

Advanced 3D Monte Carlo Algorithms for Biophotonic and Medical Applications

Lewis McMillan



University of
St Andrews

This thesis is submitted in partial fulfillment for the degree of
PhD
at the
University of St Andrews

August 2019

Declaration

I, Lewis McMillan, hereby certify that this thesis, which is approximately 32000 words in length, has been written by me, that it is the record of work carried out by me, or principally by myself in collaboration with others as acknowledged, and that it has not been submitted in any previous application for a higher degree.

I was admitted as a research student in September 2015 and as a candidate for the degree of PhD in September 2015; the higher study for which this is a record was carried out in the University of St Andrews between 2015 and 2019.

Date Signature of candidate

I hereby certify that the candidate has fulfilled the conditions of the Resolution and Regulations appropriate for the degree of PhD in the University of St Andrews and that the candidate is qualified to submit this thesis in application for that degree.

Date Signature of supervisor

Date Signature of supervisor

Abstract

The Monte Carlo radiation transfer (MCRT) method is a that allows the simulation of light transport through turbid media. MCRT allows the simulation of multiple anisotropic scattering events, as well as a range of microphysics such as polarisation, and fluorescence. This thesis concerns the development of MCRT algorithms to solve various biophotonic and medical problems.

Chapter 2 introduces the MCRT method and gives an in depth description of the theory and how it is implemented in code. Details of code parallelisation is also presented.

Chapter 3 introduces a numerical model of tissue ablation. This models uses MCRT to calculate the energy deposited by a laser, a numerical heat simulation to diffuse the heat deposited by the laser, and finally a numerical tissue damage model to calculate the damage to the tissue due to the laser. Laser tissue ablation is used for a variety of medical and cosmetic treatments. It can be used to help topical drug diffusion, treat acne and rhinophyma, and can make the skin look younger. This model was created to predict ablation crater depth, and to help and optimise ablation treatments which can lead to improved patient outcomes.

The work in chapter 4 pertains to the modification of the “traditional” ballistic light MCRT algorithm, such that it can now model wave like behaviour of light. This work was undertaken so that a comparison of Bessel beams and Gaussian beams propagation in turbid media can be carried out.

Finally, the work contained in chapter 5 focuses on the modelling of the autofluorescence response of human skin. The autofluorescent response of tissue has been noted as a biomarker for various disease, including cardiovascular disease. This chapter presents a discussion on the effect of tissue optics on the natural fluorescence of cells, including how Fitzpatrick skin type, area of the body, and blood volume effect the response of the various fluorophores responsible for the autofluorescent response.

Acknowledgements

First of all, thank you to Tom, and Kenny for first allowing me the opportunity to undertake this PhD and for all their support and encouragement over the course of my thesis. If it weren't for you both keeping me on the straight and narrow I'm sure I would still be coding instead of writing. I also swear my code is now bug free...

Thank you to Ian for getting me access to Wardlaw and Kennedy computer clusters. Most of this work wouldn't be possible without it.

Thank you to Isla for answering all my stupid questions over the past three years, and for being a good source of moral support. Thank you also for allowing me to be a part of code and cake, which I thoroughly enjoyed, both the baking and the talks.

Thank you to all at Ninewells for making me feel welcome every time I took up space in your research office. Especially thank you to Luke, Paul, and Ewan for letting me collaborate with you, and for your good company at the conferences we attended together.

Mcconnells

Thank you to my family for your support throughout my last nine years at St Andrews.

Kathleen smells

Contents

Declaration	iii
Abstract	v
Acknowledgements	vii
Abbreviations	xi
List of Figures	xvii
1 Introduction	1
1.1 Monte Carlo Method	2
1.2 Synopsis and Thesis Objectives	5
2 Monte Carlo Radiation Transport Technique	7
2.1 Introduction	7
2.2 Monte Carlo Radiation Transport Algorithm	7
2.2.1 Introduction and Background	7
2.2.2 Optical Properties	11
2.2.3 MCRT Algorithm	15
2.2.4 Code Details	20
2.3 Validation of MCRT Code	23
2.4 Conclusion	24
3 Computational Modelling of Tissue Ablation	25
3.1 Introduction and Background	25
3.2 Methods	26
3.2.1 Monte Carlo radiation transport (MCRT)	26
3.2.2 Heat Transport	27
3.2.3 Tissue Damage	33
3.2.4 Validation	36
3.3 <i>In silico</i> results	38
3.3.1 Introduction	38
3.3.2 Results	40
3.4 Application of Model for Spy Disposal	47
3.5 Conclusion	48
4 Quasi-wave/particle Monte Carlo Algorithm, φMC	51
4.1 Introduction	51

4.2	Theory	52
4.2.1	Complex Phase Tracking	52
4.2.2	Huygens-Fresnel Principle	53
4.2.3	Validation of Phase Tracking Algorithm	54
4.3	Gaussian Beams	59
4.4	Bessel Beams	62
4.4.1	Theory	63
4.4.2	Validation	64
4.5	Higher Order Bessel Beams	70
4.6	Comparison	73
4.6.1	Discussion	76
4.7	Conclusion	77
5	Modelling Auto fluorescence in Skin for Novel Biomarkers of Cardiovascular Diseases	79
5.1	Introduction	79
5.2	Skin Model	80
5.2.1	Optical Properties	82
5.2.2	Fluorophores in the Skin	86
5.3	Modelling Fluorescence	87
5.4	Nelder-Mead Method	91
5.5	Validation	93
5.6	Results	97
5.6.1	Experimental Work	97
5.6.2	Effect of Tissue Optics on Fluorescent Signal	99
5.6.3	Using the NM Method	101
5.7	Discussion	103
5.8	Conclusion	105
6	Conclusion	107
6.1	Summary	107
6.2	Future Prospects	108
Appendix A	Fresnel Reflections	113
Appendix B	Detected Light Fluence Tracking Method	117

Abbreviations

T_a ablation temperature.

AMR adaptive mesh refinement.

BPM beam propagation methods.

BPM beam propagation method.

CDF cumulative distribution function.

CVD cardiovascular disease.

CVDs cardiovascular diseases.

EEM excitation emission matrix.

FDM finite difference method.

FDTD finite difference time domain.

FEM finite element method.

HOBBs higher order Bessel beams.

K-M theory Kubelka-Munk theory.

MCRT Monte Carlo radiation transfer.

MPI Message-passing interface.

NM Nelder-Mead.

OBS optical biopsy system.

OCT optical coherence tomography.

PDF probability density function.

PDT photo-dynamic therapy.

PORH post occlusive reactive hyperemia.

PSTD pseudo-spectral time-domain.

RTE radiative transfer equation.

List of Figures

- 1.1 Sample Buffon needle experiment. 100 needles are dropped on a 10×10 cm area with lines spaced 1.5 cm apart. If a needle lands on a line it is recorded and coloured blue, else it is red. This simulation gave a value of $\pi \approx 3.10$.
- 1.2 Illustration of the rejection method for determining π from the area of a circle inscribed within a square. The ratio of the area of the circle to the square is $\frac{\pi}{4}$. Thus the ratio of darts landing in the circle to those that land outside the circle is $\pi \approx \frac{4N_{inner}}{N_{total}}$, where N_{total} is the total number of darts, and N_{inner} is the total number of darts that land in the circle. Using 200 darts gave a value of $\pi \approx 3.12$.
- 1.3 Example of randomly sampling from a spectrum. Figure shows 100 random samples drawn to recreate a solar spectrum.
- 1.4 Computer generated imagery using ray tracing. The Monte Carlo method is used to “compute radiance along ray paths between lights and the camera”, to generate CGI images [23].
- 2.1 Energy flow through area dA within solid angle $d\Omega$ in a direction \hat{s} . Adapted from [31, 32].
- 2.2 Cylindrical volume element, $ds dA$, with solid angle $d\Omega$ in direction \hat{s} and solid angle $d\Omega'$ in direction \hat{s}' . Energy flowing through this element is used to derive the radiation transfer equation. Adapted from [31, 32].
- 2.3 Figure shows the g factor for the Henyey-Greenstein phase function, for various configurations of back, forward or isotropic scattering. Arrow indicates the photons initial direction before scattering.
- 2.4 Examples of wavelength dependent absorption coefficients for some common tissue chromophores [43, 47–55].
- 2.5 Flowchart of the Monte Carlo radiation transport algorithm as described in this section.
- 2.6 Example of a possible voxel model, with three different layers, various holes due to ablative pixel beam lasers (see Chapter 3). Each voxel can represent a different optical/thermal property of the tissue medium.
- 2.7 Illustration of photon propagation through a 2D grid. d_{x1} , and d_{y1} are the distances to the voxel walls in the x and y directions in the μ_1 voxel. In this case $S_1 = d_{x1}$ as d_{x1} is smaller than d_{y1} , thus the photon hits the voxel wall in the x direction. For the μ_5 voxel, d_y is smaller, thus the photon hits the voxel wall in the y^{th} direction.
- 2.8 Illustration of rotating the centre of mass frame to the lab frame. \mathbf{n} is the direction vector of the photon before scattering, and \mathbf{n}_s is the scattered direction vector. θ and φ are the scattering angles. z_s is in the same direction as \mathbf{n} .

- 2.9 Source code hierarchy, showing the relationship between different modules. Green is the entry point for the simulation. Red are the data modules, light blue are the routine modules, and grey are the external dependencies.
- 2.10 Performance of the parallelisation of the MCRT code using MPI.
- 2.11 Figure shows the fluence as a function of depth. Figure also shows comparison to the Jacques MCRT simulation and the MCRT as described in this chapter.
- 3.1 Flowchart of the tissue ablation algorithm.
- 3.2 Red lines are packet paths within a voxel. Black lines packet paths out with the voxel. Red packet paths, weighted by μ_a , are summed up to calculate the absorbed energy within each voxel.
- 3.3 Finite difference method stencil for simple explicit scheme.
- 3.4 Computational domain decomposition. Total computational domain (red outline) is evenly divided between cores in the CPU. This is done via layers of the domain in the z direction. Information is passed to/from cores via the “halo swap” process (see Fig. 3.5).
- 3.5 Halo swapping. Process A updates the area in red and blue on the left. It updates the blue area which is sent to process B as B’s “halo”. Process B cannot update its own halo, but rather updates the halo for process A.
- 3.6 Figure shows the speed up gained by parallelisation of the heat simulation using the “halo swapping” technique, for various sizes of computational domain (voxels). Data taken from a Intel Xeon E3-1245 v5, 8 cores @ 3.5GHz machine.
- 3.7 Ablation of a dog aorta, as viewed under a microscope. Steam vacuoles are clearly visible either side of the ablation area. Carbonisation is also evident at the edges of the ablation fronts. Adapted from [79].
- 3.8 Temperature of the cube for various times, comparing between analytical solution and numerical method.
- 3.9 Simulation of 81 pixel beams. Figure a) shows a slice through the optical properties at the end of the simulation in the z-y plane. Figure b) shows the optical properties in the x-y plane at the top surface. Yellow is unchanged tissue, and purple is completely ablated tissue. Figure shows that the ablation craters do not overlap one another.
- 3.10 Simulation of 70 W CO₂ ablative laser, with a circular beam profile. Crater depths as a function of pixel beam energy for various ablation temperature (T_a)’s.
- 3.11 Simulation of 70 W CO₂ ablative laser, with a Gaussian beam profile. Crater depths as a function of pixel beam energy for various T_a ’s.
- 3.12 Temperature bore hole though centre of medium as a function of time, for $T_a=500$ °C.
- 3.13 Figure shows the maximum horizontal extent of thermal damage as a function of energy per pixel beam, for different T_a ’s.
- 3.14 Tissue thermal damage around the ablation crater (white). Thermal tissue damage values of 3 refer to 3rd degree burns, 2 to 2nd, and 1 to 1st degree burns respectively. P is the power in Watts, T_a is the ablation temperature in Kelvin, and E_p is the energy per pixel beam in mJ.
- 3.15 Figure show the time taken for 1st, 2nd, and 3rd to occur as a function of depth, for a range of T_a ’s at 400 mJ.
- 3.16 Figure show the time taken for 1st, 2nd, and 3rd to occur as a function of depth, for a range of T_a ’s at 50 mJ.
- 3.17 Comparison of the different pulse profiles trialled for a pulselength of 0.2 s.
- 3.18 Comparison of various pulse shapes for the pixel beams.

- 3.19 Comparison of ablation depths for different initial temperatures in the porcine skin.
- 3.20 Comparison of maximum horizontal damage distance for different initial porcine skin temperatures.
- 3.21 Comparison of different voxel temperatures after ablation. Half refers to setting the temperature of a voxel to half that of the ablation temperature. Room refers to room temperature, and ablation leaves the temperature at the ablation temperature.
- 3.22 Still image of the iconic laser scene in the film Goldfinger. Copyrights Eon Productions.

- 4.1 Example of phase calculation when a photon has travelled a distance l . The figure also shows an example of interference between two photons via addition of the complex amplitudes at the point P_0 .
- 4.2 Illustration of the Huygens-Fresnel principle. At t_0 a wave is incident on an aperture. Times t_1 , t_2 , and t_3 show the evolution of the wavefront using the Huygens-Fresnel principle. Dashed lines illustrate the wavefront position at the previous time step, and is the source of the Huygens-Fresnel wavelets.
- 4.3 Comparison of theory and simulation for the double slit experiment. Top image shows a slice through the computed image and the expected profile from theory. For clarity only every 5th MCRT data point is plotted. Bottom image shows the computed image.
- 4.4 Geometry of the square aperture used in the validation.
- 4.5 Comparison of theory and simulation for diffraction through a square aperture in the Fresnel and Fraunhofer regimes.
- 4.6 Illustration of a Gaussian beam focusing to its waist then diverging away. Image shows the various defined properties of a Gaussian beam along side the radius of curvature changing direction at the waist.
- 4.7 Simulation setup of focusing a Gaussian beam through a lens. Lens is convex-plano and is modelled on ThorLabs LA4249 UV fused silica lens [134]. L_t is the lens thickness, D is the $\frac{1}{e^2}$ input beam diameter, W_d is the working distance or back focal length, $2 \cdot z_{max}$ is the depth of the medium, and w_0 is the beam waist.
- 4.8 Results of *in-silico* experiment of focusing a Gaussian beam though a convex-plano lens.
- 4.9 Slice through the real part of the complex electric field of the *in-silico* experiment as in Fig. 4.7. Figure shows the radius of curvature changing direction at the waist as predicted by theory.
- 4.10 Illustration of φMC 's ability to model spherical aberrations. Top image generated using same setup as in Fig. 4.7, but with $D = 1.5\text{ mm}$ within φMC . Image shows the elongated focus and characteristic interference pattern behind the focus. Bottom image shows illustration of rays traced through a lens which suffers from spherical aberration.
- 4.11 Geometry of a Bessel beam, generated by an axicon lens. β is the angle with the optical axis, and the angle of the conical waves. α is the axicon angle.
- 4.12 Comparison of theoretical and MCRT simulation of a Bessel beams, with intensity normalised. The results from φMC show good agreement with the theory.
- 4.13 Bessel beam in the far field. Bessel beams in the far field become ring beams. Image shows a slice of intensity through the medium.

- 4.14 Illustration of the Bessel beams self-healing property. Highly absorbing cube placed near the top of the medium. Figure shows that the Bessel beam forms further down the optical axis. a) shows side on view with the obstacle at 0.02 mm , b) shows top down view at surface of the simulated $b=\text{medium}$ before the obstacle, c) shows top down view in the middle of the obstacle, and d) shows the top down view after the Bessel beam has ‘healed’.
- 4.15 Experimental set-up for propagating a Bessel beam through a cuvette filled with varying concentrations of Intralipid 20%. Bessel beam is imaged by an $20\times$ objective lens and a Grasshopper 3 camera.
- 4.16 Scattering properties of 20% Intralipid [149].
- 4.17 Comparison of experimental and simulation data for propagation of a Bessel beam produced by an axicon, through mediums of various turbidity. Images a) to g) is the data from φMC , and h) to n) are the experimental data. Volumes along the top are the volume of Intralipid in each solution as in Table 4.1. All images are cropped so they are the same size and normalised to the maximum value in each image.
- 4.18 Line graph plots of slices taken through the generated and experimental images as shown in Fig. 4.17.
- 4.19 Comparison of a larger medium, 2 mm^3 versus that of a smaller medium, $0.5\text{ mm}\times 0.5\text{ mm}\times 2.00\text{ mm}$. The figure shows that the smaller medium gives a better signal to noise ratio, whilst still accurately modelling the experiment.
- 4.20 Helical delay element attached to an axicon. The Axicon introduces a radial delay in addition to that of the helical element. If the input beam is a Gaussian, the output beam is a higher order Bessel beam, $l > 0$.
- 4.21 Higher order Bessel beams (HOBBs). a) to d) show the phase shift due to the helical element. e) to h) show line plots of the simulation data compared to the theory. i) to l) and m) to p) show the higher order Bessel beam images for theory and simulation data respectively.
- 4.22 First comparison of Bessel and Gaussian beams with equal power used to generate both beams. Plots taken at the Gaussian beams focus. The maxima at the sides of the Gaussian beam in the $0.0\mu L$ plot are due to simulation effects, mainly the small size of the medium not allowing photons from further off the optical axis to interfere destructively.
- 4.23 First comparison of Bessel and Gaussian beams, with equal power used to generate both beams. Plots taken at the bottom of the simulated medium.
- 4.24 Second comparison of Bessel and Gaussian beams for the case where the power given to each beam, yields the same maximum at the Gaussian beams focus. These plots are taken from the Gaussian beams focus.
- 4.25 Comparisons of unequal powered beams at the bottom of scattering medium.
- 4.26 Illustration of how a Bessel beam becomes degraded due to scattering. Top image shows how two photons propagate through the axicon and constructively interfere to produce a Bessel beams. Bottom image shows how scattering can affect this process.
- 5.1 Simplified schematic showing the roles of NADH and FAD in various different metabolic pathways. The star boxes indicate fluorescing forms of NADH and FAD. Taken from Croce *et al.* [172].
- 5.2 Illustration of our five layer skin model. Image not to scale.
- 5.3 Absorption coefficients for the various chromophores found in our skin model.

- 5.4 Absorption coefficients for the different layers in our skin model.
- 5.5 Figure shows the reduced scattering coefficient for the different layers of our skin model.
- 5.6 Top) Shows the fluorescent emission for the various different fluorophores. Bottom) Extinction coefficients for a selection of fluorophores found in the skin [185–192].
- 5.7 Jablonski diagram for PPIX. Bold lines indicate the lowest vibrational state of the electronic state, and thinner lines indicate higher vibrational modes of the electronic states. a) shows excitation of the ground singlet state via absorption of a photon to the second singlet state, b) non-radiative transition, and c) fluorescence.
- 5.8 Optical properties of Coproporphyrin III. The figure on the left shows the absorption coefficient as a function of wavelength. The figure on the right shows the emission spectrum as a function of wavelength.
- 5.9 Validation of fluorescence modelling technique as described above. Figure shows that the MCRT method matches closely to the experimental results.
- 5.10 Operations that can be preformed on a simplex for $n = 2$.
- 5.11 Nelder-Mead decision tree. Here $>$ means better, and $<$ worse. Best, lousy, and worst have the same meanings as in the main text.
- 5.12 Contour plots of test functions with Nelder-Mead simplexes over plotted. Top left is the Ackley function, top right is the sphere function, bottom left is the Himmelblau's function, and the bottom right is the Rosenbrock function. Grey lines are contours, coloured lines are the simplices with the blue simplex being the initial simplex. Finally, the black dots represent the global minima for that function.
- 5.13 Example of toy model spectrum for testing NM method. The two peaks correspond to the fictitious fluorophore, and NADH.
- 5.14 Illustration of how the Savitzky-Golay filter works on noisy data and recovers the roughly the same signal on the same data set with less noise. Left image shows the raw signals from the simulations with a packets difference of 10^{-3} . Right image shows the data set after the Savitzky-Golay filter is applied. A window size of 101, and polynomial of order 2 were used as the filter settings.
- 5.15 Figure shows the search space for the 2D toy problem outlined above. A line of best fit is fitted to the concentrations found by the Nelder-Mead (NM) method. Note also the valley of good fit where the line of best fit lies. The search space is also fairly smooth.
- 5.16 Figure shows the line of best fit for the case where $n = 3$. Figure also shows the simplices path over their whole lifetime, from initial guess to final simplex.
- 5.17 Example of a PORH test whilst measuring autofluorescence and perfusion. The perfusion of blood in the skin decreases once the cuff is inflated, and then rapidly reaches a maximum once the cuff is removed. The inverse of this can be seen in the autofluorescent response of NADH in the tissue.
- 5.18 Figure shows an example of a raw spectrum taken by S. Smirni *et al.*. This figure illustrates how the spectrum is red-shifted, along with some of the artifacts, backscatter, and autofluorescence peaks. There is also a third peak in the red end of the spectrum. The cause of this is unknown, but most likely due to an unidentified fluorophore.
- 5.19 Penetration of UV radiation as a function of depth.
- 5.20 Detected “fluence” for FAD, NADH, and elastin fluorescence. Inset shows zoom in of top layers of the skin, note the inset is a linear scale.

- 5.21 Amount of packets escaping as a function of depth for FAD and NADH fluorescence.
- 5.22 NADH and FAD absorption and emission spectra.
- 5.23 Excitation-emission matrix for NADH. Figure shows that the fluorescent signal from NADH is strongest in the papillary dermis.
- 5.24 Excitation-emission matrix for FAD. Figure shows that the fluorescent signal from FAD is strongest in the reticular dermis.
- 5.25 Figure shows the diagnostic information output by the NM method. Top left) shows the size of the simplex as it evolves. Top right) shows the best point in the simplex as it evolves. Bottom left) shows the average fitness of the simplex. Bottom right) shows the number of calls to the MCRT code per iteration of the simplex. The more call to the MCRT the simplex requires, the longer the runtime.
- 5.26 Figure shows the best result from the NM operating on the experimental data from S. Smirni *et al.*. The spectrum has a fitness of ~ 3 . The figure also shows the makeup of the final spectrum by the individual fluorophores.

- 6.1 Image on the left shows the fluence of light in a gourd, calculated using Monte Carlo radiation transfer (MCRT). The optical properties of the gourd in this simulations are similar to that of skin. The optical properties of the medium around the gourd are that of air. Image on the right shows a rendering of the same mesh in blender.

- A.1 Geometry for reflection of light at a refractive change boundary. I is incident light, R is the reflected light, and N is a normal to the surface. Here, θ is the angle of incidence which is equal to the angle of reflection.
- A.2 Geometry of light refraction and reflections.

- B.1 Example of the push and pop operation on a stack. The first operation add the integer 2 to the stack. The second operation push 7 to the stack. The last operation pops the 7 from the stack.

Chapter 1

Introduction

The advent of the computer in the last 80 years has been a boon for society. Increasing computing power is easily available, allowing higher-quality research, and research into topics once thought beyond human computation. One topic where computers have revolutionised is medicine. Computers have enabled advances in many areas including drug discovery [1, 2], patient diagnoses [3, 4], and better imaging modalities [5, 6]. One particular area of focus where computers are or will be heavily used is personalised medicine.

Personalised medicine is where instead of a patient being treated with what works on an “average” patient, the treatment is tailored specifically for the patient. This entails having fine grained knowledge of the patient down to the genome level, to understand how various drugs or treatments will affect the patient. One particular area of research in personalised medicine is into the so called “digital twin”. A digital twin as defined by A. El Saddik [7]:

“A digital twin is a digital replica of a living or non-living physical entity.”

Digital twins are currently heavily used in engineering to predict when various machinery will need to undergo maintenance. Digital twins operate by modelling their physical counterpart. This model is updated via information from their physical counterpart which allows the digital twin predict it’s physical counterparts future behaviour. Companies like Phillips use this in their MRI machines to help schedule downtime, and predict which parts the engineer will need on site, both of which minimises the downtime of the machine which is import for the hospital/clinic [8].

At the heart of the digital twin method, is the ability to accurately model the object or living thing being studied. This can be straightforward when the twin in question is a machine, as sensors can usually be attached to the various components to get feed back on the machines operation. Machines also have the bonus of (normally) be completely understood so that modelling them is usually easy. However, this is not as straightforward when dealing with biology. First, we still do not have a complete understanding of the biology within humans. Therefore, modelling a human accurately is not possible as various assumptions and approximations have to be made. Second, to get accurate information on what is happening inside a patient, generally either ionising radiation needs to be used, or cameras inserted into the patient. Both of these cannot be done for indefinite periods without causing harm or discomfort to the patient. Therefore, continuous information on the inner functions of the body is not possible. One area where information is more readily available is the skin. Information on the skin function or dysfunction is normally diagnosed with light. Light is also used in various treatments such as photodynamic therapy and tissue ablation, over various internal and external sites on the body. Lights interaction over the whole spectrum, from the UV to the infrared, is readily modelled

with techniques such as MCRT. MCRT allows a digital twin model of the individual patient skin to be simulated. This can then be used to tailor treatment regimes for the individual patient, or to predict treatment outcomes for specific patients. The use of simulations techniques like MCRT allow testing *in-silico*, can negate the need to test on humans or animals.

This thesis concerns the development of various MCRT models to help diagnose, optimise treatments and help predict which imaging modalities may be better.

1.1 Monte Carlo Method

The Monte Carlo method is a numerical analysis technique based upon random numbers, which are used to calculate unknown variables in problems [9, 10].

The earliest use of the method is in Buffon's needle experiment of the 18th century [11–13]. Buffon asked the question;

"Suppose we have a floor made of parallel strips of wood, each the same width, and we drop a needle onto the floor. What is the probability that the needle will lie across a line between two strips?"

The solution to this question is: for a needle length l , strip separation s , where x is the distance from the needle to the closest line, and θ is the angle of the needle with respect to the wood strips. Then using a simple geometrical argument, a needle crosses a strip if $x \leq \frac{l}{2} \sin\theta$.

x is distributed uniformly in $[0, \frac{s}{2}]$, and θ in $[0, \frac{\pi}{2}]$. Therefore the probability density function for x is $p(x) = \frac{2}{s}$, and θ is $p(\theta) = \frac{2}{\pi}$. The probability density function (PDF), is a function of a variable that gives probability for a variable to take a given value. The PDF is normalised over the whole range of the variable, in this case x , and θ . Thus, as x and θ are independent variables, giving a joint probability of $p(x, \theta) = \frac{4}{s\pi}$. So the probability of a needle of length l ($l < s$) is:

$$P = \int_0^{\frac{\pi}{2}} \int_0^{\frac{l}{2} \sin\theta} \frac{4}{s\pi} dx d\theta = \frac{2l}{s\pi} \quad (1.1)$$

Equation (1.1) can be used to carry out a Monte Carlo estimation of π . A simple rearrangement yields: $\pi = \frac{2l}{sP}$ where P is the ratio of needles crossing the line to the total number dropped. Laplace was the first to suggest that Buffon's needle experiment could be used to estimate π [12]. Figure 1.1 shows an example of a simulation of Buffon's needle experiment.

There are various different approaches to using the Monte Carlo method to obtain randomly sampled variables. One analytical way of achieving this is the inverted sampling method. The inverted sampling method can be summarised by the following steps for drawing a sample X_i from an arbitrary PDF $p(x)$:

1. Compute the cumulative distribution function (CDF) $P(x) = \int_0^x p(x')dx'$
2. Compute the inverse $P^{-1}(x)$
3. Obtain a uniformly distributed random number ξ
4. Finally, compute $X_i = P^{-1}(\xi)$

If a given problem cannot use the inverted sampling method, as it may not be possible to get a PDF or analytically invert the CDF, then the rejection method can be used. The rejection method is essentially a dart throwing method. This means that points are drawn and compared to the function. If the point lies under the function then the point is accepted, if it lies above the function then it is rejected. For example, if a function, $f(x)$ that does not have an analytical PDF, we can use a PDF $p(x)$ such that $f(x) < cp(x)$ where c is a constant. Therefore sampling

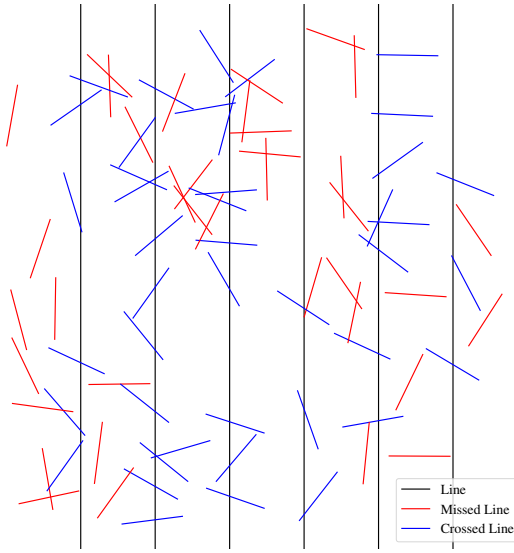


Figure 1.1: Sample Buffon needle experiment. 100 needles are dropped on a 10×10 cm area with lines spaced 1.5 cm apart. If a needle lands on a line it is recorded and coloured blue, else it is red. This simulation gave a value of $\pi \approx 3.10$.

from $p(x)$, and if the sampled point lies under $f(x)$ it is accepted, else it is rejected. Figure 1.2 shows an example of this process.

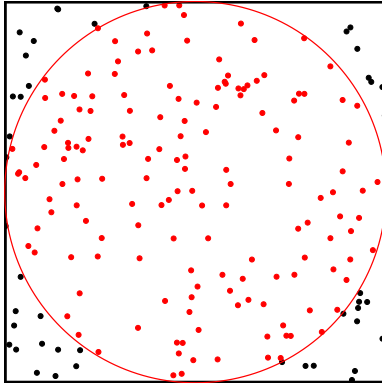


Figure 1.2: Illustration of the rejection method for determining π from the area of a circle inscribed within a square. The ratio of the area of the circle to the square is $\frac{\pi}{4}$. Thus the ratio of darts landing in the circle to those that land outside the circle is $\pi \approx \frac{4N_{inner}}{N_{total}}$, where N_{total} is the total number of darts, and N_{inner} is the total number of darts that land in the circle. Using 200 darts gave a value of $\pi \approx 3.12$

One common use of the Monte Carlo method, is to randomly sample from a spectrum. To generate a random sample from a spectrum, first the CDF of the spectrum must be calculated. This is done by first normalising the PDF, where the PDF in this case is the spectrum it self. It is normalised such that the sum of the PDF is unity. The CDF is then just the cumulative sum

of the PDF. Then using the above method as described above, a random number is drawn, ξ , and the bracketing values in the CDF are found. We then interpolate to get the x and y values corresponding to ξ . Figure 1.3 shows the result of this process for 100 random samples.

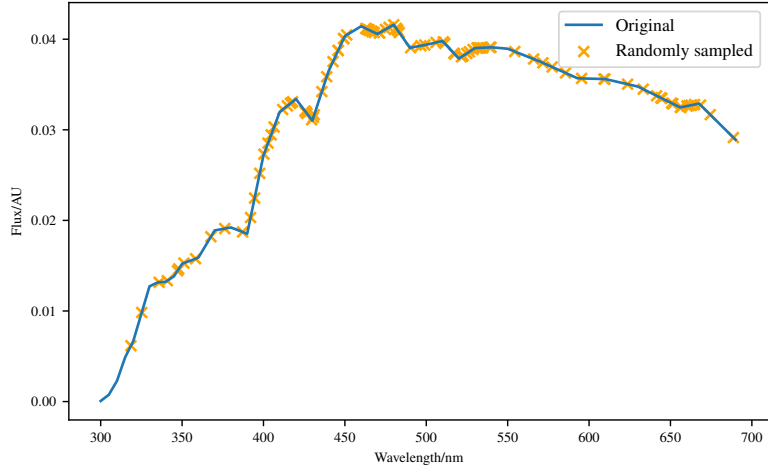


Figure 1.3: Example of randomly sampling from a spectrum. Figure shows 100 random samples drawn to recreate a solar spectrum.

The Monte Carlo method is used in various different disciplines. Ranging from use in the financial sector to analyse investments and stocks by simulating the sources of uncertainty which affect their values [14, 15], use in statistical analysis [16], and in modern computer generated images (see Fig. 1.4) [17, 18]. It is also widely used in astronomy [19, 20] and medicine [21, 22], to simulate the propagation of radiation through scattering (turbid) media. This technique, MCRT, is what makes up the bulk of this thesis and is described in depth in the following sections.

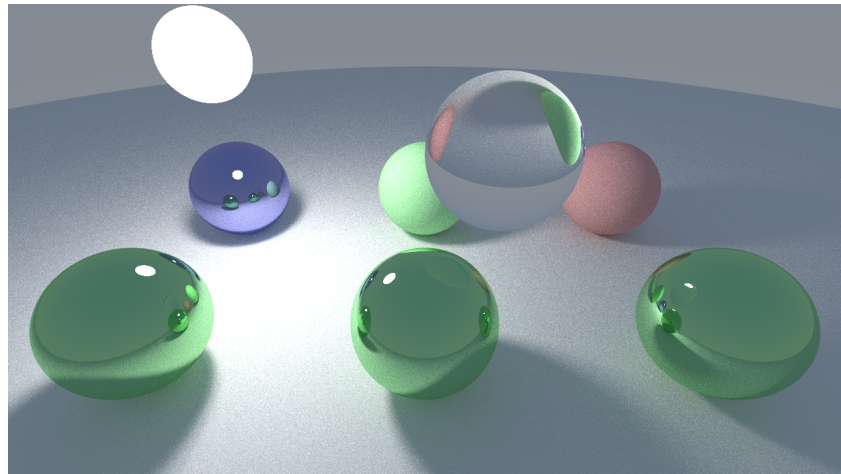


Figure 1.4: Computer generated imagery using ray tracing. The Monte Carlo method is used to “compute radiance along ray paths between lights and the camera”, to generate CGI images [23].

1.2 Synopsis and Thesis Objectives

Chapter 2 details the MCRT method that is used for the bulk of this thesis. Presented in this chapter are details of the algorithm and various code details that underpin the whole thesis. Details of speed up techniques such as parallelisation are also presented. Finally the code is validated against other results.

Chapter 3 details the tissue ablation model. Discussion of the individual components of the model, alongside validation of the model against theoretical and experimental evidence is presented.

Chapter 4 presents an adaptation to the regular Monte Carlo model so that it can model wave like properties of photons including diffraction and interference. The new algorithm is validated against several theoretical expressions and experimental data. Finally the algorithm is used to compare Bessel beams and Gaussian beam in highly turbid media, to determine which beam performs better.

Chapter 5 details the modelling of a novel biomarker for cardiovascular disease, autofluorescence. The theoretical groundwork for the biomarker is outlined, along with discussion of how MCRT can model fluorescence. Presented alongside this is ameombaMCRT, a Monte Carlo radiation transfer simplex algorithm used to determine concentrations of fluorophores in different layers of tissue for a given spectrum.

Finally, chapter 6 concludes this thesis and presents possible future avenues of research that could be undertaken.

Chapter 2

Monte Carlo Radiation Transport Technique

2.1 Introduction

This chapter will provide an overview of the MCRT method and compares it to other methods. Details of the MCRT code developed during this project and used as the basis of the results reported in subsequent chapters, validation of code, and details of computational speed up are also presented.

2.2 Monte Carlo Radiation Transport Algorithm

2.2.1 Introduction and Background

The technique that makes up the bulk of this thesis is the MCRT technique. This method was developed at the end of the Second World War at the Los Alamos National Laboratory, for the purpose of calculating neutron diffusion through shielding material [24–27]. It has since found a myriad of applications from light transport through dusty galactic clouds [28], calculating doses for radiotherapy [29] to light transport through tissue [30].

The theory that governs the transport of radiation through a medium is the radiative transfer equation (RTE). Before describing MCRT which is a numerical simulation of the RTE, the theory of radiation transport must be examined.

Radiative Transfer

Transport of radiant energy through turbid media can be modelled analytically using the RTE. The RTE models the radiative losses and gains by a beam of radiation as it propagates, including: loss of energy due to absorption, loss/gain of energy due to scattering, and energy gain due to emission. Before deriving the RTE, definitions of some terms and physical quantities is required.

The first term is spectral irradiance, L_ν . Spectral irradiance is defined as the energy flow in a direction $\hat{\mathbf{n}}$, for a solid angle $d\Omega$, per unit time per unit temporal frequency bandwidth. Irradiance is defined as the spectral irradiance over a small frequency range $[\nu, \nu + \Delta\nu]$:

$$L(\vec{r}, \hat{s}, t) = L_\nu(\vec{r}, \hat{s}, t)\Delta\nu \quad (2.1)$$

Where:

- \vec{r} is the position;
- \hat{n} is the unit normal vector;
- t is the time;
- and $L(\vec{r}, \hat{s}, t)$ is the irradiance [$W m^{-2} sr^{-1}$].

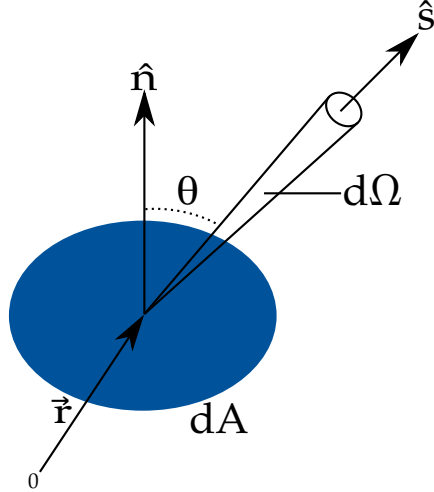


Figure 2.1: Energy flow through area dA within solid angle $d\Omega$ in a direction \hat{s} . Adapted from [31, 32].

The irradiance can be used to determine the energy, dE , transported across an area dA , in a solid angle $d\Omega$ in a time dt (see Fig. 2.1) is:

$$dE = L(\vec{r}, \hat{s}, t) \cdot \cos(\theta) \ dA \ d\Omega \ dt \quad (2.2)$$

Where:

- \hat{n} is the unit normal to dA ;
- and $\cos(\theta)$ is the angle between \hat{n} and \hat{s} .

Irradiance can also be used to determine the fluence rate, ϕ , which is defined as the energy flow per unit time, independent of the flow direction.

$$\phi(\vec{r}, t) = \int_{4\pi} L(\vec{r}, \hat{s}, t) \ d\Omega \quad (2.3)$$

Where:

- ϕ is the fluence rate [$W m^{-2}$].

Solving the RTE yields the irradiance which gives the distribution of light in the medium, and gives information on the state of the system and all the physical properties of it.

With the irradiance defined, as well as the other quantities that follow, the RTE can be derived [31, 32]. First considering the conservation of energy, as shown in Eq. (2.4).

$$dP = -dP_{div} - dP_{ext} + dP_{scatt} + dP_{src} \quad (2.4)$$

Where:

- dP is the total change in energy in the volume $dA ds$ within the solid angle, $d\Omega$, per unit

time (see Fig. 2.2);

dP_{div} is the energy loss due to the divergence of the radiation beam per unit time;

dP_{ext} is the energy loss due to absorption and scattering within the volume $dA ds$ within the solid angle, $d\Omega$;

dP_{scatt} is the energy gain due to scattering from \hat{s}' into $d\Omega$ per unit time;

and dP_{src} is the energy gain due to emission within the medium, per unit time.

The total change in energy, dP , in the volume element within the solid angle $d\Omega$ is equal to:

$$dP = \frac{1}{c} \frac{\partial L(\vec{r}, \hat{s}, t)}{\partial t} dA ds d\Omega \quad (2.5)$$

Where c is the speed of light.

The first loss term, dP_{div} , is the energy loss due to divergence of the radiation beam. This is modelled as:

$$dP_{div} = \frac{\partial L}{\partial s} d\Omega dV \quad (2.6)$$

$$= \hat{s} \cdot \nabla L(\vec{r}, \hat{s}, t) d\Omega dV \quad (2.7)$$

dP_{ext} is the second loss term, and accounts for energy loss due to scattering and absorption in the volume element within the solid angle $d\Omega$. This is modelled as:

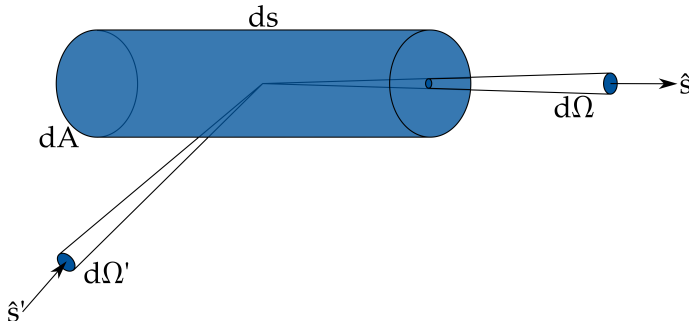


Figure 2.2: Cylindrical volume element, $ds dA$, with solid angle $d\Omega$ in direction \hat{s} and solid angle $d\Omega'$ in direction \hat{s}' . Energy flowing through this element is used to derive the radiation transfer equation. Adapted from [31, 32].

$$dP_{ext} = \mu_t ds L(\vec{r}, \hat{s}, t) dA d\Omega \quad (2.8)$$

Where μ_t is the extinction coefficient [m^{-1}], see Section 2.2.2 for further details.

The first energy gain term, dP_{src} , is due to emission in the volume element within the solid angle $d\Omega$.

$$dP_{src} = S(\vec{r}, \hat{s}, t) dV d\Omega \quad (2.9)$$

The second energy gain term, and final term, is due to the incident energy on the volume element within the solid angle $d\Omega$ in direction \hat{s} due to scattering from any direction \hat{s}' .

$$dP_{scatt} = N_s dV \left(\int_{4\pi} L(\vec{r}, \hat{s}', t) P(\hat{s}', \hat{s}) \sigma_s d\Omega' \right) d\Omega \quad (2.10)$$

$$= \mu_s dV \left(\int_{4\pi} L(\vec{r}, \hat{s}', t) P(\hat{s}', \hat{s}) d\Omega' \right) d\Omega \quad (2.11)$$

Where:

N_s is the number density of scatters [$\#m^{-3}$];

$P(\hat{s}', \hat{s})$ is the scattering phase function (see Section 2.2.2 for further discussion);

and σ_s is the cross section of the scatters [m^2], thus $\mu_s = N_s \sigma_s$, where μ_s is the scattering coefficient [m^{-1}].

Finally substituting Eqs. (2.5), (2.7) to (2.9) and (2.11) into Eq. (2.4) yields the RTE:

$$\frac{1}{c} \frac{\partial L(\vec{r}, \hat{s}, t)}{\partial t} + s \cdot \nabla L(\vec{r}, \hat{s}, t) = -\mu_t L(\vec{r}, \hat{s}, t) + \mu_s \int_{4\pi} p(\hat{s}, \hat{s}') L(\vec{r}, \hat{s}', t) d\Omega' + S(\vec{r}, \hat{s}, t) \quad (2.12)$$

In general, the RTE is hard to solve in arbitrary 3D geometries, however there are several approximations, and numerical methods available. Diffusion approximation, Kubelka-Munk theory (K-M theory), and MCRT are the common methods used to approximate or solve the RTE.

Kubelka-Munk Theory

K-M theory was originally developed to calculate the light distribution in thin layered materials, such as paint or paper [33]. The theory is rather simple and makes many assumptions about the medium and the incident light. The main assumptions of K-M theory are: only scattering and absorption take place in the medium, the incident light is already diffuse, the medium is uniform with only isotropic scattering, no external or internal reflections, and the medium is planar and infinitely wide [34–36].

These assumptions make K-M theory poor for modelling light-tissue interactions. This is because in tissue, scattering is not isotropic but rather forward biased (see Section 2.2.2). Tissue is rarely, planar and infinitely wide. Tissue also has some reflections at its external and internal boundaries, due to changes in refractive indices. Many medical and biophotonic treatments/methods use laser light which is not diffuse. Finally, tissue can also exhibit fluorescence, which the K-M theory is not able to model, along with polarization. K-M theory does have some positive aspects. **K-M theory** theory is good at calculating the diffuse reflectance of simple media, and can be used to roughly estimate calculations. Though it is not well suited for modelling light-tissue applications [37].

Diffusion Approximation

The diffusion approximation for the RTE is where the irradiance is separated into two components:

$$L(\vec{r}, \hat{s}) = L_c(\vec{r}, \hat{s}) + L_d(\vec{r}, \hat{s}) \quad (2.13)$$

Where L_c is the unscattered contribution, which satisfies Beer's law*, and L_d is the diffuse contribution. The L_d component is expanded using Legendre polynomials and truncated. The

*Beer's law (or Beer-Lambert law) states that the transmission, T , is equal to $e^{-\mu L}$, where L is the distance and μ is the attenuation coefficient.

diffusion approximation also has several assumptions and restrictions. The main assumption is that scattering dominates over absorption, and that the scattering is nearly isotropic. This restricts the types of scattering the diffusion approximation can model, though using similarity relations can partially model scattering in tissue [38, 39].

Diffusion theory is computationally fast, and simple to implement. However, it is poor at modelling light-tissue interactions due to its assumptions and restrictions, mainly the inaccurate modelling near the boundaries of the medium and its lack of modelling fluorescence and other microphysics. Though it can be used to speed up MCRT in mediums where scattering dominates [40, 41].

MCRT

The final method, MCRT, is numerically equivalent to the RTE [31]. MCRT is a flexible method, it can model arbitrary 3D geometries, various microphysics including fluorescence, and polarisation. MCRT can also model various different light sources, from collimated laser beams to diffuse light sources. The only downside noted in the literature is that the MCRT can be expensive computationally. However, with computational power growing faster with time, this is less of a problem going forward.

The next several sections give an in depth description of the MCRT method and its flexibility, along with a description of the code used in this thesis to solve various medical and biophotonic problems.

2.2.2 Optical Properties

Before an in-depth description of the MCRT method is outlined, a discussion of the optical properties of materials is presented, which the MCRT method requires to simulate the transport of photons in a material.

Optical properties of a medium are the properties that describe how light is transported through that medium. Usually the optical properties of a medium are defined by three main parameters: the scattering (μ_s) and absorption coefficients (μ_a), and the anisotropy coefficient (g).

Scattering

The scattering coefficient, along with the anisotropy value (see [Anisotropy](#)), define how light is scattered in a medium. The main scatters in the dermis and epidermis are filamentous proteins such as collagen and elastin [42]. In the upper layers of the skin, the main scatters are keratins and various chromophores such as melanin. The size of the scatters affect how light is scattered and into which direction that light is scattered into.

The scattering of light within tissue is usually defined as μ_s or μ'_s : the scattering coefficient and the reduced scattering coefficient, where $\mu'_s = \mu_s(1 - g)$. The scattering coefficient is defined such that the probability of transmission without scattering and neglecting absorption in a path length L is:

$$T = e^{-\mu_s L} \tag{2.14}$$

This gives units of inverse length for the scattering coefficient (usually measured in cm^{-1}). The reduced scattering coefficient is often given in place of the scattering coefficient, as the reduced coefficient is more easily measured than the “normal” coefficient [43].

Anisotropy

Anisotropy is the degree of deviation that light undergoes at each scattering event. The anisotropy value is taken from the phase function for the medium. The phase function is defined as the angular distribution of light intensity scattered by a particle. The phase function, $\Phi(\theta, \phi)$, is usually normalised over all angles:

$$\int_{\Omega} \Phi(\theta, \phi) d\Omega = 1 \quad (2.15)$$

Where θ , and ϕ are the usual polar and azimuthal spherical angles, and $d\Omega = \sin \theta d\theta d\phi$. Thus, for Rayleigh and isotropic scattering, their phase function's are:

$$\Phi_{isotropic}(\theta, \phi) = \frac{1}{4\pi} \quad (2.16)$$

$$\Phi_{Rayleigh}(\theta, \phi) = \frac{3}{8\pi}(1 + \cos^2(\theta)) \quad (2.17)$$

For simplicity, the phase function is usually cast as the anisotropy value g , which is defined as the average angle of deflection:

$$g = \langle \cos(\theta) \rangle = \int_{\Omega} \cos \theta \Phi(\theta, \phi) d\Omega \quad (2.18)$$

The anisotropy factor, g , can take on any value from -1 to 1 . Where a value of -1 is totally back scattering, 0 is isotropic scattering, and 1 is totally forward scattering (see Fig. 2.3).

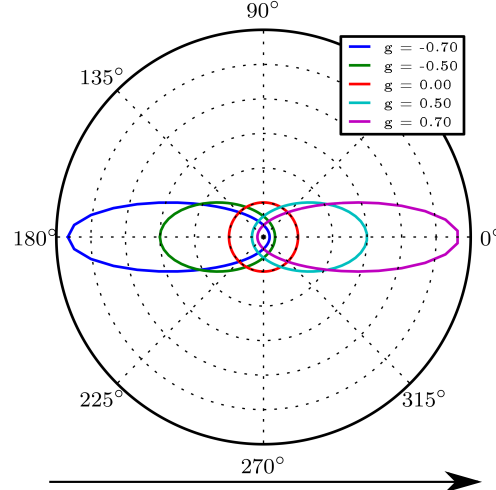


Figure 2.3: Figure shows the g factor for the Henyey-Greenstein phase function, for various configurations of back, forward or isotropic scattering. Arrow indicates the photons initial direction before scattering.

There are many phase functions that can be used to model the anisotropy factor in a medium. The standard phase function in biological tissue is the Henyey-Greenstein phase function. The Henyey-Greenstein phase function, was originally created to model scattering of diffuse radiation in the galaxy [44, 45]. It has since become the *de-facto* phase function for biological tissue. This

is due to the phase functions relative simplicity and due to it being regarded as a “good” phase function for approximating scattering in biological tissue [46]. The Henyey-Greenstein phase function is shown in Eq. (2.19):

$$\Phi_{H.G}(\theta, \phi) = \frac{1}{4\pi} \frac{1 - g^2}{(1 + g^2 - 2g \cos(\theta))^{\frac{3}{2}}} \quad (2.19)$$

Absorption

Absorption of light by a medium is defined by the absorption coefficient μ_a . The absorption coefficient is defined in a similar fashion to the scattering coefficient, by considering the probability of transmission without absorbing and neglecting scattering in a path length L:

$$T = e^{-\mu_a L} \quad (2.20)$$

This, again like the scattering coefficient, gives inverse distance for the unit of the absorption coefficient (and usually measured in units of cm^{-1}).

There are various sources of absorbers in tissue including blood, water, fat, melanin, β -carotene, and bilirubin. These chromophores can all contribute, depending on the wavelength, with some more absorbing than others, as shown in Fig. 2.4. The absorbed photons can then be remitted as fluorescence or absorbed as heat.

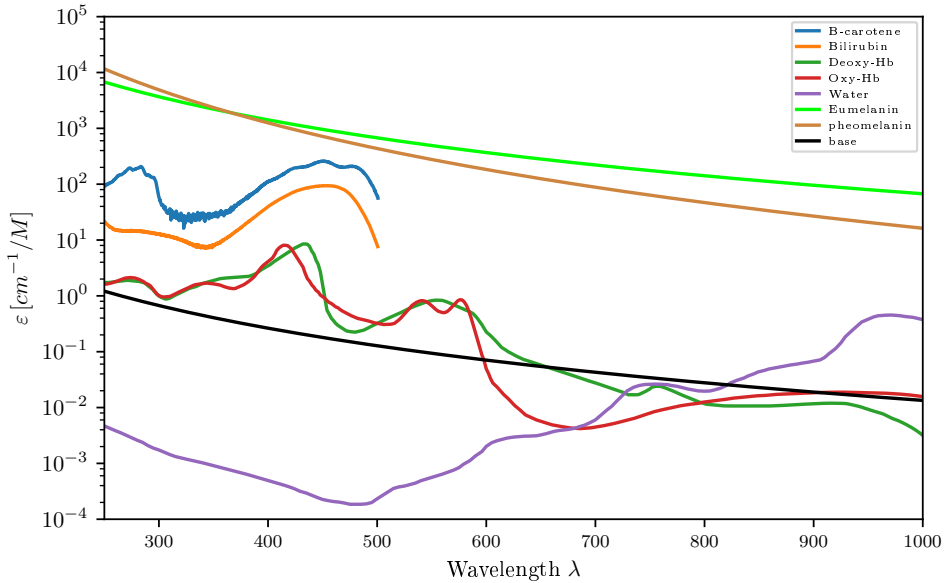


Figure 2.4: Examples of wavelength dependent absorption coefficients for some common tissue chromophores [43, 47–55].

Derived Parameters

There are also some derived parameters that are useful to use. These are the albedo and the total attenuation coefficient.

The total attenuation coefficient is defined as the sum of the scattering coefficient and the absorption coefficient:

$$\mu_t = \mu_s + \mu_a \quad (2.21)$$

The albedo, or scattering probability, is defined as the ratio of the scattering coefficient to the total attenuation coefficient:

$$a = \frac{\mu_s}{\mu_a + \mu_s} = \frac{\mu_s}{\mu_t} \quad (2.22)$$

Other Parameters

The preceding subsection described the optical properties that this thesis will use in every chapter. However, there are other optical properties that can be used to define a medium. These other parameters generally are used to model microphysics such as Raman scattering, polarization, fluorescence or reflection/refraction. This section will give a brief overview of these other optical properties.

Fluorescence

Fluorescence occurs when a photon is absorbed by a fluorescent molecule and re-emitted with a new wavelength. Fluorescence is a reactively common phenomena, and is heavily utilised in biophotonics and medicine, to image, or monitor molecules in tissue. Again the optical property that models fluorescence is a coefficient that gives the probability of absorption and re-emission of a photon by a certain molecule. Usually this is in the form of an absorption coefficient or extinction coefficient. The extinction coefficient is a measurement of absorption in terms of the concentration of that absorber. Thus, if a medium has many fluorophores, then the total absorption coefficient is the bulk absorption of the medium plus the contribution from the fluorophores as in Eq. (2.23):

$$\mu_a = \ln(10) \sum_i C_i \varepsilon_i \quad (2.23)$$

Where C_i is the concentration of the i^{th} fluorophore, and ε_i is the extinction coefficient of the i^{th} fluorophore.

Fluorescence will be described in more depth in Chapter 5 and ??.

2.2.3 MCRT Algorithm

This section will provide an in depth description of the MCRT algorithm for the propagating photons thorough a spherical medium with optical properties μ_s , and μ_a . The subsequent section provides details of how the MCRT algorithm is implemented in the Fortran programming language, along with the various code details, such as the parallelisation of the code.

Figure 2.5 shows a flow chart of the MCRT algorithm described in this chapter.

Medium and Grid Set-up

The first step of any MCRT algorithm, is to set-up the medium the photons will propagate through. There are a variety of ways the medium can be set-up. For this section, it is assumed the medium is an isotropic sphere, radius R , and centred at the origin. For simplicity one wavelength is considered, λ . As the MCRT algorithm presented here is run on a 3D Cartesian grid, the grid is setup before creating the spherical medium. The grid is composed of $n_x \times n_y \times n_z$ voxels[†], where each voxel can have its own optical properties. The grid is setup by first setting an array that stores the locations of the voxel boundary walls in the x , y , and z directions. The next step is to setup the actual medium. This is achieved by discretising the medium onto a grid. For this example a sphere is inscribed into a cubic volume, by setting the optical properties of a voxel to that of the medium if the sphere encloses that voxel. The voxels out with sphere are set to that of the ambient medium. An example of a voxelised medium can be seen in Fig. 2.6.

Photon Launch and Initialisation

The second step in the MCRT algorithm, is to initialise the photon. Initialisation of the photon involves setting its initial position and direction. Again, how this is done depends on the experiments being simulated. Here the photon is initialised to the centre of the sphere. The initial direction is sampled isotropically, and set accordingly:

[†]A voxel is a 3D pixel

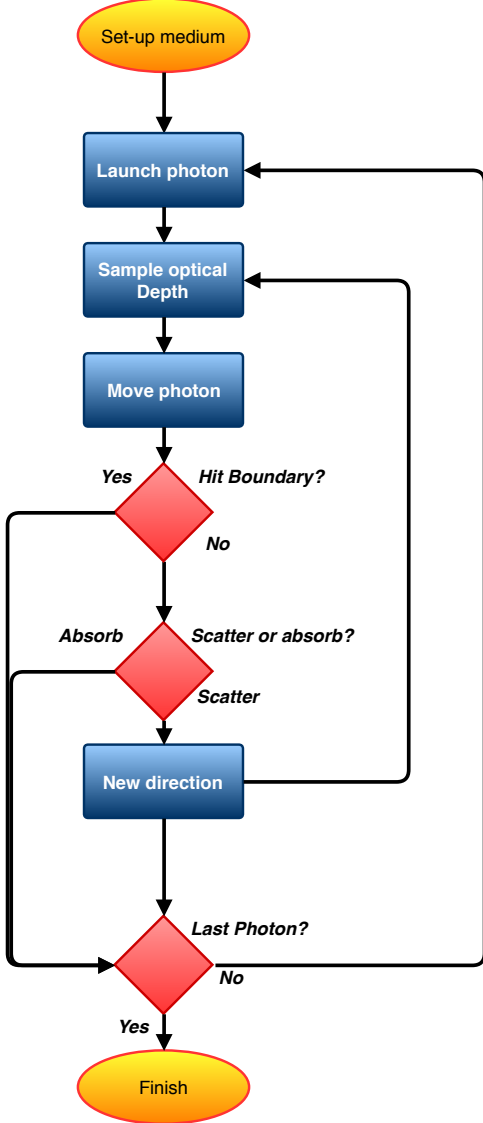


Figure 2.5: Flowchart of the Monte Carlo radiation transport algorithm as described in this section.

$$n_{xp} = \sin \theta \cdot \cos \phi \quad (2.24)$$

$$n_{yp} = \sin \theta \cdot \sin \phi \quad (2.25)$$

$$n_{zp} = \cos \theta \quad (2.26)$$

With θ and ϕ sampled uniformly between $[0, \cos^{-1}(2\xi - 1)]$ and $[0, 2\pi\xi]$ respectively, where ξ is a random number in the range $[0,1)$.

The next step is to launch a photon packet. Depending on the source of photon packets for a given simulation, this step varies from simulation to simulation. The general idea of launching a photon packet is that the packet is given an initial direction vector and position (which consists of a physical position and a voxel position)[‡]:

$$\text{direction} = \begin{bmatrix} n_{xp} \\ n_{yp} \\ n_{zp} \end{bmatrix} \quad (2.27)$$

$$\text{position} = [x_p, y_p, z_p] \quad (2.28)$$

$$\text{voxel} = [x_{cell}, y_{cell}, z_{cell}] \quad (2.29)$$

To set the direction vectors, the components of the direction vectors must be first set. The packets position is tracked using a Cartesian coordinate system, however for ease of computation for calculating scattering angles (see [Photon Interaction Event](#)), the direction vectors are computed in a spherical system thus the direction vectors are in Eqs. (2.24) to (2.26).

θ and ϕ are generated dependent on the photon source used. The individual sine and cosine terms are saved for use in the scattering routines (see [Photon Interaction Event](#)). The position is then set according to the light source used. For this example the photons are released from the origin of the sphere. Using this position the voxel the packet is in is calculated.

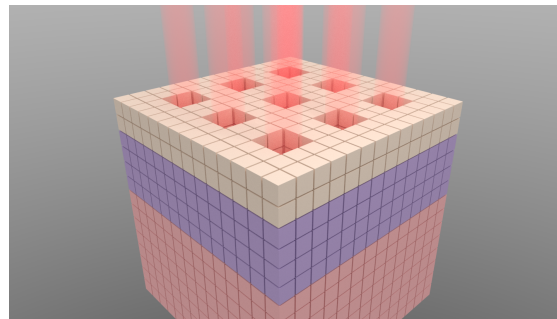


Figure 2.6: Example of a possible voxel model, with three different layers, various holes due to ablative pixel beam lasers (see Chapter 3). Each voxel can represent a different optical/thermal property of the tissue medium.

Photon Propagation

The next step in the algorithm is moving a packet to the next interaction point. The probability a packet will interact over a distance dL is $\mu_t dL$, where μ_t is the total extinction coefficient (see [Optical Properties](#)). Thus, the probability of travelling dL without any interaction is $1 -$

[‡]all variables given in this section are the same as they are in the code.

$\mu_t dL$. Therefore, over a distance L , with N segments of length L/N the probability of travelling L before any interaction:

$$P(L) = (1 - \mu_t \frac{L}{N}) \cdot (1 - \mu_t \frac{L}{N}) \dots (1 - \mu_t \frac{L}{N}) = (1 - \mu_t \frac{L}{N})^N \quad (2.30)$$

$$P(L) = \lim_{N \rightarrow \infty} (1 - \mu_t \frac{L}{N})^N = e^{-\mu_t L} = e^{-\tau} \quad (2.31)$$

Where τ is the number of mean free paths in a distance L . Eq. (2.31) is now a PDF for the distance a packet will travel before an interaction occurs. To be able to get a random optical depth, the PDF has to be able to be sampled from either analytically or via the rejection method. Using the Monte Carlo method described in Section 1.1, with ξ as our random number, gives:

$$\xi = \int_0^\tau e^{-\tau'} = 1 - e^{-\tau} \rightarrow \tau = -\ln(1 - \xi) \quad (2.32)$$

As ξ is symmetric about 0.5, $1 - \xi$ can be substituted for ξ yielding:

$$\tau = -\ln(\xi) \quad (2.33)$$

τ is now the optical distance, however this needs to be converted into a physical distance so that the photon packet can be moved. From our definition of τ we know that $\tau = \int_0^L \mu_t dS$, and if the medium is smooth and homogeneous (i.e not a gridded medium):

$$L = \frac{\tau}{\mu_t} \quad (2.34)$$

Therefore, to update the packets position it is simply:

$$x_p = x_p + L \cdot n_{xp} \quad (2.35)$$

$$y_p = y_p + L \cdot n_{yp} \quad (2.36)$$

$$z_p = z_p + L \cdot n_{zp} \quad (2.37)$$

However, as the code in this thesis is a 3D gridded Cartesian code, the method of updating and moving the packets position is slightly adjusted. As stated in Medium and Grid Set-up, the medium has been discretised onto a grid, so that each voxel can have a different μ_t , thus Eq. (2.34) becomes:

$$L = \frac{\tau}{\mu_{t,\zeta}} \quad \zeta = (x, y, z) \quad (2.38)$$

with $\mu_{t,\zeta}$ the μ_t for the ζ^{th} voxel.

Moving the photon through a voxelised medium is more involved than propagating a photon through a non voxelised medium. This is because the voxel the photon is in needs to be updated as the photon moves from voxel to voxel. The first step of moving the photon through a voxelised medium is drawing a random optical depth. This optical depth will be the full optical depth the photon travels before an interaction event. The generation of a random optical depth is as outlined above, $\tau = -\log(\xi)$. As the photon travels through the voxel grid, a running total of the current optical distance travelled is kept. This is then compared to the randomly generated optical depth. When the running total optical depth equals the randomly generated optical depth the photon propagation is stopped, and the photon undergoes an interaction.

We then calculate the distance to the nearest voxel boundary in the x , y , and z directions. The distance is calculated for each direction. Equation (2.39) shows for the x direction:

$$d_x = \frac{x_{face} - x_{cur}}{n_{xp}} \quad (2.39)$$

Where d_x is the distance to the nearest wall in the x direction. x_{face} is the voxel wall position in the x direction, and n_{xp} is the x direction vector. With three distances calculated, $[d_x, d_y, d_z]$, the minimum of these is thus the distance to the nearest voxel wall.

The next step is to calculate the optical depth for this distance. The optical depth is found by rearranging Eq. (2.38) for τ , with L now the distance to the nearest wall. With the optical distance to the nearest wall calculated, the next step is to determine if there is “enough” optical distance left to travel the full distance to the nearest wall. Therefore, the running total optical distance is compared to the randomly generated optical distance. If the running total + the new optical distance to the nearest wall, is less than the randomly generated optical depth, then the photon travels to the nearest wall. The photon is then placed in the next voxel by a distance δ , where δ is just larger than machine precision. If the running total + the new optical distance to the nearest wall is greater than the generated optical distance then an interaction event occurs in the current voxel. The distance to the interaction event is calculated and the photon moved to this location.

Figure 2.7 illustrates this whole process for a 2D example.

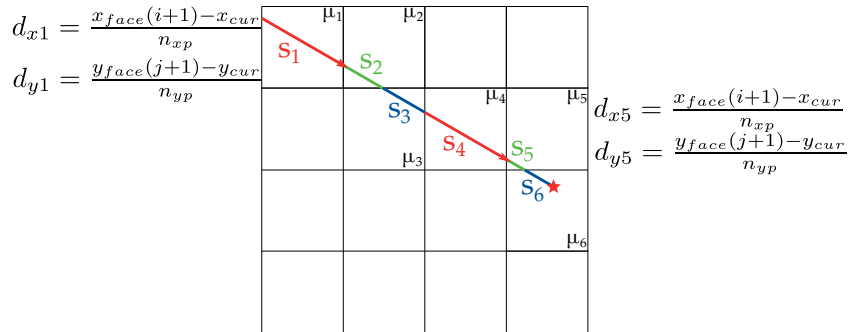


Figure 2.7: Illustration of photon propagation through a 2D grid. d_{x1} , and d_{y1} are the distances to the voxel walls in the x and y directions in the μ_1 voxel. In this case $S_1 = d_{x1}$ as d_{x1} is smaller than d_{y1} , thus the photon hits the voxel wall in the x direction. For the μ_5 voxel, d_y is smaller, thus the photon hits the voxel wall in the y^{th} direction.

This whole process is repeated until the photon undergoes an interaction event or leaves the voxel medium. The next step in the algorithm is the interaction event, which can consist of either: scattering, absorbing or another microphysics phenomena.

Photon Interaction Event

The next section of the algorithm is to decide how the photon interacts with the medium, either via scattering or absorption. There are other interaction events that can occur, however descriptions of these are left for the chapters that detail these behaviours.

To decide whether a packet scatters or absorbs, a random number, ξ , is generated and compared against the albedo, a . If $\xi < a$ then the packet scatters, otherwise it is absorbed.

Packet Absorption

If the interaction event is a photon packet absorption, then the algorithm terminates the photon packets and starts the next photon packet, see [Termination](#).

Packet Scattering

If the interaction event is a packet scattering, then the packet is scattered into a new direction and the above processes are carried out until a termination clause is met, see [Termination](#).

Depending on the medium being simulated, it can either be isotropic or anisotropic scattering. For the isotropic case, new $\cos(\theta)$ and ϕ angles are sampled uniformly, and the direction vectors set as in section [Photon Launch and Initialisation](#). For the case where the scattering is anisotropic the calculation of the scattering angles, θ and ϕ , is more complicated. The random sampling of the scattering angles, θ and ϕ , are valid in the “centre of mass” frame containing the scatter, incident and scattered ray. The photons position is updated in the lab frame, thus the direction vectors also have to be updated in the lab frame. This means that the scattering angles need to be rotated into the lab frame. For the isotropic case assume that the scattering is also isotropic in the lab frame, thus the new direction vector is easily calculated. However, this is not the case for anisotropic scattering, as the centre of mass frame has to be rotated into the lab frame.

Figure 2.8 and Eq. (2.40) show how this process is achieved. Where $\mathbf{n} = (n_x, n_y, n_z)$, $\mathbf{n}_s = (n_x^{new}, n_y^{new}, n_z^{new})$, θ_s is chosen from the phase function Eq. (2.41), and $\varphi_s = 2\pi\xi$ with ξ being a random number in the range 0 to 1.

$$\begin{aligned} n_x^{new} &= \frac{\sin\theta_s}{\sin\theta} (n_x n_y \cos\varphi_s - n_y \sin\phi_s) + n_x \cos\theta_s \\ n_y^{new} &= \frac{\sin\theta_s}{\sin\theta} (n_y n_z \cos\varphi_s + n_x \sin\phi_s) + n_y \cos\theta_s \\ n_z^{new} &= -\sin\theta_s \cos\varphi_s + n_z \cos\theta_s \end{aligned} \quad (2.40)$$

$$\cos\theta_s = \frac{1 + g^2 - \left(\frac{1-g^2}{(1-g+2g\xi)^{3/2}} \right)^2}{2g} \quad (2.41)$$

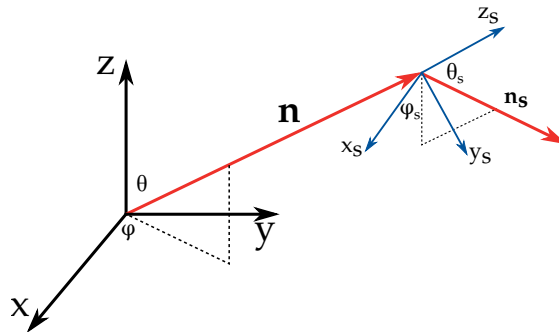


Figure 2.8: Illustration of rotating the centre of mass frame to the lab frame. \mathbf{n} is the direction vector of the photon before scattering, and \mathbf{n}_s is the scattered direction vector. θ and φ are the scattering angles. z_s is in the same direction as \mathbf{n} .

Termination

The final section of the MCRT algorithm is to check if it should be terminated. This is a simple check to see if there are any more photons to run. If there are more photons to run then the algorithm goes back to the [Photon Launch and Initialisation](#) section and continues from there. If there are no more photons the algorithm terminates and any results are written out.

Scored Quantities

As MCRT is a computational method, a wealth of information is able to be recorded during the simulation. From the paths of individual photons, to average scattering angles and more. However, it is not practical to record all this information for every simulation, as this would lead to inefficient simulations, and expensive data storage solutions. Thus, for a given problem only the pertinent information is stored.

One important recorded variable is fluence. Fluence is the number of photons entering a sphere per unit cross section area [10]. In practice the average fluence per area is used, Eq. (2.42), as this is easier to calculate in an MCRT code. Lucy showed that the average fluence per area is proportional to the sum of the path length through a volume [56]:

$$J_i = \frac{L}{NV_\varsigma} \sum l \quad (2.42)$$

Where:

J_i is the mean intensity such that the fluence is $\Phi = 4\pi J [W m^{-2}]$;

L is the luminosity or power of the light source [W];

N is the total number of photon packets [-];

V_ς is the volume of the ς^{th} voxel [m^3];

and l is the path length of a photon packet through the ς^{th} voxel [m].

Most chapters in this thesis make use of Eq. (2.42) or modified versions of it as the main scored quantity, e.g. to determine absorbed energy.

Other common scored quantities are the exit location of a photon, the wavelength of an exiting photon or the distribution of photon packet absorption.

2.2.4 Code Details

This section describes the implementation of the MCRT and of the parallelisation the code.

Code

All code in this thesis is written in modern Fortran[§]. All subroutines and functions are contained in modules (with the exception of the main program—main.f90). This is done to be able to “hide” data from subroutines and functions, and to arrange the code that relates to other parts of the code in the same file. Having the code in modules also allows the use of runtime allocation of memory for arrays. This enables the user to specify the size of arrays depending on the need of the user for the problem at hand.

Modules are classified into three different types: data, routines, and dependencies. Data modules are modules that contain no function or routines, but store variables that can be accessed anywhere in the program when required. Routine modules contain the subroutines and functions

[§]modern Fortran is considered anything past Fortran 95 [57].

used in the code. Finally dependency modules are the modules that have not been written by me, and thus the code depends upon them to run.

Figure 2.9 show the relationship between the various modules, for a basic version of the MCRT as described in [MCRT Algorithm](#).

Using Fig. 2.9 as a reference each module contains:

`mepolar.f90` is the entry point of the code. It calls all other subroutines and functions, as well as setting up various variables and printing progress.

`ch_opt` is the module where the optical properties are set or changed.

`gridset_mod` is where the optical properties grid and voxel walls are set.

`subs` contains general purpose routines that are used in various different parts of the code.

`writer_mod` contains routines that write out the results of the simulation.

`inttau2` is the module that contains the routines that propagate the photon through the voxel grid.

`sourcph_mod` contains the routines that initialise the photon position and direction.

`stokes_mod` contains the routine that calculates the scattering direction after a scattering event.

`iarray` is a data module that contains all the arrays in the code.

`constants` is a data module that contains all the constants and filepaths needed in the code.

`ieee_arithmetic` is an external dependency that gives various arithmetic checking routines such as `is_nan()`.

`vector_class` is a module that contains the vector type, and all its associated operations such as cross and dot products of vectors.

`photon_vars` is a data module that contains the data pertaining to each photon, such as wavelength or energy.

Finally, `opt_prop` contains the data about the current optical properties such as the albedo and absorption coefficient.

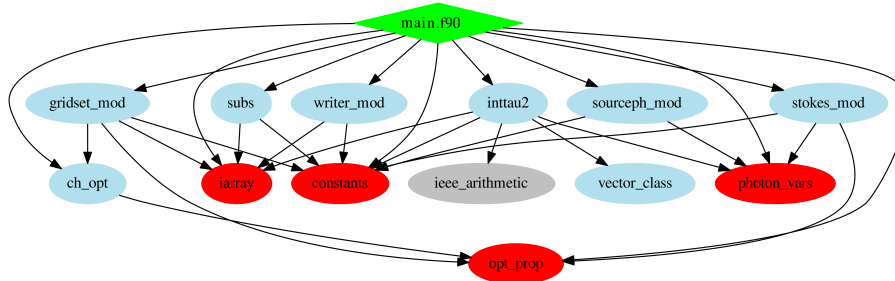


Figure 2.9: Source code hierarchy, showing the relationship between different modules. Green is the entry point for the simulation. Red are the data modules, light blue are the routine modules, and grey are the external dependencies.

Parallelisation of the MCRT Algorithm

As mentioned in the previous sections, MCRT can be computationally intensive, especially when dealing with highly scattering mediums. Fluorescence can also cause simulations times to dras-

tically increase as photons are no longer “killed” off, but rather re-emitted at a new wavelength. Other optical processes such as Raman scattering are highly unlikely events, which again can lead to a dramatic increase in simulation times, as many photons are required to be simulated to get “good” statistics.

Fortunately MCRT is classed as an “embarrassingly parallel” problem[¶]. This means that it is trivial to parallelise in comparison to other algorithms. The reason that MCRT is classed as “embarrassingly parallel”, is that the algorithm can be split up onto separate processors, with little need for communication between them. In reality this means that n copies of the algorithm can run on n cores in a processor, with communication taking place at the start and end of each simulation run.

All the code in this thesis is parallelised using Message-passing interface (MPI) [59, 60], with the only communication taking place at the end, where the results are collated on to all processes. The one exception to this is in Chapter 3, where the heat diffusion calculation needs communication between the processes during the calculation.

The parallel efficiency of a code depends on the problem and the number of photon packets run. To determine the speedup of a given problem, Amdahl’s law is used [61]:

$$speedup = \frac{1}{(1 - P) + P/N} \quad (2.43)$$

Where P is the fraction of the code that is parallel, and N is the number of cores the code is run on. The consequence of Amdahl’s law is as N tends to infinity the speedup tends to a maximum:

$$speedup_{max} = \frac{1}{1 - P} \quad (2.44)$$

The value of P varies from problem to problem and the number of photon packets run. Figure 2.10 shows the results of the profiling of the code, for various numbers of cores. This test consisted of running the same number of photons, in a highly scattering medium of size 2 cm^3 . This yielded a P of 0.999010 ± 0.000045 and a maximum speedup of 1010.1.

[¶]However, this is not true for all MCRT applications. For example, using the Bjorkman & Wood [58] immediate temperature corrections method, turns MCRT into a different class of parallel problem [19].

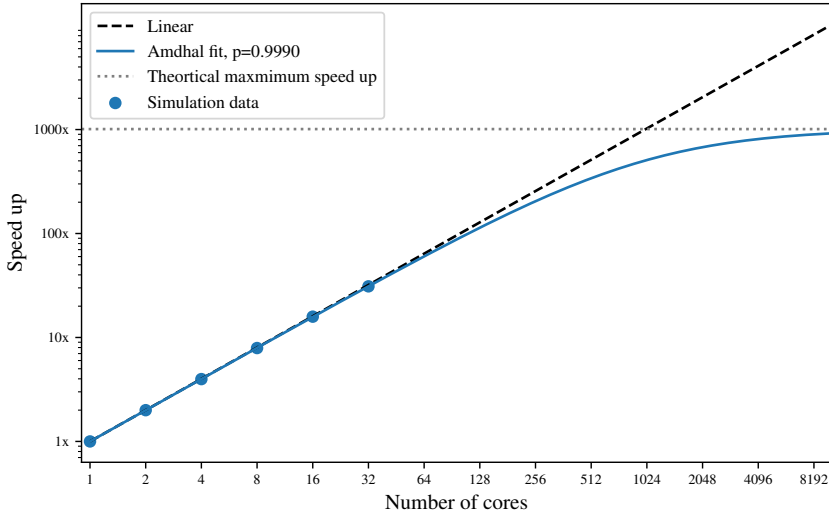


Figure 2.10: Performance of the parallelisation of the MCRT code using MPI.

2.3 Validation of MCRT Code

As the Monte Carlo method is an algorithm that depends upon random numbers, it is sometimes hard to ensure the correct result is obtained. Or to put it another way:

“Monte Carlo is easy to do wrong!” G.W. Collins III [62]

Thus, the code has to be validated against various theoretical/experimental and other simulations, to determine whether the results are correct.

The main benchmark of the MCRT code is a comparison against an expression for fluence as a function of depth [63]. This expression has also been fitted to by other MCRT simulations [64].

$$\Psi(z) = \Psi_0(C_1 e^{-k_1 z/\delta} - C_2 e^{-k_2 z/\delta}) \quad (2.45)$$

Where:

$\Psi(z)$ is the penetration of the incident light, or equivalently the fluence rate [$W\text{ cm}^{-2}$];

Ψ_0 is a normalisation constant [$W\text{ cm}^{-2}$];

C_n and k_n are fitted coefficients [-];

and δ is the optical penetration depth, defined as $\delta = 1/\sqrt{3\mu_a(\mu_a + \mu_s(1-g))}$, [cm].

Jacques *et al.*, in their simulation used two different wavelengths, 420 nm and 630 nm. The medium in the simulation is a infinitely wide slab with a depth of 1 cm, with uniform optical properties. The medium has a refractive index of 1.38. The g value is in the range 0.7 — 0.9, and the optical properties are as in Table 2.1.

Wavelength/nm	Absorption	Scattering	Penetration				δ/cm
	μ_a/cm^{-1}	$\mu_s(1-g)/cm^{-1}$	C1	k1	C2	k2	
420	1.8	82	5.76	1.00	1.31	10.2	0.047
630	0.23	21	6.27	1.00	1.18	14.4	0.261

Table 2.1: Table of optical properties and determined coefficients from Jacques *et al.* [64].

Using these values Jacques *et al.* calculated values for C_1 , C_2 , k_1 and k_2 using their MCRT code. The above optical properties and medium dimensions^{||} are recreated in the code and a value of 0.9 was chosen for g . 8 million photons were run for the simulation. This yielded the result as in Fig. 2.11.

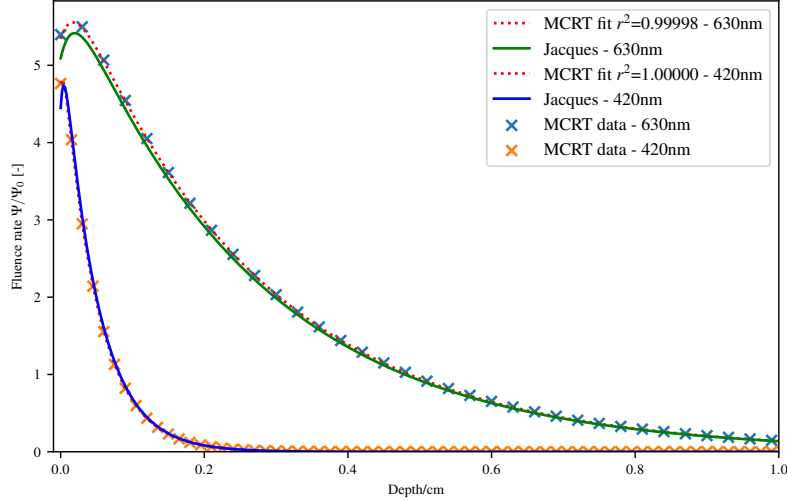


Figure 2.11: Figure shows the fluence as a function of depth. Figure also shows comparison to the Jacques MCRT simulation and the MCRT as described in this chapter.

Fitting Eq. (2.45) to the data calculated by our MCRT code for 630 nm, gave: $C_1 = 6.425$, $C_2 = 1.083$, $k_1 = 1.0$, and $k_2 = 12.966$. For 420 nm gave: $C_1 = 5.600$, $C_2 = 0.838$, $k_1 = 1.003$, and $k_2 = 9.846$. These are in good agreement (with in code differences) with Jacques *et al.* results.

2.4 Conclusion

There are various methods available to model the radiative transport equation. MCRT is the most flexible of the methods available, allowing arbitrary geometries, light sources, multiple anisotropic scattering, and various microphysics to be modelled. This chapter presented an overview of the MCRT algorithm that will be the basis of the results presented in the following chapters. The code described in this chapter is based upon K. Wood's **MCRT** code for light propagation in galactic dust clouds. It has been modernised to modern Fortran and adapted so that the code can model biological tissue so that the code can be applied to various medical and biophotonic problems. The optical properties required in a MCRT simulation have been discussed, and will be utilised to subsequent chapters. A description of how the code has been parallelised and validated against a standard literature code has also been presented.

^{||}The infinitely wide slab is implemented so that when a photon leaves one of the sides of the voxel grid, it is moved to the other side of the grid, retaining its original direction vectors.

Chapter 3

Computational Modelling of Tissue Ablation

3.1 Introduction and Background

This chapter uses MCRT techniques coupled to a heat transfer simulation, to study the thermal damage to tissue due to a laser, with its power spread over many beams to leave viable tissue around zones of damaged/necrotic tissue [65]. This class of laser is called a fractionated ablative laser. This chapter presents experimental work carried out on porcine tissue by our collaborators at the University of Dundee and the photobiology department at Ninewells Hospital, along side my computational model of tissue ablation.

Ablative lasers are used in a wide variety of medical procedures including: coagulating scalpels, port wine stain removal, tattoo removal, hair removal, and skin rejuvenation [66–70]. One class of laser used in these procedures are ablative lasers. Ablative lasers are usually high powered lasers ($>30\text{ W}$) targeted at a specific chromophore in the skin, to partially or fully remove layers of skin. These types of lasers are commonly used for aesthetic procedures such as: skin rejuvenation [70], and removal of various diseases such as Rhinophyma [71] or lesions/nodules [72]. Ablative lasers have also been recently investigated as a means of better drug penetration into the skin for various therapies such as photo-dynamic therapy (PDT). The ablative laser “drills” holes in the skin, which allows topical treatments to better diffuse into the skin [73].

One downside to using lasers to remove tissue, is that unlike a scalpel where the surgeon has full control of the depth of the incision, ablative lasers are not as predictable. Lasers can cause thermal damage to the surrounding areas, leading to potentially unwanted effects, though some applications of ablative lasers utilise the thermal damage, particularly aesthetic procedures [74].

Currently, the only reliable method to measure the depth of the ablative holes, is via a biopsy, which is an invasive procedure. In this work an optical coherence tomography (OCT) system is used to measure the ablative crater non-invasively *in-vivo*. The OCT measurements are then compared to a computational model developed as part of this project. It is hoped this computational model could be used to predict the depth of the ablative crater when using a certain laser power for various different applications such as: laser assisted drug delivery, and various cosmetic applications.

3.2 Methods

To replicate the experimental work *in silico*, the numerical model has three main portions. The first is the MCRT code that models light transport through tissue so that we can calculate the laser energy deposited as a function of time and space. The second, a finite difference method (FDM) which is used to calculate the heat diffusion within the tissue due to the absorbed laser energy. Finally, a tissue damage model to track the tissue damage caused by the laser. All these individual functions are connected together to create a full numerical model.

3.2.1 Monte Carlo radiation transport (MCRT)

MCRT is used here to calculate the energy deposited by the laser. This is then passed to the heat transport simulation, which calculates the heat diffusion in the medium. The algorithm for the three coupled simulations is presented in Fig. 3.1.

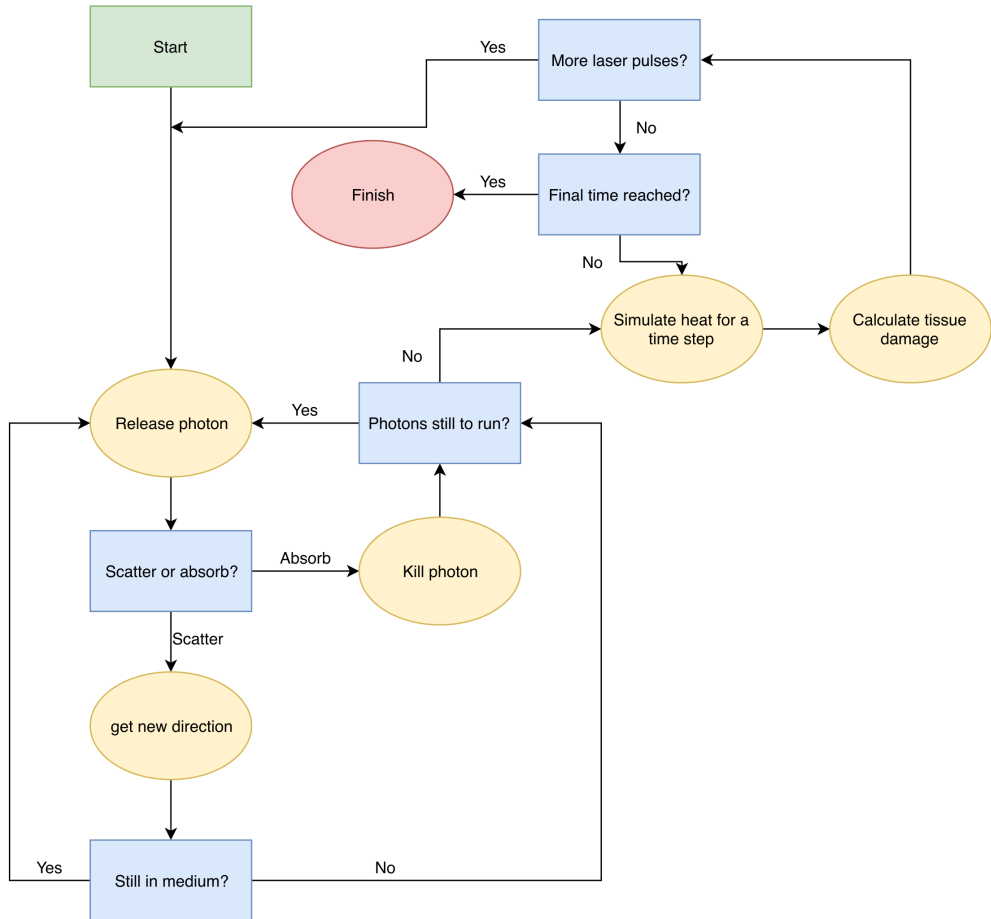


Figure 3.1: Flowchart of the tissue ablation algorithm.

The MCRT algorithm is largely the same as described in Chapter 2, with some important adjustments.

The first adjustment is that the path length counter for fluence is changed to track absorbed energy. This is achieved by multiplying the pathlength in a voxel by the absorption coefficient of that voxel. Figure 3.2 show this process graphically, and Equation (3.34) shows the mathematical expression:

$$E_i^{abs} = \frac{P}{NV_i} \sum \mu_{a,i} s \quad (3.1)$$

Where:

- E_i^{abs} is the energy absorbed in the i^{th} voxel [$J s^{-1} m^{-3}$];
- P is power [W];
- N is the number of packets, representing a power, P;
- V_i is the volume of the i^{th} voxel [m^{-3}];
- $\mu_{a,i}$ is the absorption coefficient of the i^{th} voxel [cm^{-1}];
- and s is the pathlength of a packet through the i^{th} voxel [cm].

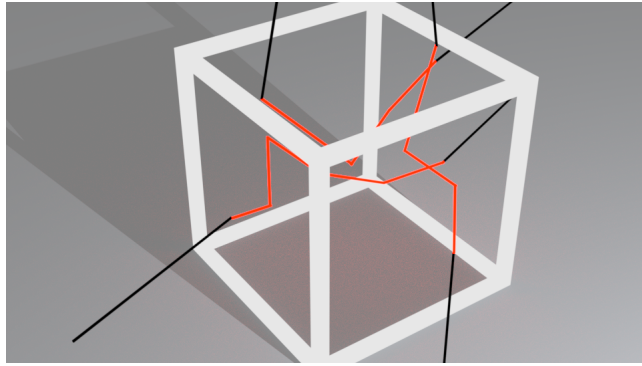


Figure 3.2: Red lines are packet paths within a voxel. Black lines packet paths out with the voxel. Red packet paths, weighted by μ_a , are summed up to calculate the absorbed energy within each voxel.

This grid of absorbed energy is then passed to the heat transport portion of the simulation, so that the heat diffusion in the porcine tissue can be calculated.

The next adjustment to the MCRT algorithm is that the MCRT algorithm is run for every heat simulation time step, as the medium could change at every time step due to the optical, and thermal properties changing as a function of tissue damage.

Finally, to match the experiment undertaken the medium and laser for the *in-silico* experiments must match the practical experiments. As the laser used in the experiments emits an infra-red wavelength ($10.6 \mu m$), the optical properties are dominated by the water content of the tissue. Due to this it is assumed that there is just absorption in the medium, with no scattering. Further discussion can be found in Section 3.3.1. The laser in some of the *in silico* modelling, has multiple beams and the source photon packet routine is adjusted to accommodate this when needed.

3.2.2 Heat Transport

The diffusion of heat can be modelled using the heat equation (Eq. (3.2)), which is derived from Fourier's law and the principle of conservation of energy [75]. The standard heat equation is a partial differential equation of the parabolic form. Solutions and analytical methods are readily

available for lower dimensions (i.e. 1D heat diffusion), but for higher dimensions, numerical models must be used for all except the simplest problems. The simplest form of the heat equation is shown below:

$$\rho c_p \frac{\partial T}{\partial t} = \nabla \cdot (\kappa \nabla T) + \dot{q} \quad (3.2)$$

Where:

- $T(x, y, z, t)$ is the temperature as a function of time and space [K];
- κ is the thermal conductivity [$Wm^{-1}K^{-1}$];
- ρ is the density [Kgm^{-3}];
- c_p the specific heat capacity [JK^{-1}];
- $\dot{q}(x, y, z, t)$ is the source/sink term as a function of time and space [Wm^{-3}].

Equation (3.2) is for a homogeneous system where the thermal properties do not change as a function of time, space and temperature. However, to model a moving ablation front the nonlinear heat equation must be used, where the thermal properties can be a function of time, space and temperature (Eq. (3.3)).

$$\frac{\partial T}{\partial t} = \frac{1}{(\rho c_p)_\xi} (\nabla k_\xi T + k_\xi \nabla^2 T) + \dot{q}, \quad \text{where } \xi = (i, j, k) \quad (3.3)$$

Included in Eq. (3.3) is a source and sink term, \dot{q} , to allow the modelling of heat loss/gain from external sources/sinks. The heat source in this simulation is due to the laser, and it is assumed that the only loss of heat to the surrounding medium is via conduction.

The medium is considered to be at a constant temperature of 5°C, as the porcine skin was kept cooled prior to experimental work and the simulation volume is smaller than the porcine tissue samples.

Where:

- h is the heat transfer coefficient [$Wm^{-2}K$];
- A is the area of the grid element, that is radiating/convicting heat away [m^{-2}];
- and T , and T_∞ are the temperature in a voxel and the surrounding medium temperature respectively [K].

As Eq. (3.3) is generally hard to solve in arbitrary geometries with complex boundary conditions, a numerical method is employed to solve it. The numerical method employed is a FDM, derived from the Taylor series, see Eq. (3.4).

A function $f(x)$ is discretised onto a grid with N nodes a distance Δx apart. Equation (3.4) is then truncated and rearranged and it is assumed that the remainder term R_1 is sufficiently small enough, to yield an approximation for the first derivative of a function $f(x)$ at a point $x_0 + \Delta x$, see Eq. (3.5). Equation (3.5) is the so called forward difference, due to it using a point in the “forward” direction. The “backward” and central difference terms can be calculated by using a node at $x_0 - \Delta x$ for the backward difference Eq. (3.6b). The central difference (Eq. (3.6c)) is an average of the forward and backward differences. Expressions can also be given for the 2nd derivatives for backward, forward and central (forward and backward 2nd order equations omitted for brevity) Eq. (3.6d).

$$f(x_0 + \Delta x) = f(x_0) + \frac{f'(x_0)}{1!} \Delta x + \frac{f''(x_0)}{2!} \Delta x^2 + \dots + \frac{f^{(n)}(x_0)}{n!} \Delta x^n + R_n(x) \quad (3.4)$$

$$f'(x_0) \approx \frac{f(x_0 + \Delta x) - f(x_0)}{\Delta x} \quad (3.5)$$

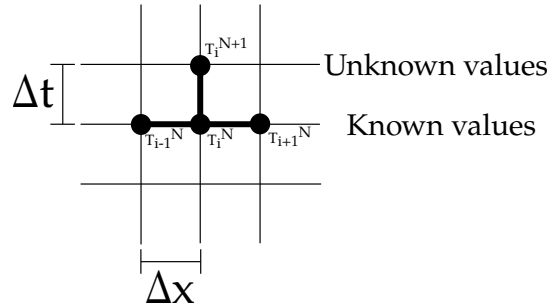


Figure 3.3: Finite difference method stencil for simple explicit scheme.

$$\frac{df}{dx} = \frac{f_{i+1} - f_i}{\Delta x} \quad (\text{forward}) \quad (3.6a)$$

$$\frac{df}{dx} = \frac{f_i - f_{i-1}}{\Delta x} \quad (\text{backward}) \quad (3.6b)$$

$$\frac{df}{dx} = \frac{f_{i+1} - f_{i-1}}{2\Delta x} \quad (\text{central}) \quad (3.6c)$$

$$\frac{d^2f}{dx^2} = \frac{f_{i-1} - 2f_i + f_{i+1}}{\Delta x^2} \quad (\text{central}) \quad (3.6d)$$

Thus, the linear heat equation Eq. (3.2), in 1D, taking a 1st order forward time derivative, and a 2nd order central spatial derivative gives:

$$\frac{T_i^{n+1} - T_i^n}{\Delta t} = \alpha \frac{T_{i-1}^n - T_i^n + T_{i+1}^n}{\Delta x^2} + \frac{\dot{q}}{\rho c_p} \quad (3.7a)$$

$$T_i^{n+1} = \alpha \Delta t \frac{T_{i-1}^n - 2T_i^n + T_{i+1}^n}{\Delta x^2} + \frac{\Delta t \dot{q}}{\rho c_p} \quad (3.7b)$$

Where $\alpha = \frac{\kappa}{\rho c}$.

Equation (3.7b) is called the “simple explicit form of finite-difference approximation” [76]. Figure 3.3 shows the “stencil” of this scheme, where there are three known points at time N , and just one unknown at time $N+1$. There are various other schemes that can be used to calculate the temperature at the next time step. However, a simple explicit scheme is used here, due to its ease of implementation despite there being a constraint on the stability in comparison to an implicit method. This method is also easily scaled up to 3D with little difficulty.

For the more complicated nonlinear heat equation there is a possibility that the medium is not continuously smooth between nodes, in terms of optical and thermal properties. The two easiest methods [76] of achieving this are: (1), lag the value behind by one step, i.e $c_p^{n+1} = c_p^n$. (2), average κ , ρ , and c_p using a half difference scheme where the thermal property used in the calculation is the thermal property half way between two nodes, i.e the average of the two nodes:

*For brevity $f(x_0 + \Delta x)$ is defined as f_{i+1} , and $f(x_0 - \Delta x)$ as f_{i-1} , etc.

$$\kappa^\pm = \frac{\kappa_i + \kappa_{i\pm 1}}{2} \quad (3.8)$$

$$\rho^\pm = \frac{\rho_i + \rho_{i\pm 1}}{2} \quad (3.9)$$

$$c_p^\pm = \frac{c_{p,i} + c_{p,i\pm 1}}{2} \quad (3.10)$$

Thus, for the simple 1D case as in Eq. (3.7b), the thermal properties are averaged between nodes when computing the coefficients of the temperature nodes, and lag the thermal properties when adding the heat from the laser:

$$T^{N+1} = \Delta t (AT_{i-1}^N - 2BT_i^N + DT_{i+1}^N) + T_i^N + \frac{\Delta t}{\rho c_p} q_L \quad (3.11)$$

Where (in the x direction):

$$\begin{aligned} A &= \frac{\kappa^-}{\rho^- c_p^- 2\Delta x^2} \\ B &= \frac{\kappa^+}{\rho^+ c_p^+ 2\Delta x^2} \\ D &= \frac{(A + B)}{2} \end{aligned} \quad (3.12)$$

Equation (3.11) is straightforward to generalise to higher dimensions. The 3D case gives:

$$U_{xx} = (AT_{i-1,j,k}^N - 2BT_{i,j,k}^N + DT_{i+1,j,k}^N) \quad (3.13)$$

$$U_{yy} = (AT_{i,j-1,k}^N - 2BT_{i,j,k}^N + DT_{i,j+1,k}^N) \quad (3.14)$$

$$U_{zz} = (AT_{i,j,k-1}^N - 2BT_{i,j,k}^N + DT_{i,j,k+1}^N) \quad (3.15)$$

$$T_{i,j,k}^{N+1} = \Delta t (U_{xx} + U_{yy} + U_{zz}) + T_{i,j,k}^N + \frac{\Delta t}{\rho c_p} q_L \quad (3.16)$$

Where:

$T_{i,j,k}^{N+1}$ is the new temperature at node i, j, k [K];

$T_{i,j,k}^N$ is the temperature at node i, j, k at the current time step [K];

α is the thermal diffusivity [$m^2 s^{-1}$];

κ is the thermal conductivity [W/mK];

Δx etc. is the size of the grid element in the p^{th} direction [m];

and A, B, D are the coefficients in their respective dimension (Eq. (3.12)).

Equation (3.16) gives the full numerical solution to the nonlinear heat equation with a laser heat source. This will allow the calculation of the heat diffusion in the porcine tissue due to laser heating.

As the laser used in the experimental work operates in a pulsed mode, this is accounted for in the simulation. The laser pulse shape is a triangular pulse, with the peak power, P_{peak} , and pulse length, τ [77]. In the heat simulation there has to be an additional variable in the term $laserOn(t) \cdot \frac{\alpha \Delta t}{\kappa} q_L$ in Eq. (3.16). This additional variable, $laserOn(t)$, is a boolean value and a function of time, which is defined as:

$$laserOn = \begin{cases} 1, & \text{Laser on} \\ 0, & \text{Laser off.} \end{cases}$$

In the instance where there is a train of laser pulses, the laser is turned on and off based upon the pulse frequency.

Due to a simple explicit FDM being used, the time step is constrained to make the solution stable. For a cubic 3D FDM without prescribed flux boundary conditions, this yields the constraint: $\Delta t \leq \frac{1}{\delta\alpha}$ where $\delta = \frac{1}{\Delta x^2} + \frac{1}{\Delta y^2} + \frac{1}{\Delta z^2}$. Along with this time constraint, the pulse length of the laser also has to be considered. If the time step of the heat simulation is too large it will not account for the heat deposited by the laser. Thus, the timestep has to be at least an order of magnitude smaller than the shortest laser pulse.

As the time step is small, and the grid resolution large, the resultant simulation is slow. Thus, the code has been fully parallelised to improve performance. Both the MCRT and heat simulation are independently parallelised.

Parallelisation of the heat simulation is more involved than the “embarrassingly parallel” class of problems where MCRT belongs. This is due to the heat simulation being dependent on neighbouring nodes to update the temperature at the current node. Thus, if the medium were to be split up on to separate cores, there would have to be communication between the cores, in order for the simulation to be completed successfully. Therefore it is not possible to take the “easy” route of running the simulation concurrently N times and collating the result at the end of all the simulations.

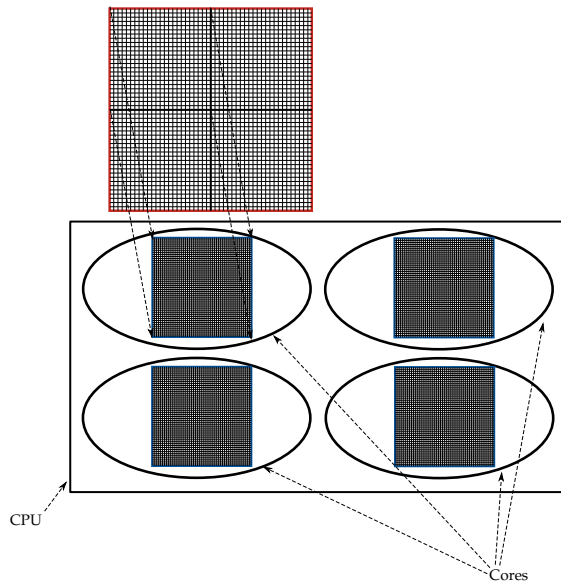


Figure 3.4: Computational domain decomposition. Total computational domain (red outline) is evenly divided between cores in the CPU. This is done via layers of the domain in the z direction. Information is passed to/from cores via the “halo swap” process (see Fig. 3.5).

The heat simulation is parallelised using a technique called “halo swapping”. This involves splitting up the computational domain (see Fig. 3.4), in this case the tissue medium, and doing the calculations on each domain on a separate core. The “halo swapping” comes in when cores

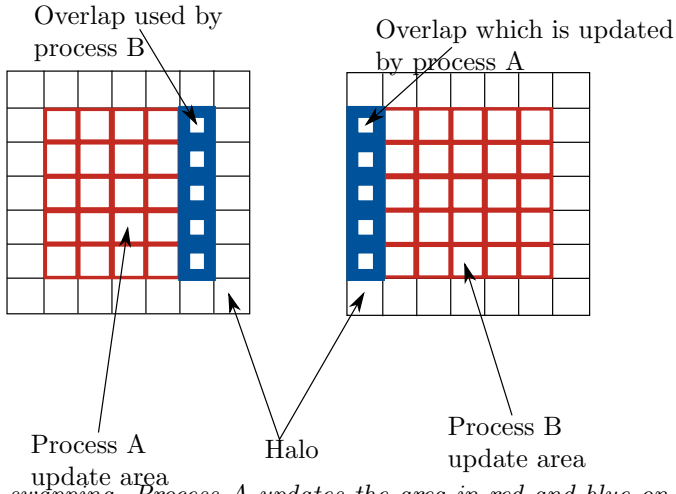


Figure 3.5: Halo swapping. Process A updates the area in red and blue on the left. It updates the blue area which is sent to process B as B’s “halo”. Process B cannot update its own halo, but rather updates the halo for process A.

need to communicate with each other about updating their boundary temperature nodes (see Fig. 3.5).

Figure 3.6 shows the speed up gained from using the technique. The “halo swapping” technique is efficient for situations where the computational domain can be split up with large “chunks” being calculated on each core. However, if the computational domain is small, and the number of cores large then bottlenecks occur due to too much communication between cores taking place. Thus, to efficiently use “halo swapping” careful thought has to be given to the size of the computational domain, and the number of cores running the simulation. Evidence of this bottlenecking can be seen in Fig. 3.6 for problems where the size of the grid, in voxels, is 40^3 and 24^3 . These problems also show superlinear speed up, for certain number of cores. This is not unfeasible, due to several reasons, in particular the underlying computer architecture [78].

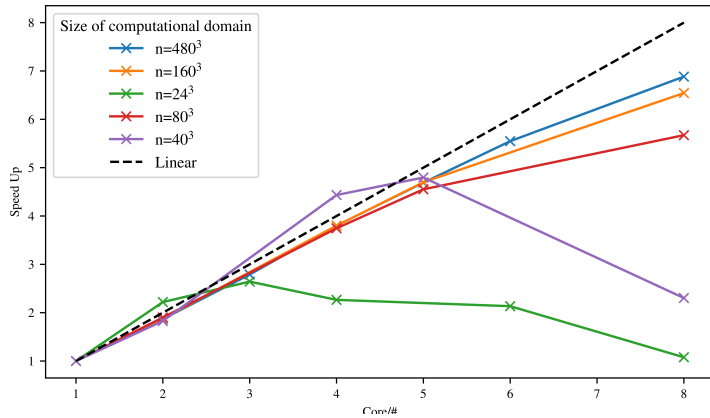


Figure 3.6: Figure shows the speed up gained by parallelisation of the heat simulation using the “halo swapping” technique, for various sizes of computational domain (voxels). Data taken from a Intel Xeon E3-1245 v5, 8 cores @ 3.5GHz machine.

After one time step of the heat simulation has been completed, the temperature grid is

passed to the tissue damage portion of the simulation to calculate the tissue damage that may have accrued during the heat simulation time step.

3.2.3 Tissue Damage

Introduction

The final portion of the simulation is the tissue damage model. To be able to model damage to the tissue, the process tissue undergoes upon heating due to the laser needs to be able to be described.

When the laser is turned on, the temperature starts to rise within the tissue due to the absorption of photons by the tissue. The temperature rise causes damage to the tissue when above a threshold temperature, T_d , approximately 43°C [79]. From the temperature, T_d , four main areas of tissue damage are defined:

$$T = \begin{cases} \text{coagulation,} & T_d \leq T \leq 100^\circ\text{C} \\ \text{water boils,} & T = 100^\circ\text{C} \\ \text{carbonisation,} & 100^\circ\text{C} \leq T \leq T_a \\ \text{ablation,} & T = T_a. \end{cases} \quad (3.17)$$

The area of tissue damage termed “coagulation” is a multifaceted process. At 43°C - 50°C , bonds break within cell membranes, causing ruptures and some cell death [79, 80]. This process is usually termed *hyperthermia*. Around 50°C , enzyme activity decreases, cells become immobile, and various cell repair mechanisms are disabled, leading to increased cell death. When temperatures exceed 60°C , proteins become denatured. Thermal denaturation is a structural and functional change in a protein due to the heating it undergoes. This means they change from a highly organised structure with specific purposes, to disorganised structures with little to no function at all [81].

The next stage in the tissue damage process is the vaporisation of water. As the temperature of the tissue starts to approach 100°C (at 1 atm), water starts to vaporise. If the vaporised water cannot escape the tissue it forms steam vacuoles, small pockets of steam. These vacuoles can easily been seen when viewing tissue samples after tissue has been treated with a high powered laser (see Fig. 3.7). In certain conditions these steam pockets can explode [82].

The third stage of tissue damage is carbonisation of the tissue. This occurs when most of the water has boiled off, leaving the remaining tissue to heat up and reduce to its elemental carbon form. This carbonisation of tissue, when it occurs, is generally only a thin layer of 5-20 μm [79, 83].

The final stage of tissue damage is the removal of the remaining tissue, i.e. tissue ablation. There is no agreement in the literature how tissue undergoes ablation with several methods proposed. The three main methods are: photochemical, thermal, and explosive [84–86]. Photochemical ablation is when the energy of a photon from the irradiating laser, is sufficient enough that it excites the electronic state of the tissues molecules into an anti-boding state, leading to broken bonds and conversion from electronic energy into kinetic energy, and thus ablation. Thermal ablation is where tissue is heated sufficiently so that tissue vaporisation takes place. Finally, explosive ablation is an extreme version of thermal ablation. Explosive ablation occurs when large amounts of energy is deposited in a small time scale, so that none of the energy can thermally diffuse away, resulting in explosive ablation. Photochemical ablation, is usually applied to UV laser ablation, whereas thermal and explosive ablation regimes are the more likely candidates for IR ablation which is considered here.

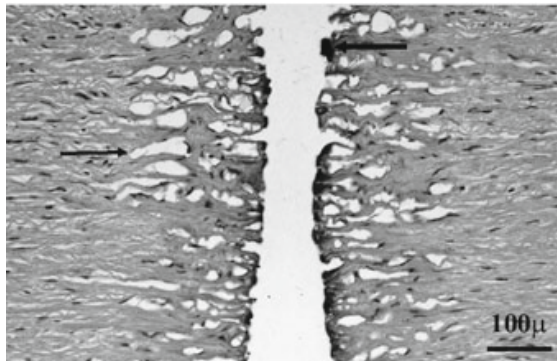


Figure 3.7: Ablation of a dog aorta, as viewed under a microscope. Steam vacuoles are clearly visible either side of the ablation area. Carbonisation is also evident at the edges of the ablation fronts. Adapted from [79].

The theoretical models behind explosive and thermal ablation models are also not well understood, with many models proposed to try to explain experimental results. These models range from heuristic models to sophisticated models that relate the underlying physical mechanisms to ablation damage. The two main heuristic models are: the blow off model, and the steady state model. The blow off model assumes that there is thermal confinement (i.e no propagation of heat in time t), and that material is removed after the laser irradiation. There is a radiant threshold that has to be met to ablate material, and that Beer-Lambert's law describes the spatial distribution of light. For laser pulses of < 10 ns, these conditions are normally met. However, for lasers with pulse length larger than this, these conditions are not usually met [87–89].

The steady state heuristic model, assumes that the pulse length is of the order of ms or larger, that material starts to be removed shortly after laser irradiation begins, and that some radiant threshold exists in order for ablation to begin. The steady state model also assumes that a fixed energy is required to remove a unit of tissue [87]. However, this does not always hold, as there are many circumstances where there is no one fixed energy, but rather many energies (due to various phase changes) that must be met in order for ablation to occur. There are also many other sophisticated models, that try to describe what happens physically when ablation occurs [90–92].

Due to the above mentioned reasons, there is no defined ablation temperature. The literature however, does suggest that it takes place when the tissue temperature is between 177 °C and 500 °C [91, 93, 94].

To model all these tissue damage processes the tissue damage model is split into two sections: coagulation damage and “physical” damage. Coagulation damage has no effect on the tissue’s bulk optical or thermal properties. “Physical” damage changes the tissue optical and thermal properties.

Modelling coagulation damage

With the description of the various processes that tissue undergoes during ablation, a numerical model of these processes can be created. First to model the full extent of the damage done under 100°C, i.e in the coagulation regime, the Arrhenius damage model is used. The Arrhenius damage model was originally used as a kinetic model of reaction products in chemistry [95]. It has since been adapted by various authors for modelling tissue damage, and is the *de facto* standard [96, 97]. These authors and various others, adapted this model by fitting Eq. (3.18) to

experimental data for burn damage. The two parameters fitted are A, the frequency factor, and ΔE , the activation energy.

$$\Omega(t) = \int_{t_i}^{t_f} Ae^{-\frac{\Delta E}{RT}} d\tau \quad (3.18)$$

Where:

- Ω is the damage value [-];
- A is “frequency factor” [s^{-1}];
- ΔE is activation energy [$Jmol^{-1}$];
- R is the universal gas constant [$Jmol^{-1}K^{-1}$];
- T is the temperature [K];
- and t_i and t_f are the initial time and final time at t_{crit} .

It is reported that a value of Ω of 0.53, 1.0, and 10^4 relate to first, second, and third degree burns respectively [98]. The Arrhenius damage model is used to better understand the amount of damage caused by the laser in the non-ablated areas of tissue. Values of $A = 3.1 \times 10^{98}$ and $\Delta E = 6.3 \times 10^5$ are adopted [94, 96, 99].

Modelling physical tissue damage

As tissue mostly consists of water [100] when the temperature of the tissue approaches $100^\circ C$ (at 1 atm), water in the tissue begins to boil off. This acts as a large heat sink for the absorbed laser energy, slowing down the rate of ablation. The energy required to boil the water is $Q_{vapor} = m_v \cdot L_v$, where m_v is the mass of a voxel, and L_v is the latent heat of vaporisation. The energy to boil off the water is provided via the laser and heat diffusing into the voxel:

$$Q_{vapor} = \underbrace{laserOn(t) \cdot \dot{q} \cdot \Delta t \cdot V_{i,j,k}}_{\text{laser heating}} + \underbrace{c \cdot M_{i,j,k} \cdot \Delta T}_{\text{heat diffusion}} \quad (3.19)$$

Where:

- Q_{vapor} is the current energy in Joules that has been used to boil off the water in the voxel [J];
- $laserOn$ is a boolean variable that determine if the laser is on or off [-];
- \dot{q} is the energy absorbed by the voxel due to the laser [Wm^{-3}];
- Δt is the timestep [s];
- $V_{i,j,k}$ is the volume of the voxel labelled i, j, k [m^3];
- c is the heat capacity of the voxel [JK^{-1}];
- $M_{i,j,k}$ is the mass of the voxel labelled i, j, k [kg];
- and ΔT is the change in temperature the voxel would undergo, if the water was not boiling off.

As water boils off, the water content of each voxel changes. This affects the absorption coefficient, density, thermal conductivity, and heat capacity. Each of these vary with water content per voxel [101];

$$W = W_{init} - \left(W_{init} \cdot \left(\frac{Q_{current}}{Q_{vaporisation}} \right) \right) \quad (3.20)$$

$$\rho = \frac{1000}{W + 0.649 \cdot P} \quad (3.21)$$

$$c_p = 4.2 \cdot 10^3 \cdot W + 1.09 \cdot 10^3 \cdot P \quad (3.22)$$

$$\kappa = \rho \cdot (6.28 \cdot 10^{-4} \cdot W + 1.17 \cdot 10^{-4} \cdot P) \quad (3.23)$$

$$\mu_a = W \cdot \mu_{water} + \mu_{protein} \quad (3.24)$$

$$(3.25)$$

Where:

W is the water content (i.e $W = 0.7$ equates to 70% water content);

W_{init} is the initial water content;

$Q_{current}$ is the total energy absorbed by the i^{th} voxel since the temperature reached 100°C [J];

P is the protein content (i.e $P = 1.0 - W$);

κ is the Thermal conductivity [$\text{Wm}^{-1}\text{K}^{-1}$];

c_p is the heat capacity [$\text{Jkg}^{-1}\text{K}^{-1}$];

and μ_a is the total absorption coefficient, and μ_{water} and $\mu_{protein}$ are the absorption coefficients of water and protein respectively.

T_a is defined as occurring between 177 and 500 $^\circ\text{C}$ [91, 93, 94]. At T_a the tissue is removed and the thermal, optical, and physical properties set to that of air.

The updated damaged tissue structure is then fed back to the MCRT model and the whole process repeats until the predefined time limit is reached. This whole process of photon propagation, heat diffusion and tissue damage is outlined in Fig. 3.1.

3.2.4 Validation

Heat transport validation

To thoroughly validate the numerical method employed to solve the heat equation, the numerical method is compared against an easily solvable analytical case. The heat equation is solved on a cube, side L , in a surrounding medium of 0°C . The cube is initially at temperature 20°C and the temperature is calculated at various times. Thus, the boundary conditions are:

$$T(0, y, z, t) = T(x, 0, z, t) = T(x, y, 0, t) = 0^\circ\text{C} \quad (3.26)$$

$$T(L, y, z, t) = T(x, L, z, t) = T(x, y, L, t) = 0^\circ\text{C} \quad (3.27)$$

The thermal diffusivity (α), density (ρ), and heat capacity (c_p) are all set to 1. This corresponds to a material which has the thermal diffusivity between copper and aluminium [102, 103]. Assuming a separable solution in Cartesian coordinates yields:

$$\begin{aligned} T(x, y, z, t) = & (A_1 \cos(\alpha x) + A_1 \sin(\alpha x)) \cdot \\ & (B_1 \cos(\beta y) + B_1 \sin(\beta y)) \cdot \\ & (C_1 \cos(\gamma z) + C_1 \sin(\gamma z)) \cdot e^{-\alpha \mu^2 t} \end{aligned} \quad (3.28)$$

$$\mu^2 = \alpha^2 + \beta^2 + \gamma^2 \quad (3.29)$$

Applying the boundary conditions (Eqs. (3.26) and (3.27)) gives:

$$A_1 = B_1 = C_1 = 0 \text{ and } \alpha = \frac{\pi n}{L} \quad \beta = \frac{\pi m}{L} \quad \gamma = \frac{\pi p}{L} \quad (3.30)$$

$$\therefore T_{nmp}(x, y, z, t) = A_{nmp} \cdot \sin\left(\frac{\pi n x}{L}\right) \cdot \sin\left(\frac{\pi m y}{L}\right) \cdot \sin\left(\frac{\pi p z}{L}\right) \quad (3.31)$$

This yields the following solution for the heat equation using the principle of superposition, and solving Eq. (3.32) with $f(x, y, z)$ as the initial temperature profile of the cube:

$$A_{nmp} = \frac{8}{L^3} \int_0^L \int_0^L \int_0^L f(x, y, z) \cdot \sin\left(\frac{\pi n x}{L}\right) \cdot \sin\left(\frac{\pi m y}{L}\right) \cdot \sin\left(\frac{\pi p z}{L}\right) dx \cdot dy \cdot dz \quad (3.32)$$

$$T(x, y, z, t) = \sum_{n=1,3,\dots}^{\infty} \sum_{m=1,3,\dots}^{\infty} \sum_{p=1,3,\dots}^{\infty} \frac{2368}{\pi^3 nmp} \cdot \sin\left(\frac{\pi n x}{L}\right) \cdot \sin\left(\frac{\pi m y}{L}\right) \cdot \sin\left(\frac{\pi p z}{L}\right) \cdot e^{(-\lambda^2 t)} \quad (3.33)$$

Where:

$$\lambda^2 = \alpha\pi^2\left(\frac{n^2}{L^2} + \frac{m^2}{L^2} + \frac{p^2}{L^2}\right);$$

n, m, p are odd integers;

and L is the length of the cube.

A slice through the middle of the cube, $L = 50 \text{ cm}$, yields Fig. 3.8, which shows that the numerical method matches the analytical solution closely.

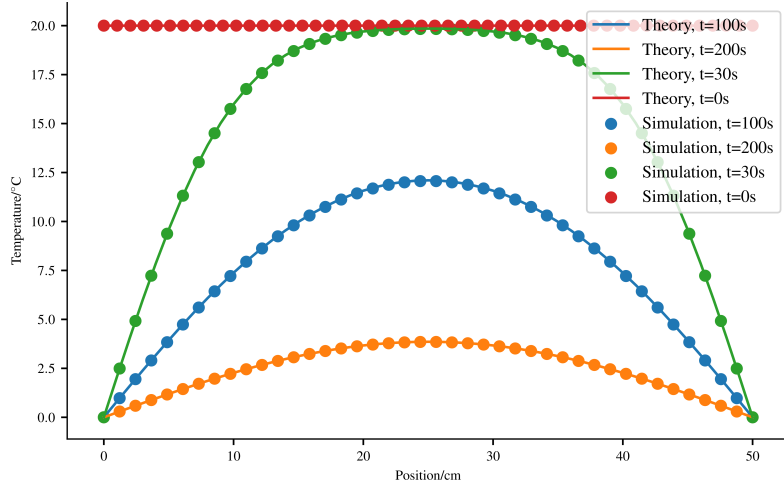


Figure 3.8: Temperature of the cube for various times, comparing between analytical solution and numerical method.

MCRT and heat transport validation

As a first test of the code, both MCRT and heat simulation, is compared to a simple analytical model of ablation. The simple model of ablation is as: the ablation energy (E_a), is defined as the minimum energy required to raise the temperature of the medium to 100 °C, and then boil off

the water in a volume dV , mass M . Thus, in one dimension Eq. (3.34), where the symbols have their usual meanings. If the energy for ablation is delivered in a time dt by a laser of intensity ($W\text{cm}^{-2}$), P , this gives Eq. (3.35). Equation (3.35) can be rearranged to give an ablation front velocity, Eq. (3.36).

$$E_a = c_p \rho dx \Delta T + L_v \rho dx \quad (3.34)$$

$$P \cdot dt = \rho dx (c_p \Delta T + L_v) \quad (3.35)$$

$$u = \frac{P}{\rho (c_p \Delta T + L_v)} \quad (3.36)$$

Assuming the ablation front moves with constant velocity during the ablation, and using $L_v = 2.53 \cdot 10^6 \text{ Jkg}^{-1}$, $c_p = 4181 \text{ J} \cdot \text{kg}^{-1} \cdot \text{K}^{-1}$ and the medium is a cube side 2 mm, with a starting temperature is 37 °C with a water content of 70% giving a density of 700 $\text{kg} \cdot \text{m}^{-3}$. For these parameters this gives an ablation velocity, $u \simeq 0.77 \text{ cm} \cdot \text{s}^{-1}$, and a time to ablate through 2 mm of tissue of $\simeq 0.26 \text{ s}$. As the code developed in this chapter simulates the diffusion of heat in a medium due to an incident laser, the expected time to ablate through the same medium should be slightly larger as heat diffuses away from the voxel while it is being heated. When the full heat + MCRT code is used to simulate this experiment, it gives a time, $t \simeq 0.33 \text{ s}$.

3.3 *In silico* results

3.3.1 Introduction

To match the experimental results, an accurate model of the experimental setup *in silico* must be created. However, due to computational constraints, such as memory and time available, some approximations to the experimental set-up have to be made. The porcine skin was a large thin slice of the top most layers of the skin. However, as the area of interest is where the ablation occurs, initially the porcine skin is modelled as a cuboid, dimensions: $1.1 \times 1.1 \times 0.5 \text{ cm}$. The initial temperature of the porcine skin is assumed to be around 5°, as the tissue was kept on ice or was kept cooled. As mentioned in the previous sections, there are several unknowns in the model: T_a , water content, temperature of air after ablation, and the exact thermal and optical properties of the porcine tissue. Therefore several models are run so that the full parameter space of these unknowns can be explored. Results from these *in silico* experiments are presented in this section along with a comparison of the model to the experimental work carried out in collaboration with the University of Dundee and the Photobiology department at Ninewells Hospital.

Optical & thermal properties

The thermal and optical properties of porcine tissue are not known exactly for any given tissue sample. As such the thermal and optical properties used in this section are taken from various literature sources.

The laser used in the experimental work is an CO₂ laser operating at 10.6 μm . This means that the optical properties of the tissue are dominated by water absorption. The laser used in the experiment is the Pixel CO₂ [104]. The Pixel CO₂ laser has a wavelength 10.6 μm which corresponds to an absorption of coefficient in water of $\sim 850 \text{ cm}^{-1}$. As the absorption coefficient is large, it is assumed that scattering is negligible at these wavelengths. Table 3.1 summarises the thermal properties for tissue and air used in the simulations.

	Thermal conductivity, κ	Density, ρ	Heat capacity, c
Tissue	$\rho \cdot (6.28 \cdot 10^{-4} \cdot W + 1.17 \cdot 10^{-4} \cdot P)$	$\frac{1000}{W+0.649 \cdot P}$	$4.2 \cdot 10^3 \cdot W + 1.09 \cdot 10^3 \cdot P$
Air	$a e^{-b(T-273.15)} + c$	$\frac{p_{atm}}{R_{spec}T}$	1006

Table 3.1: Optical and thermal properties for porcine tissue and air. W and P are the percentage of water and protein respectively. ρ is the density of the skin, p_{atm} is the pressure of air at 1 atmosphere, and R_{spec} is the gas constant. a , b , and c are constants.

The laser was used in “Pixel beam” mode. This means that the laser beam is split into an array of smaller beams. The laser used an array 9×9 of 81 pixel beams, each with a diameter of $250 \mu\text{m}$. The Pixel CO₂ rated laser power is $\sim 70 \text{ W}$.

The laser delivered one single pulse of varying total energy delivered over the range 50 mJ to 400 mJ , in so called “super pulsed mode”. The experiment consisted of ablating the porcine tissue, as a function of energy per “pixel” beam. This was achieved by adjusting the pulse length of the laser, τ , so that the energy per pulse was varied over a range 50 mJ to 400 mJ .

Computational speed up:

As discussed in the Section 3.1, the volume of interest is the area around the ablation craters. The volume is $1.1 \text{ cm} \times 1.1 \text{ cm} \times 0.5 \text{ cm}$. However, for the simulation to have good resolution of the ablation craters this volume would require many voxels for the tissue model. This is unfeasible due to: the memory required to store the various counters, grids, and variables, and the time that would be required to carry out the computation. Thus, the volume of interest is reduced to focus on just one of the ablation craters that is created by the laser (a volume of $0.06 \text{ cm} \times 0.06 \text{ cm} \times 0.18 \text{ cm}$) As a check to ensure that no physical phenomena are omitted by focusing on just one ablation crater, an initial simulation that models the full volume of interest was carried out to investigate the possibility of overlapping craters or other related phenomena. The simulation, as shown in Fig. 3.9, gives reassurance that the shrinking of the volume of interest is a valid approximation to make as there is no overlap between the separate ablation crater.

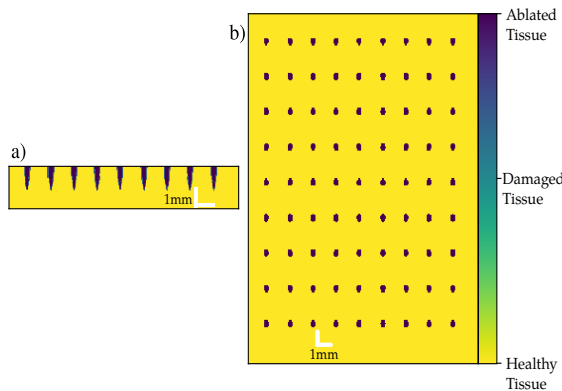


Figure 3.9: Simulation of 81 pixel beams. Figure a) shows a slice through the optical properties at the end of the simulation in the z - y plane. Figure b) shows the optical properties in the x - y plane at the top surface. Yellow is unchanged tissue, and purple is completely ablated tissue. Figure shows that the ablation craters do not overlap one another.

3.3.2 Results

Investigating ablation temperature, T_a

Various literature sources report the ablation temperature ranging widely from 177° to 500° [91, 93, 94]. Thus, several models are run over this range to establish the T_a which fits the experimental results. Figures 3.10 and 3.11 show how T_a , and beam profile affect the crater depth as a function of pixel beam energy for the CO₂ laser. The data suggests that, a T_a around $T_a = 500^\circ C$ is appropriate for the studies carried out, the upper limit of T_a from the literature.

Increasing the ablation temperature has the obvious effect of requiring more energy to be deposited by the laser before ablation takes place. This also allows more heat to diffuse away from the ablation crater increasing the thermal damage done to the surrounding tissue. Decreasing the ablation temperature has the converse affect, and allows the ablation crater to become deeper.

Over the full range of T_a , as the energy per pixel beam increases, there is a trend that at higher energies the crater depth begins to taper off. This is potentially due to several reasons. As the ablation craters grows the volume of tissue that is ablated is replaced with air, allowing more heat loss from the tissue to the environment. As well as heat loss to the environment, more heat is diffused away into the surrounding tissue as the crater grow, due to the availability of more tissue for the heat to diffuse into.

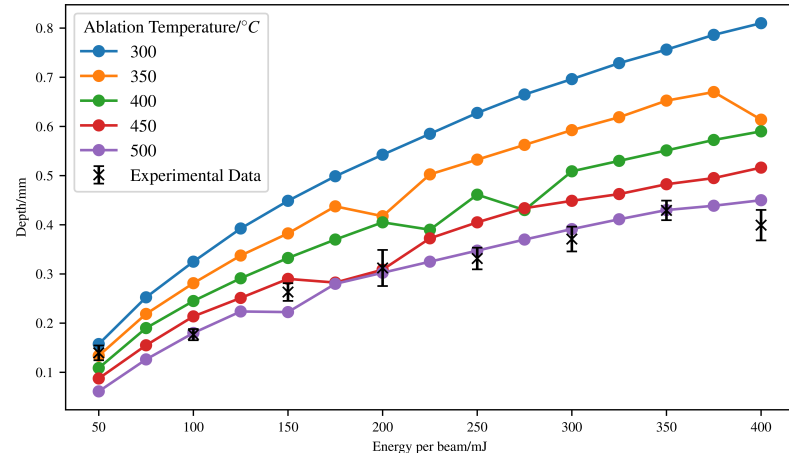


Figure 3.10: Simulation of 70 W CO₂ ablative laser, with a circular beam profile. Crater depths as a function of pixel beam energy for various T_a 's.

Investigating beam type

As the manufacturer does not provide information on the beam profile of the pixel beams and the lack of equipment available to measure the beam profile, the shape of the beam profile has to be assumed. Two different beam types are tried: Gaussian and circular (top-hat). Figures 3.10 and 3.11 show the result of these *in-silico* experiments. The Gaussian beam ablates deeper holes than the circular beam type, which is to be expected due to the distribution of power in the Gaussian beam. The beam that best fits the data is the circular beam. For the Gaussian beam to fit the data ablation would have to take place at temperatures above $500^\circ C$ which does not fit with the literature. Without knowing the exact profile of the beam, it is assumed for the rest of the *in-silico* experiments that the beam profile is circular.

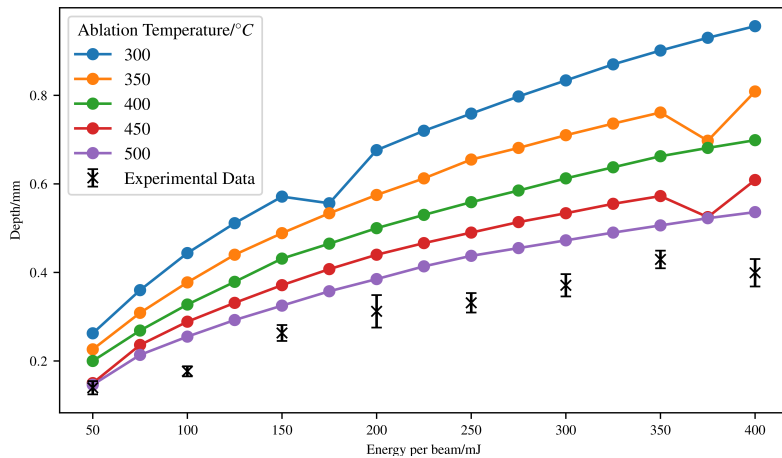


Figure 3.11: Simulation of 70 W CO₂ ablative laser, with a Gaussian beam profile. Crater depths as a function of pixel beam energy for various T_a 's.

Temperature during ablation

Figure 3.12 shows slices of temperature as a function of time during a simulation for $T_a = 500$ °C. This means that every column of pixels shows a bore hole through the medium (along the z axis) for a given time. Figure 3.12 also shows the laser pulse profile as a function of time as a reference so that knowledge of when the laser is on or off is easily elucidated. The figure shows that the temperature reaches a maximum temperature which is equal to T_a , regardless of ablation progress. This maximum temperature is researched roughly 0.25 s into the simulation, and lasts until ~ 0.75 s. The maximum temperature The ablation crater depth can be seen by the evidence of the “dark valley” before the jump in temperature. The border of the crater region is slightly cooler, with a maximum slightly deeper into the tissue. This temperature maximum extends for a small distance into the tissue, before diffusion spreads it out.

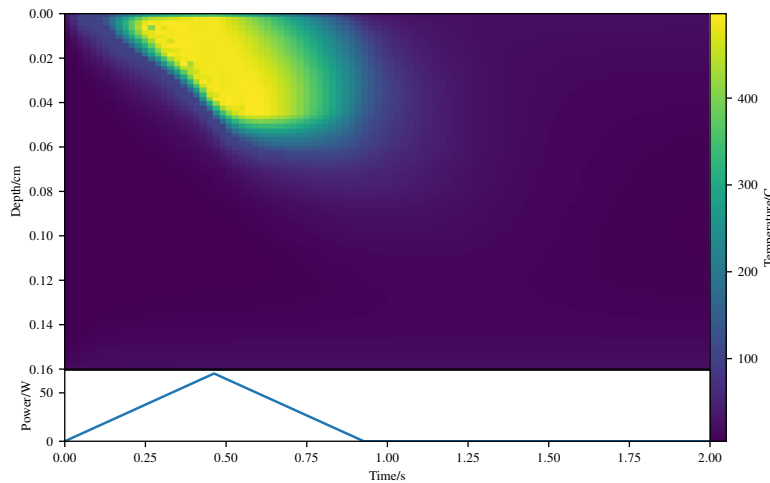


Figure 3.12: Temperature bore hole though centre of medium as a function of time, for $T_a=500$ °C.

Once the laser reaches maximum power

Investigating thermal damage

As stated in Section 3.2.3, the Arrhenius damage integral is used to estimate the thermal damage due to the laser. To calculate the tissue damage around the ablation craters, Eq. (3.18) is first transformed into a summation:

$$\Omega(t) = \int_{t_p}^{t_f} Ae^{-\frac{\Delta E}{RT}} d\tau \quad (3.37)$$

$$\Omega(t) = \sum_{m=m_p}^{m_f} Ae^{-\frac{\Delta E}{RT_\xi^m}} \Delta t \quad (3.38)$$

Where:

ΔE , R , T , and A have the same meanings as before;

ξ is the i^{th} , j^{th} , k^{th} node;

and m_p is the p^{th} timestep when the ξ^{th} node is above the threshold temperature.

Using Eq. (3.38) it can thus be estimated that the damage to the tissue on a voxel by voxel basis. Figure 3.14 shows how far the thermal damage extends around the ablation crater. For ease of visualisation 1-3 is mapped to their respective burns via the following scheme, with η as burn severity:

$$\eta = \begin{cases} 3, & \Omega \geq 10000 \\ 2, & 1 \leq \Omega < 10000 \\ 1, & 0.53 \leq \Omega < 1 \\ 0, & 0.0 \leq \Omega < 0.53. \end{cases} \quad (3.39)$$

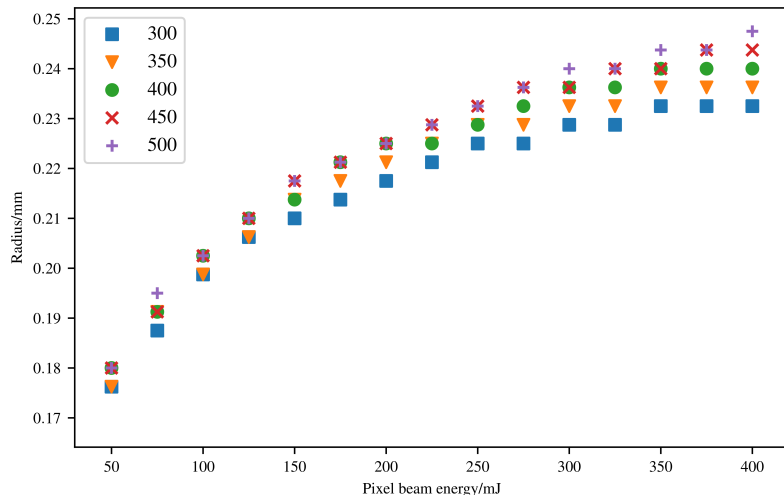


Figure 3.13: Figure shows the maximum horizontal extent of thermal damage as a function of energy per pixel beam, for different T_a 's.

As shown in Fig. 3.14, the thermal damage zone extends for a small distance around the ablation crater, due to the diffusion of heat into these areas. Figure 3.13 shows the maximum horizontal thermal damage distance as a function of T_a , and pixel beam energy. For values of T_a less than $\sim 425\text{ }^{\circ}\text{C}$, it appears that the maximum horizontal extent of the thermal damage tapers off. This is most likely because for lower values of T_a , there is a larger ablation crater, meaning that the energy from the laser is deposited deeper in the tissue in comparison to higher values of T_a . The higher values of T_a allow greater diffusion of the heat, thus yielding larger zones of damage. Overall there is little difference in the maximum horizontal extent of thermal injury, when using different energies (of the order of $\sim 0.01\text{ mm}$).

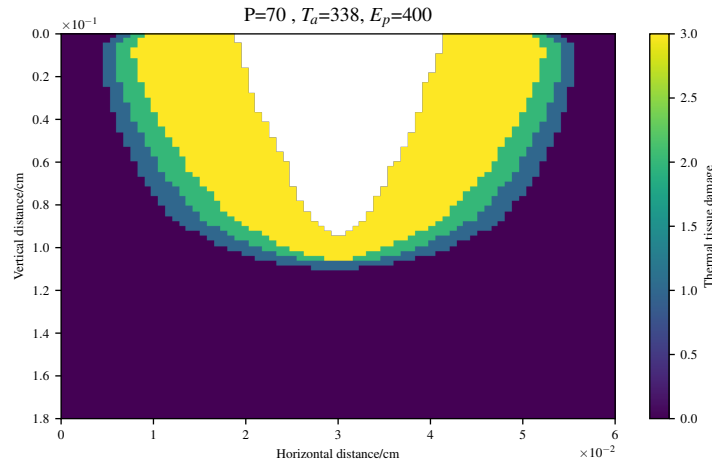


Figure 3.14: Tissue thermal damage around the ablation crater (white). Thermal tissue damage values of 3 refer to 3rd degree burns, 2 to 2nd, and 1 to 1st degree burns respectively. P is the power in Watts, T_a is the ablation temperature in Kelvin, and E_p is the energy per pixel beam in mJ.

Investigations for the time it takes for different areas of the tissue to become thermally damaged, were also carried out. This can be easily achieved by saving the time each voxel passes one of the damage boundaries in Eq. (3.39). Figures 3.15 and 3.16 show the minimum time taken for 1st, 2nd, and 3rd degree burns to occur as a function of depth. Figure 3.15 shows that there is little to no time (upon the order of 0.5 ms) between 1st and 2nd, and 3rd degree burns. Figure 3.16 shows there is a slightly greater time difference between 1st and 2nd, and 3rd degree burns, however this is almost as negligible as the 400 mJ case.

The reason that there is almost no time between 1st and 2nd, and 3rd degree burns, is most likely because there is little time for heat to diffuse, whilst the laser is still illuminating the medium. The laser pulses are on the order of seconds, and tissue is not thermally conductive. This leads to the results presented here.

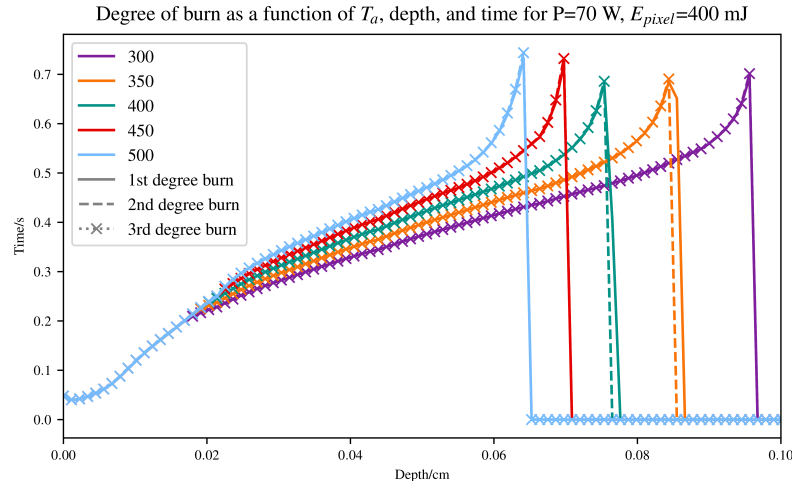


Figure 3.15: Figure show the time taken for 1st, 2nd, and 3rd to occur as a function of depth, for a range of T_a 's at 400 mJ.

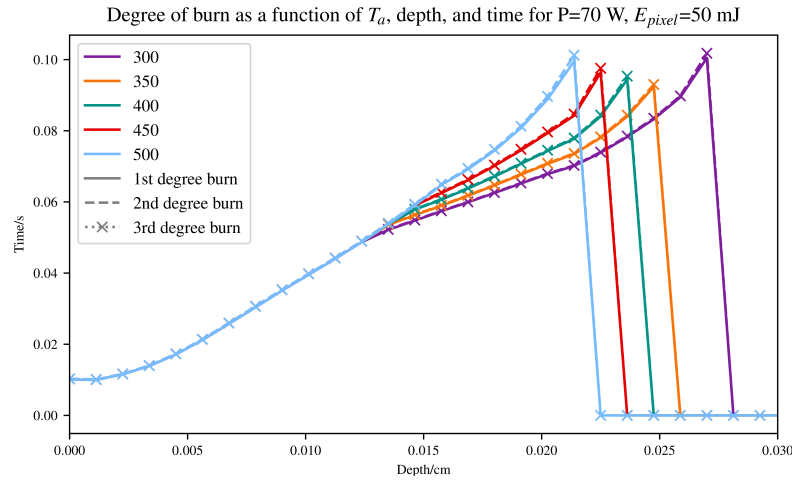


Figure 3.16: Figure show the time taken for 1st, 2nd, and 3rd to occur as a function of depth, for a range of T_a 's at 50 mJ.

Investigating laser pulse profile

Pulsed lasers have a variety of pulse profiles. The pulse profiles are usually modelled as triangular, tophat, or Gaussian. However, the pulse profiles in reality are normally less well defined, and rather the pulse profile is something in between these perfect models.

The laser used in the above experiments, the Pixel CO₂, uses a triangular pulse profile for the laser pulses. Thus, in this section the effect of the laser pulse profile has on ablation and the surrounding thermal injury is investigated.

Four different laser pulses profiles are investigated: tophat, triangular and two different Gaussian profiles. The two different Gaussian pulses trialled are, a Gaussian profile with σ equal to the pulselength, and a pulse profile where the same energy is expended.

Figure 3.17 show the pulse profiles for a pulselength of 0.2 s.

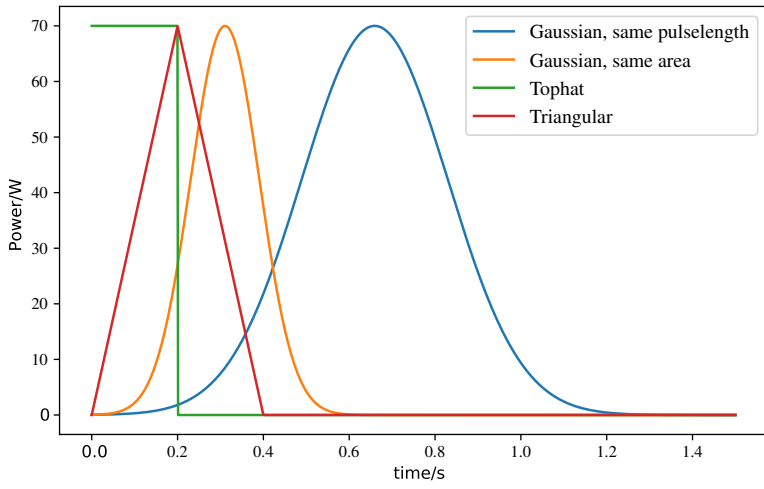


Figure 3.17: Comparison of the different pulse profiles trialled for a pulselength of 0.2 s.

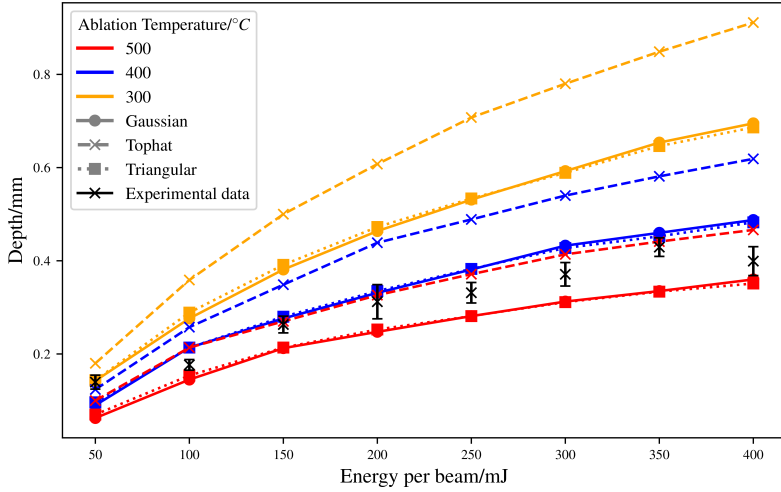


Figure 3.18: Comparison of various pulse shapes for the pixel beams.

Investigating Initial Temperature

As the experiment was carried out on porcine tissue that was kept on ice before the experiment was conducted, we assumed that the initial temperature of the porcine tissue was around 5 °C. This section investigates whether this is an accurate assumption.

To investigate this, three different temperatures were trialled: 0 °C, 5 °C, and 25 °C. These temperatures correspond to room temperature, the temperature of ice and the original temperature we assumed. Figure 3.19 shows the results of this *in-silico* investigation.

As expected the hotter the porcine skin is initially the larger the ablation depth. This occurs as less energy is required to bring the porcine skin to its ablation temperature. In the previous subsections it was assumed that the temperature of the porcine skin was around 5 °C. This assumption was based upon the fact that the porcine skin was kept on ice before the experiment, thus the temperature of the skin must be between 0 and room temperature. This investigation shows that over small variations of temperature ($\lesssim 5$ °C), the ablation depth does not vary too

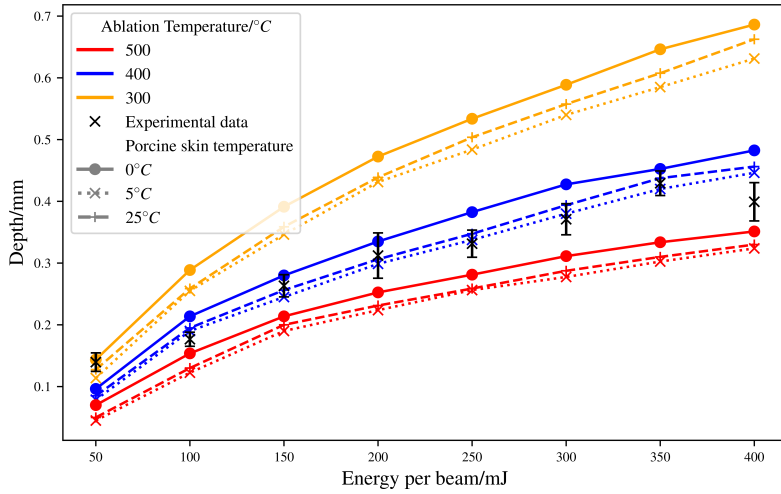


Figure 3.19: Comparison of ablation depths for different initial temperatures in the porcine skin.

much (on the order of $\approx 0.01 \text{ mm}$).

However, there is a greater difference in the maximum extent of thermal damage to the skin for different initial temperatures in the porcine skin. Figure 3.20 shows this difference.

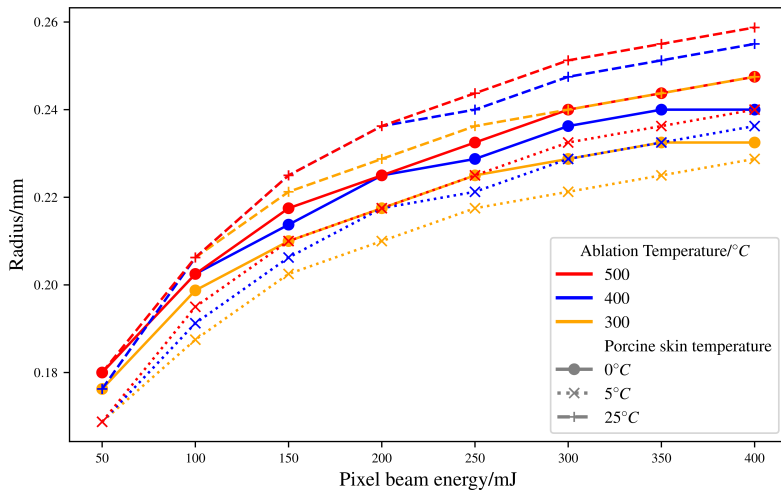


Figure 3.20: Comparison of maximum horizontal damage distance for different initial porcine skin temperatures.

Investigating Voxel Temperature After Ablation

In the previous section it is assumed that the temperature of a voxel remains unchanged after the tissue is removed from that voxel via ablation. However, this assumption may not be accurate. To test if the temperature of the voxel after ablation effects the depth of ablation or the thermal injury to the surrounding tissue various voxel temperature were tried. Two different temperatures

were tried: half the ablation temperature and room temperature($\approx 25^\circ C$). Figure 3.21 shows the effect of the voxel temperature after ablation has on the ablation depth.

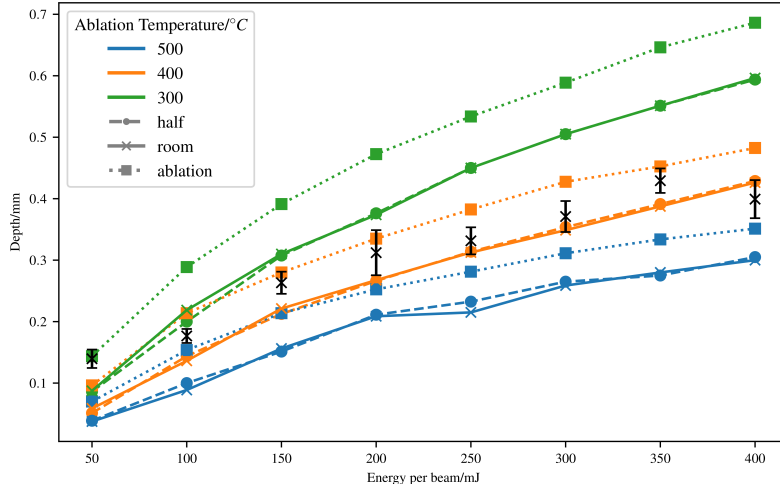


Figure 3.21: Comparison of different voxel temperatures after ablation. Half refers to setting the temperature of a voxel to half that of the ablation temperature. Room refers to room temperature, and ablation leaves the temperature at the ablation temperature.

Setting the voxel temperature to either half the ablation temperature or to room temperature has a large effect on the ablation depth, with a difference of $\approx 0.1\text{ mm}$. However, there is a small difference between setting the voxel temperature to room temperature and to half of the ablation temperature though.

3.4 Application of Model for Spy Disposal

In the 1964 James Bond film, Goldfinger, James Bond is threatened with a laser by the titular antagonist ()Fig. 3.22. Would this laser actually cut Bond in half as the film implies, and could Goldfinger be more humane[†] in his choice of laser for the task?

As the first laser was demonstrated in 1960 was a ruby laser of 694 nm , with the film being released in 1964 and the “laser”[‡] shown on screen being red, the likely laser portrayed is a ruby laser.

To assess whether Bond would die due to the laser we used the model outlined in this chapter with the following parameters.

As Auric Goldfinger uses this laser to cut sheets of gold, we assumed the power of the laser was around 1 kW , as industrial lasers used to cut metal, are high powered continuous operation lasers. We assumed that the Bond is completely made of skin, with no organs or bones. We ran two simulations, one for the Ruby 694 nm and one for the CO_2 $10.6\text{ }\mu m$. For the CO_2 as before there is no scattering due to high absorption coefficient. The Ruby laser’s wavelength is highly scattering, so we model both scattering and absorption. The medium we model is a 2 cm^3 cube of homogeneous skin.

We found that the CO_2 takes 22 ms , and Ruby takes 11 s to ablate through the 2 cm medium. From timing the movie, the laser moves at a round 1 cms^{-1} . Therefore the Ruby laser used

[†]i.e could Goldfinger use a laser that would lessen Bond’s suffering.

[‡]A laser was not used on set, but rather was added in post-production.

by Goldfinger would only give Bond some serious burns, but would leave him in one piece. If Goldfinger used a CO_2 laser then Bond would have been cleanly cut in two.



Figure 3.22: Still image of the iconic laser scene in the film Goldfinger. Copyrights Eon Productions.

3.5 Conclusion

Using MCRT and a finite difference method, a fully 3D model of photon and heat transport within tissue has been created. This model can be used to simulate the heat deposited by laser, the ablation craters formed via high powered lasers and the resultant thermal damage surrounding the ablation crater.

The model has been fully compared with both analytical solutions and experimental results. The model was found to match with experimental results that a tissue ablation temperature T_a of around $500\text{ }^{\circ}\text{C}$ has to be adopted, toward the higher end of the range previously observed in the literature.

The simulations allow us to predict for a given laser power and pulse length, how much thermal damage is caused in the tissue, and how deep an ablation crater that will form. The computational model could be used in future to help develop treatment regimes for both aesthetic and medical procedures. For example, currently there is considerable amount of “down time” after skin rejuvenation, in which the patient displays inflammation, erythema, edema, pain, and crusting [105–107]. Simulations of thermal damage due to fractional ablation could help design treatment regimes that minimise these effects, whilst still delivering skin rejuvenation. The model can also be applied to help optimise laser assisted drug delivery. Laser assisted drug delivery consists of using a laser to “drill” holes into the skin to help topical medicines diffuse into the skin better, than just applying the medicines to skin with no holes. Our model can help predict the laser parameters needed to reach a certain hole depth, thus minimising thermal damage and pain to patients.

There are many avenues available with regards to future work on this model. The model presented here in this chapter was on a initially homogeneous skin model. In reality skin is compromised of several distinctive layers, with each layer containing varying amounts of different chromophores. Our model can easily incorporate an multi-layered skin model complete with various fractions of chromophores. However, as the laser used in these studies is an infra-red laser, water is the highest absorbing chromophore, meaning that a physically accurate model, with various chromophores is not need for this application. The current model is a voxel based model, where all the voxels are the same size. This allows the model presented in this chapter to be

easily set-up, with regards to parallelisation, optical/thermal properties and ease of programming. However, voxel models, where all the voxels are the same size, are not computationally efficient. Particularly in order to achieve good resolution, many voxels are needed, which requires large amounts of RAM, due to a $\sim n^3$ scaling of voxels to memory in 3D. A more efficient way, would be to allow different sizes of voxels, depending on parts of the model which need high resolution, and parts that do not need high resolution. Such a voxel model is called an adaptive mesh refinement (AMR). There are downsides to AMR: complex implementation for parallelisation and set-up of optical/thermal properties, slower optical depth integration routines due to neighbour lookups.

Chapter 4

Quasi-wave/particle Monte Carlo Algorithm, φMC

4.1 Introduction

Complex shaped light beams have been used in a wide variety of applications in biophotonics and medicine. From using Airy beams to move particles and cells [108], Bessel beam “tractor beams” [109], Airy and Bessel beams for better field of view in light-sheet microscopy [110], and utilising Laguerre-Gaussian beams to optical trap optically reflective particles [111].

However, simulation techniques for modelling complex shaped beams in biological tissue is lacking. Currently there are several techniques that can model these beams in biological tissue, however they all have downsides. These methods include diffusion approximation to the RTE, finite difference time domain (FDTD), pseudo-spectral time-domain (PSTD), beam propagation methods (BPM), and MCRT.

As discussed in [Diffusion Approximation](#), the diffusion approximation has many issues when it comes to modelling light propagation in biological tissue. FDTD involves using a finite difference method to solve Maxwell’s equations. This is computationally intensive and requires a grid resolution of $\sim \lambda/20$ and thus most models are restricted to 2D [112, 113]. PSTD like the FDTD is also computationally intensive, though to a lesser extent [112]. Beam propagation method (BPM) is a fairly computational efficient method of propagating light beams, compared to FDTD or PSTD. However, the BPM uses the slowly varying envelope approximation, which limits some of the problems it can be applied. BPM is also generally a uni-directional propagation method, though it can be adapted to model bidirectional propagation, this can lead to issues in the model’s accuracy [112, 114].

The final method, MCRT, in general, cannot model complex beams where the wave-like behaviour of photons is required to form, or propagate the beam. For example, traditional MCRT methods cannot model Gaussian beams, as Gaussian beams have a finite beam waist at their focus (see Fig. 4.6). MCRT (along with geometric optics) predicts that Gaussian beams have an infinitely small waist.

Various authors have tried to model complex beams that require wavelike behaviours using MCRT. Some of the techniques used by these authors include: artificial beam steering [115], generating skew rays [116], complex ray tracing [117], decomposition [118], electric field Monte Carlo [119], and wavefront tracing [120]. However, all these techniques either inaccurately model Gaussian beams, can model Gaussian beams but are complex to implement or computational

intensive (more so than MCRT usually is). There have been some attempts at using the techniques presented in this chapter, to modify MCRT algorithms into algorithms that can model diffraction and interference [121–125]. These authors have good results, but either do not detail their methods, do not attempt to treat scattering or are in the x-ray regime.

This chapter modifies the MCRT method, from a “ballistic” photon method into a quasi-ballistic/wave photon method so that the wave behaviour of photons can be modelled. This algorithm, φMC , allows the modelling of complex shaped beams such as Bessel beams and Gaussian beams, without much modification of the underlying MCRT code.

We present a thorough investigation of the method used to turn a ballistic regime MCRT method in to a quasi-wave/ballistic method. The method is validated against theoretical and experimental data for various different beam types including: Bessel (including higher orders), and Gaussian beams. Treatment of the propagation through scattering media is also discussed.

4.2 Theory

To convert a MCRT simulation to be able to model wave-like behaviour of photons, we introduce two concepts: tracking the complex phase of packets and the Huygens-Fresnel principle. This section presents a description of the modifications to the traditional MCRT algorithm, alongside the theoretical background to both the concepts.

4.2.1 Complex Phase Tracking

The first concept we add to the MCRT method is assigning a complex phase to each packet. The phase is given to a packet at the beginning of the simulation depending on the input field. The packet is also given an initial electric field of the form:

$$E_0 = \frac{1}{N} \sqrt{\frac{P}{A}} \quad (4.1)$$

Where N is the number of packets run in a simulation, P is the power of the incident beam, and A is the area of the beam. This initial electric field is needed to compare different beams as in Section 4.6, and to normalise for number of packets run.

The phase is then tracked as the packet moves through the medium, over a distance l . Equation (4.2) shows how the phase is calculated.

$$\varphi = \cos\left(\frac{2\pi l}{\lambda}\right) + i \sin\left(\frac{2\pi l}{\lambda}\right) \quad (4.2)$$

Where φ is the complex phase of a photon packet, l [m] is the distance the packet has travelled, λ [m] is the wavelength of the packet. Now we can calculate the complex phase of a packet at a position P_o , if we know the distance it has travelled, and its original phase, see Fig. 4.1.

To model interference, we let the photon packets interfere with one another in a volume or area element. We do not model the interference at a point in space where photon packets cross, due to the ballistic nature of the MCRT simulation this does not occur with enough frequency to give a good signal to noise ratio. Therefore, interference takes place in a volume, dV , or area element, dA , instead. To calculate the intensity from the complex phase, the absolute value of the phase is squared. Therefore to calculate the intensity for a given voxel or area, the phase is first summed in each voxel or area before the absolute value is squared. Equation (4.3) shows the equation for intensity for a volume element dV . A similar relation for calculating the interference on an area element dA also exists.

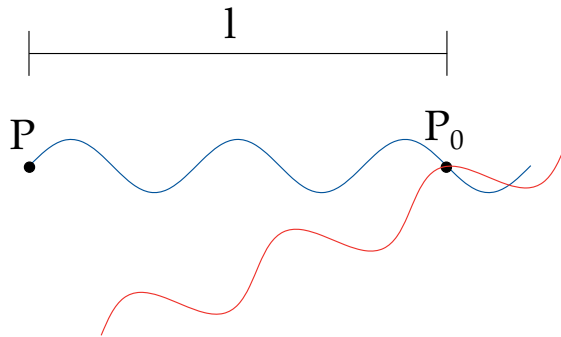


Figure 4.1: Example of phase calculation when a photon has travelled a distance l . The figure also shows an example of interference between two photons via addition of the complex amplitudes at the point P_0 .

$$I(\zeta) = \left| \sum_{\zeta} E_0 \cos\left(\frac{2\pi l}{\lambda}\right) + i \sum_{\zeta} E_0 \sin\left(\frac{2\pi l}{\lambda}\right) \right|^2, \quad \zeta = (x, y, z) \quad (4.3)$$

Where:

- l is the total distance travelled by a photon [m];
- λ is the wavelength of the photon [m];
- I is the intensity at the ζ^{th} cell [Wm^{-2}];
- E_0 is the initial electric field of the packets as in Eq. (4.1) [Vm^{-1}]
- and ζ is the x^{th} , y^{th} , z^{th} cell, volume dV .

In addition to tracking the phase, the next principle needed to simulate the wave behaviour of light in MCRT is the Huygens-Fresnel principle.

4.2.2 Huygens-Fresnel Principle

The Huygens-Fresnel principle is a method that is used to help model the propagation of waves in the far field limit and the near field limit. The Huygens principle was first postulated in 1678 and states [126–128]:

“Every point on a propagating wavefront serves as the source of spherical secondary wavelets, such as the source at some time later is the envelope of these wavelets.”

The principle is illustrated in Fig. 4.2. The principle allowed Huygens to derive laws of refraction and reflection, but it failed to describe diffraction effects. This led to Augustin-Jean Fresnel in 1818, combining the Huygens principle with his own theory of interference [128, 129]. This Huygens-Fresnel principle, gave an accurate description of the propagation of light and diffraction effects. This was achieved by allowing the secondary wavelets to self interfere, giving rise to an accurate description of the physical phenomena. Later, Gustav Kirchhoff gave a rigorous mathematical description of the Huygens-Fresnel principle, which is the basis of diffraction theory [130, 131].

The Huygens-Fresnel principle allows the modelling of diffraction in both the near and far field. As the principle states that every point on the wavefront is a source of secondary spherical waves, this implies that there are “backward” waves. These “backward” waves are un-physical, and there is no experimental evidence of their existence. Thus, Fresnel introduced an inclination

factor to eliminate these “backward” waves. This inclination factor was later put on a rigorous mathematical standing by Kirchoff, as it naturally fell out of his theory [130,131]. Equation (4.4), the Rayleigh-Sommerfeld diffraction integral of the first kind*, shows the equation for the complex field at a point on a plane.

$$u(\mathbf{r}_1) = \frac{1}{i\lambda} \int \int u(\mathbf{r}_0) \frac{\hat{s}_0 \cdot (\mathbf{r}_1 - \mathbf{r}_0)}{|\mathbf{r}_1 - \mathbf{r}_0|^2} e^{ik|\mathbf{r}_1 - \mathbf{r}_0|} dS_0 \quad (4.4)$$

Where:

- u is the complex electric field [Vm^{-1}];
- λ is the wavelength [m];
- S_0 is a plane with surface normal \hat{s}_0 [-];
- k is the wavenumber [m^{-1}];
- and \mathbf{r}_n are spatial coordinates [-].

The Huygens-Fresnel principle is implemented by sampling the light source on the surface of any lens or in a slit. In practise this means when for example, a plane wave is incident on a slit width a , and length b , the slit area is uniformly sampled for the initial position of the photon packets. The packets are then given a random direction, sampled toward the detector thus avoiding the non-existent “backward” waves. For the case of modelling propagation through a lens, the usual geometric optics approach is taken to propagate the packets through the lens. When the packet lies on the surface of the lens, the Huygens-Fresnel principle is invoked, and the packet is given a random direction (in the direction of the medium) and propagated as usual.

Our algorithm uses the Huygens-Fresnel principle and the tracking of complex phase to simulate diffraction effects, that would otherwise be absent from the simulation. The principle allows the algorithm to calculate the complex amplitude at a point, and thus the intensity at that point, essentially numerically simulating Eq. (4.4). These two concepts underpin the algorithm that allows various complex beams, and wave phenomena to be simulated within a ballistic method. The following sections validate the method against the theory and experimental data for propagation of various complex beams.

4.2.3 Validation of Phase Tracking Algorithm

Double Slit Experiment

The first test of our quasi-wave/particle MCRT algorithm[†], φMC , is to compare our simulation to a double slit experiment. The double slit experiment, is a simple experiment where a monochromatic plane wave of light is incident on two slits distance apart d , and width b , and an interference pattern is observed on a screen a distance L away from the slits. The experiment is usually carried out with the detector screen in the far field (the so called Fraunhofer regime). The intensity pattern on the detector screen is as in Eq. (4.5):

$$I(x) \propto \cos^2 \left(\frac{kdx}{2\sqrt{L^2 + x^2}} \right) \operatorname{sinc}^2 \left(\frac{kax}{\sqrt{L^2 + x^2}} \right) \quad (4.5)$$

Where the *sinc* function is defined as $\frac{\sin(x)}{x}$, for $x \neq 0$, k is the wavevector, $k = \frac{2\pi}{\lambda}$, and x is the horizontal position on the detector screen.

*If diffraction occurs in a plane, the Kirchoff diffraction integral can be modified to this

[†]Though this example is not strictly MCRT, but rather ray tracing, as it involves no scattering. The full MCRT method will be used in later sections.

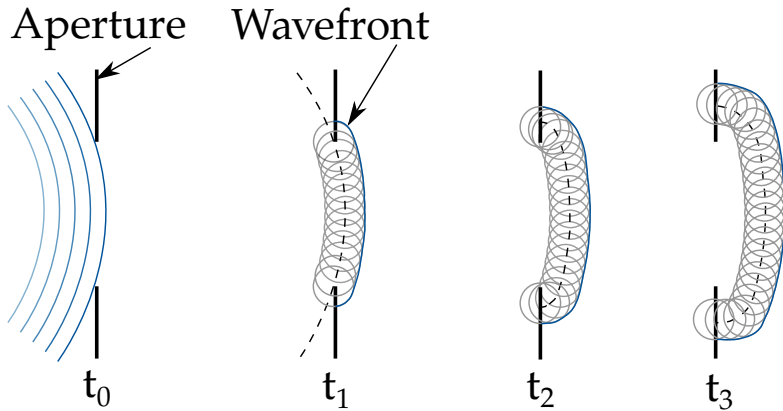


Figure 4.2: Illustration of the Huygens-Fresnel principle. At t_0 a wave is incident on an aperture. Times t_1 , t_2 , and t_3 show the evolution of the wavefront using the Huygens-Fresnel principle. Dashed lines illustrate the wavefront position at the previous time step, and is the source of the Huygens-Fresnel wavelets.

The simulation was carried out for a wavelength, λ , of 488 nm, a slit width of 10λ , slit separation of 80λ , and the detector screen positioned 10000λ away from the slits. Using the Huygens-Fresnel principle, each slit is a source of Huygens wavelets. The detector screen has dimensions, 1 mm^2 and there are 2051^2 bins, giving a bin an effective size: $\sim 488 \text{ nm}$ or $\sim \lambda$. The initial position of the photon packets is sampled uniformly from the slit area, after randomly choosing one of the slits to emit from. A random direction is then chosen to ensure that the packets will hit the detector screen. The simulation was run with 10^9 packets, which took $\approx 10 \text{ mins}$ to run on an 8 core Intel Xeon machine. This gave an accurate match to the theoretical expression, as seen in Fig. 4.3.

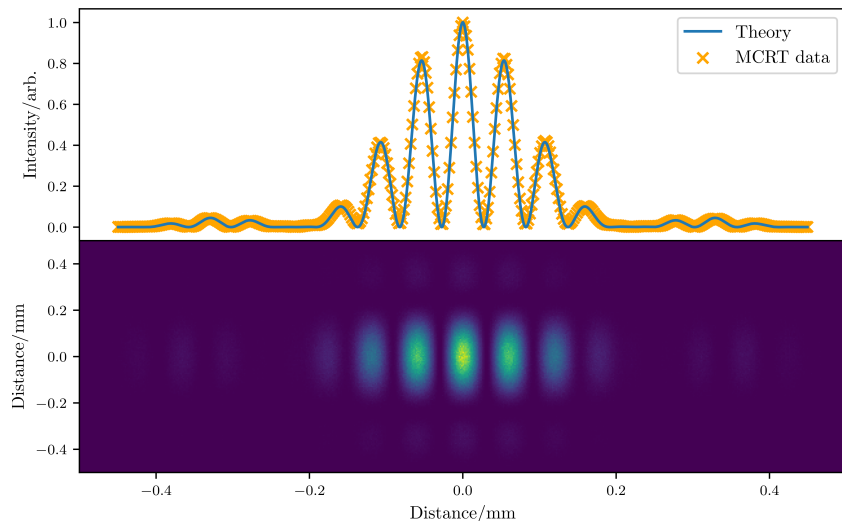


Figure 4.3: Comparison of theory and simulation for the double slit experiment. Top image shows a slice through the computed image and the expected profile from theory. For clarity only every 5th MCRT data point is plotted. Bottom image shows the computed image.

Diffraction by a Square Slit

φMC is also validated by simulating diffraction from a square aperture in the far and near field. Fresnel diffraction occurs in the near field when the *Fresnel number*, Eq. (4.6), is greater than 1.0. Fraunhofer diffraction occurs when the *Fresnel number* is less than 1.0.

$$F = l \sqrt{\frac{2}{\lambda r_0}} \quad (4.6)$$

Equation (4.6) is the Fresnel number, where l is the slit width, λ is the wavelength of the incident radiation, and r_0 is the distance from the aperture to the detector screen, as shown in Fig. 4.4.

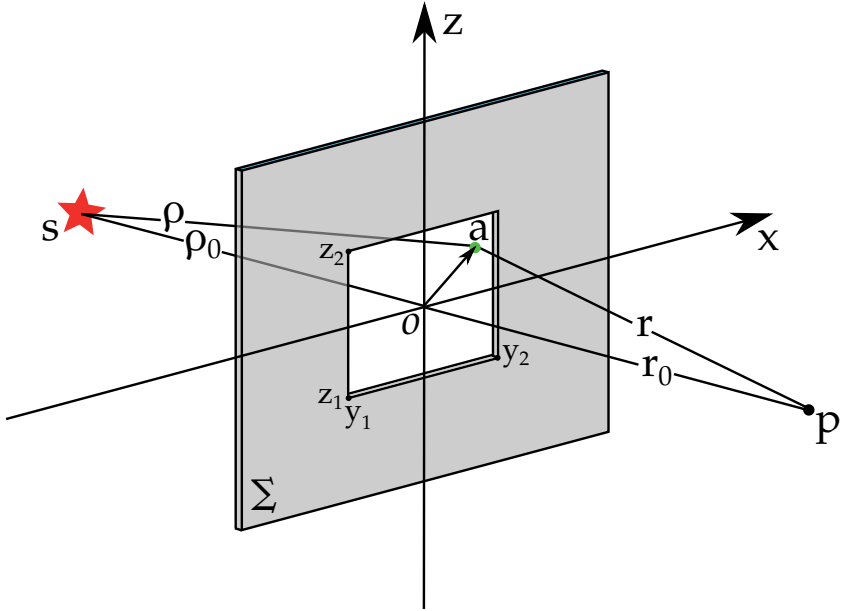


Figure 4.4: Geometry of the square aperture used in the validation.

To compare φMC to the theory, the theory must first be discussed. Consider the setup as shown in Fig. 4.4, to calculate the intensity at a point P the contribution by an area element dS at the point a , to the optical disturbance at a point P is considered. Accounting for the unobstructed optical disturbance from S as well and using Eq. (4.4), yields:

$$U(P) = \frac{1}{i\lambda} \iint_{\Sigma} \frac{A e^{i(k\rho - \omega t)}}{\rho} \frac{e^{ikr}}{r} \cos(\theta) dS \quad (4.7)$$

In the case where ρ_0 and r_0 are large compared to the size of the aperture, then $\cos(\theta) = 1$ and $\frac{1}{\rho r} = \frac{1}{\rho_0 r_0}$. The lengths of r_0 and ρ_0 are:

$$r = \sqrt{r_0^2 + y^2 + z^2} \quad (4.8)$$

$$\rho = \sqrt{\rho_0^2 + y^2 + z^2} \quad (4.9)$$

Using the binomial theorem to expand Eqs. (4.8) and (4.9) yields:

$$\rho + r \approx \rho_0 + r_0 + (y^2 + z^2) \frac{\rho_0 r_0}{2\rho_0 r_0} \quad (4.10)$$

Substituting Eq. (4.10) into Eq. (4.7) with $k = 2\pi/\lambda$

$$U(P) = \frac{Ae^{-i[k(\rho_0+r_0)\omega t]}}{i\lambda\rho_0 r_0} \iint_{\Sigma} e^{i2\pi y^2 \frac{(\rho_0+r_0)}{2\lambda\rho_0 r_0} + i2\pi z^2 e^{\frac{i\pi u^2}{2}} \frac{(\rho_0+r_0)}{2\lambda\rho_0 r_0}} dS \quad (4.11)$$

Introducing the dimensionless variables u and v

$$u = y \sqrt{\frac{2(\rho_0 + r_0)}{\lambda\rho_0 r_0}} \quad (4.12)$$

$$v = z \sqrt{\frac{2(\rho_0 + r_0)}{\lambda\rho_0 r_0}} \quad (4.13)$$

and substituting them into Eq. (4.11).

$$U(P) = \frac{\tilde{E}_u}{2} \int_{u_1}^{u_2} e^{\frac{i\pi u^2}{2}} du \int_{v_1}^{v_2} e^{\frac{i\pi v^2}{2}} dv \quad (4.14)$$

Equation (4.14) describes the optical disturbance at the point P , with \tilde{E}_u the unobstructed disturbance at P . Equation (4.14) can be evaluated using the Fresnel integrals, $C(w)$ and $S(w)$:

$$\int_0^w e^{i\pi w'^2/2} dw' = C(w) + iS(w) \quad (4.15)$$

$$S(w) = \int_0^w \sin\left(\frac{\pi w'^2}{2}\right) dw' \quad (4.16)$$

$$C(w) = \int_0^w \cos\left(\frac{\pi w'^2}{2}\right) dw' \quad (4.17)$$

Using Eq. (4.15), where $C(w)$ and $S(w)$ are the Fresnel integrals as in Eqs. (4.16) and (4.17). Equation (4.14) can then be transformed into an intensity, by taking the absolute value and squaring, yielding Eq. (4.18):

$$I_p = \frac{I_u}{4} \{ [C(u_2) - C(u_1)]^2 + [S(u_2) - S(u_1)]^2 \} \times \{ [C(v_2) - C(v_1)]^2 + [S(v_2) - S(v_1)]^2 \} \quad (4.18)$$

Equation (4.18) gives the intensity of the field at the point P on axis for a square aperture where I_u is the unobstructed intensity at the point P .

As the mathematics of calculating the optical disturbances at all points on a plane at point P is difficult, instead the aperture is moved by small displacements, with \overrightarrow{SOP} fixed. This effectively achieves the translation of the origin, O , with respect to the fixed aperture. Thus, for each displacement new aperture coordinates y_1 , y_2 , z_1 , and z_2 are generated and therefore new u_1 , u_2 , v_1 , and v_2 . Therefore the intensity at a point $P + \delta d$, where δd is the displacement,

can be calculated. This approximation holds for displacements that are small compared to the ρ_0 [127, 131, 132]. Using this method and Eq. (4.18) gives the theoretical curves in Fig. 4.5.

In φMC , the above experiment is simulated. A square slit is uniformly sampled in the x , and z direction to get the packets initial position. A random direction is then sampled, by uniformly picking a point on the detector screen. This ensures the algorithm does not waste time by calculating packets trajectories that are not registered by the detector. We assume a plane wave is incident on the aperture and each photon is given the same initial complex electric field.

The distance between the detector screen and the aperture is varied and the intensity on the screen is measured for $\sim 10^{10}$ photons released from the aperture as Huygens wavelets. For *Fresnel numbers* greater than 1.0, the number of bins is 300, covering a distance of $600 \mu m$. For the case of Fraunhofer diffraction, the number of bins is 100 covering a distance of $6000 \mu m$. The simulations take ~ 3 minutes for 10^{10} packets to be run on an Intel Xeon E3-1245 v5, 8 cores @ 3.5GHz machine. The number of bins, and photons packets simulated had to be increased for the cases where the Fresnel number was large (i.e the detector screen was near the aperture). This is due to the diffraction pattern becoming “noisy” and thus needs a higher resolution to accurately simulate. Fig. 4.5 shows the comparison between the theory and the φMC simulations.

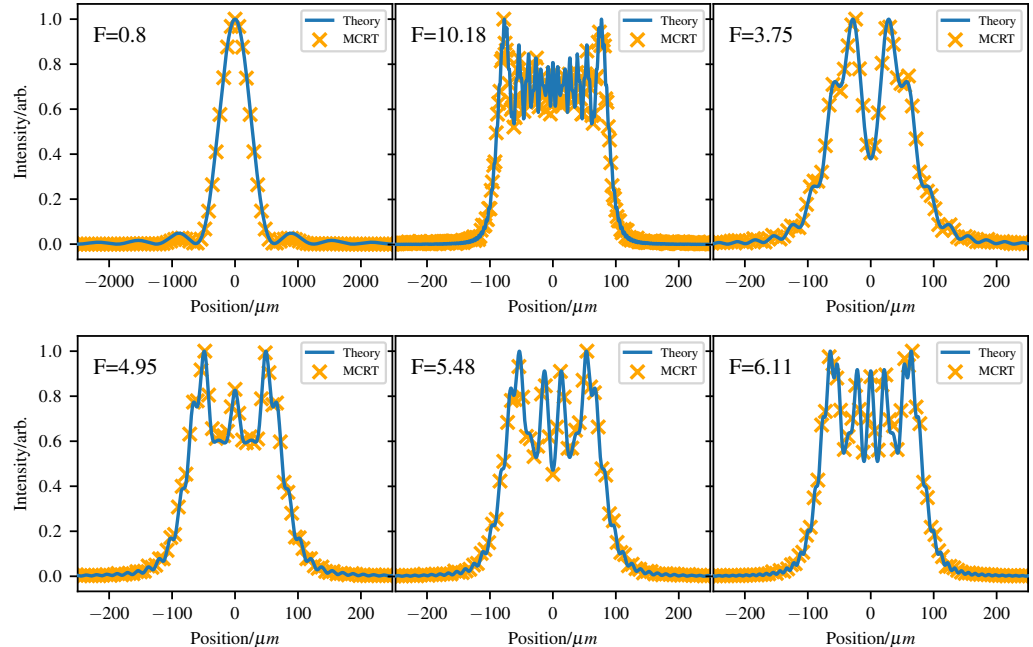


Figure 4.5: Comparison of theory and simulation for diffraction through a square aperture in the Fresnel and Fraunhofer regimes.

4.3 Gaussian Beams

Now that the method of tracking the complex phase of packets and using the Huygens-Fresnel principle has been verified against theoretical results, we can now turn our attention to modelling the propagation of beams that require the wave behaviour of light to either form or propagate. The first beam type we will examine is the Gaussian beam. Gaussian beams are important as most laser beams have the profile of the fundamental (TEM_{00}) Gaussian mode. This section will show that φMC can accurately model all the physical phenomena of Gaussian beams, within the MCRT regime.

Before discussing how φMC can model a Gaussian beam, the theory and various physical parameters of the beam must be described. The electric field of a Gaussian beam can be defined as in Eq. (4.19) [133]:

$$E(r, z) = E_0 \frac{w_0}{w(z)} e^{\frac{-r^2}{w(z)^2}} e^{-i(kz + k \frac{r^2}{2R(z)} - \varphi(z))} \quad (4.19)$$

Where:

r is the radial distance from the optical axis [m];

z is the axial distance from the beams waist [m];

k is the wavenumber, $k = \frac{2\pi}{\lambda}$ [m^{-1}];

E_0 is the electric field amplitude at the origin [$V m^{-1}$];

$w(z)$ is the radius of the beam at which the amplitude has fallen to $\frac{1}{e}$, at the distance z along the beam, Eq. (4.20) [m];

w_0 is the waist radius [m];

$R(z)$ is the radius of curvature of the beams wavefronts at z , Eq. (4.21) [m];

and finally, $\varphi(z)$ is the Gouy phase at z , Eq. (4.22) [-].

Equations (4.20) to (4.24) give the definitions of key physical properties as outlined above or as shown in Fig. 4.6. z_r is the Rayleigh range, Eq. (4.23), and defines the point at which the beams waist grows to $\sqrt{2}$ times the size of the beam at its waist. The waist of the beam at the focal point is defined as Eq. (4.24), where f is the focal length and D is the $\frac{1}{e^2}$ diameter of the beam at the lens.

$$w(z) = w_0 \sqrt{1 + \left(\frac{z}{z_r}\right)^2} \quad (4.20)$$

$$R(z) = z \left[1 + \left(\frac{z_r}{z} \right)^2 \right] \quad (4.21)$$

$$\varphi(z) = \arctan \left(\frac{z}{z_r} \right) \quad (4.22)$$

$$z_r = \frac{\pi w_0^2}{\lambda} \quad (4.23)$$

$$w_0 = \frac{2\lambda f}{\pi D} \quad (4.24)$$

$$(4.25)$$

With the physical properties of the Gaussian beam outlined, a Gaussian beam can now be modelled using our algorithm. To simulate a Gaussian beam, we set up the simulation as shown in Fig. 4.7. The simulated lens used is a convex-plano lens, with radius of curvature, 4.6 mm, thickness, L_t , of 2.2 mm, and working distance, W_d , 8.5 mm. A Gaussian beam wavelength

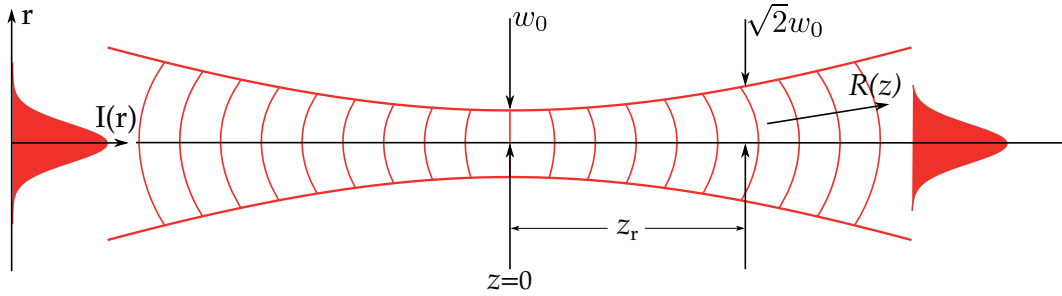


Figure 4.6: Illustration of a Gaussian beam focusing to its waist then diverging away. Image shows the various defined properties of a Gaussian beam along side the radius of curvature changing direction at the waist.

488 nm and $\frac{1}{e^2}$ waist diameter 0.5 mm, is incident on the lens. Using Eq. (4.24) yields the size of the focal spot as $3.1\mu\text{m}$.

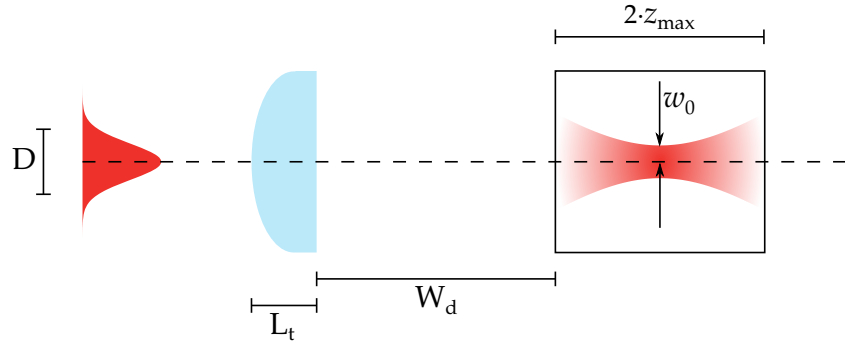


Figure 4.7: Simulation setup of focusing a Gaussian beam through a lens. Lens is convex-plano and is modelled on ThorLabs LA4249 UV fused silica lens [134]. L_t is the lens thickness, D is the $\frac{1}{e^2}$ input beam diameter, W_d is the working distance or back focal length, $2 \cdot z_{\max}$ is the depth of the medium, and w_0 is the beam waist.

To model the lens in φMC the photons initial z position is set just in front of the lens. The x and y are randomly sampled from a Gaussian distribution with a waist of $\sqrt{2}w_0$. The factor of $\sqrt{2}$ accounts for the conversion from intensity to electric field beam waist. This is because the electric field is $\propto \exp\left(\frac{-r^2}{4\sigma'^2}\right)$, and the intensity is $\propto \exp\left(\frac{-r^2}{2\sigma^2}\right)$. Thus, for the input electric field waist to be equal to the intensity, $\sigma' = \sqrt{2}\sigma$. The packet is given an electric field of the form Eq. (4.1), with $P = 1\text{ mW}$, and $A = \frac{1}{2}\pi w_0^2$.

The packet is then propagated to the surface of the convex side of the lens. This is achieved by finding the intersection of a sphere, which represents the convex side of the lens, and the packets path. With the packet on the surface of the lens, Fresnel coefficients are calculated to determine if the packet is reflected or refracted. If the packet is reflected the packet is killed and the process starts again. If the packet is refracted, and moved in the new direction to the planar surface of the lens. The new direction vector is calculated using a vector version of Snell's law (see Appendix A for discussion of this). The packets are then uniformly sampled onto the surface of the voxel medium and the usual MCRT method is used to propagate the packet whilst tracking the phase.

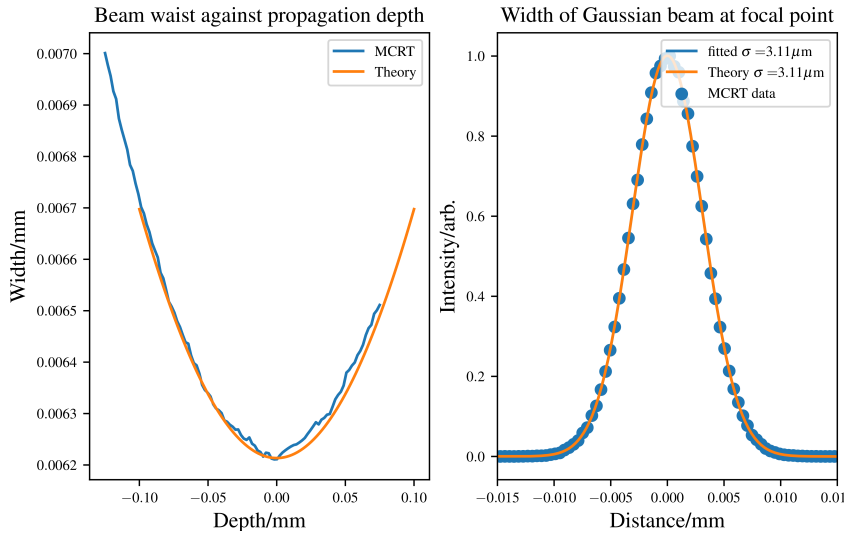


Figure 4.8: Results of *in-silico* experiment of focusing a Gaussian beam though a convex-plano lens.

Figure 4.8 shows the comparison of theory and *in-silico* experiment, with excellent agreement between the two.

φ_{MC} also correctly models the change of direction of the radius of curvature, $R(z)$, as is predicted by theory. This process is described by Eq. (4.21), before the waist the curvature is negative, at the waist it is infinite, and past the waist its is positive. This can be seen in Fig. 4.9, where the beam (direction of propagation right to left) undergoes this:

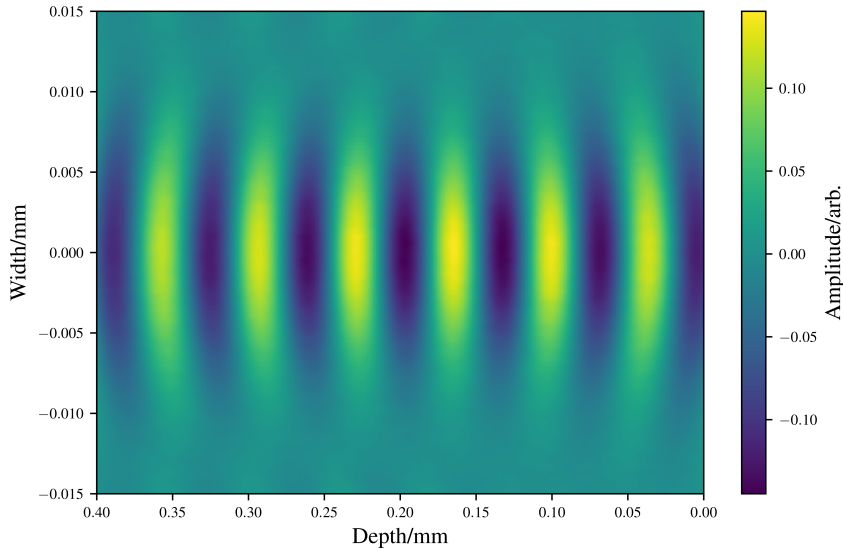


Figure 4.9: Slice through the real part of the complex electric field of the *in-silico* experiment as in Fig. 4.7. Figure shows the radius of curvature changing direction at the waist as predicted by theory.

φMC can also model spherical aberrations caused by lenses. Figure 4.10 shows aberrations caused by a plano-convex lens along side an illustration of the paths that light take through the imperfect lens, causing spherical aberrations.

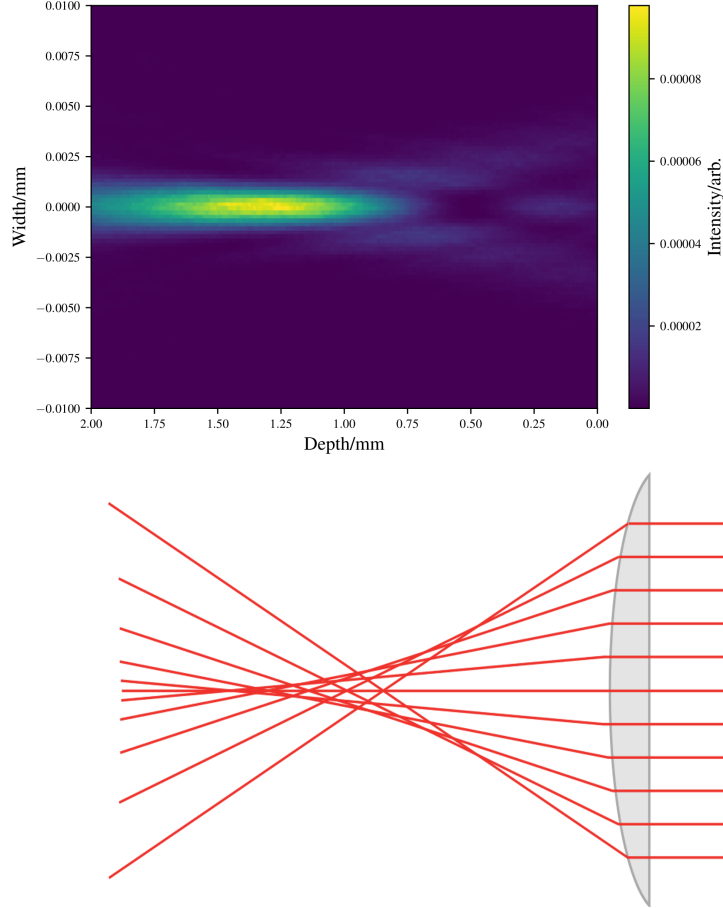


Figure 4.10: Illustration of φMC 's ability to model spherical aberrations. Top image generated using same setup as in Fig. 4.7, but with $D = 1.5$ mm within φMC . Image shows the elongated focus and characteristic interference pattern behind the focus. Bottom image shows illustration of rays traced through a lens which suffers from spherical aberration.

This section has shown that Gaussian beams, and their physical phenomena can be accurately modelled using φMC . A convex-plano lens was used to focus a Gaussian beam, but it is simple to implement other lenses given a triangulated mesh of the lens or an equation that describes the shape of the lens, e.g an aspheric lens.

4.4 Bessel Beams

Bessel beams have been the subject of intense research since their discovery in 1987 [135, 136]. Durnin noticed that the solution to the Helmholtz equation of the Bessel type were independent of the direction of propagation. This means that the central core of the beam is generally more

diffraction resistant when compared to a Gaussian beam with a similar spot size. Bessel beams also have a property of “self-healing”, this means if an obstruction is placed in the path of the central lobe of the Bessel beam, the Bessel beam can then “heal” and reform past the obstruction [137]. However, it is physically impossible to create a “real” Bessel beam, as the Bessel beam can have infinite rings, which each carry the same amount of power, thus would require infinite amount of power [135]. Therefore all Bessel beams that are created experimentally are quasi-Bessel beams which are similar to their theoretical counterpart over a finite distance [135].

These two properties make Bessel beams an attractive avenue of research, as novel solutions to imaging problems. There is also some debate among physicists as to whether these phenomena are justly labelled, or if they glib terms used to make Bessel beams seem better than they are [138–142].

4.4.1 Theory

As before with the Gaussian beam, the theory behind the Bessel beam must be discussed before we can model the beam in φMC . The electric field can be described using Eq. (4.26) [143]:

$$E(r, z) = E_0 \sqrt{\frac{2\pi k z w_0 \sin(\beta)}{z_{max}}} \exp\left(-\frac{z^2}{z_{max}^2} - \frac{i\pi}{4}\right) J_0(kr \sin(\beta)) \exp(ikz \cos(\beta)) \quad (4.26)$$

Where:

- k is the wavevector, $k = \frac{2\pi}{\lambda}$ [m];
- z is the propagated distance [m];
- β is the angle the wavefront propagates at (see Fig. 4.11) [rad];
- w_0 is the $\frac{1}{e^2}$ width of the input Gaussian beam [m];
- J_0 is the Bessel function of the first kind, zeroth order;
- r is radial distance from the optical axis [m].

Equation (4.26) gives the electric field for a Bessel beam. The intensity can be calculated using:

$$I(r, z) = \frac{c\epsilon_0 |E|^2}{2} \quad (4.27)$$

Using the definition total power transmitted by a beam as:

$$P = \frac{\pi I_0 w_0^2}{2} \quad (4.28)$$

Where I_0 is defined as on axis intensity of the incident Gaussian beam.

$$I_0 = \frac{c\epsilon_0 E_0^2}{2} \quad (4.29)$$

Substituting Eqs. (4.26), (4.28) and (4.29) into Eq. (4.27) yields:

$$I(r, z) = \frac{4k_r P}{w_0} \frac{z}{z_{max}} J_0^2(k_r r) \exp\left(-\frac{2z^2}{z_{max}^2}\right) \quad (4.30)$$

Where:

- k_r is the radial wavevector, $k_r = k \sin(\beta)$;
- P is the power of the incident Gaussian beam.

A Bessel beam can be formed by an axicon lens (see Fig. 4.11) or by diffraction through a ring, or through the use of a spatial light modulator. All the simulations of Bessel beams in this thesis use the axicon method of generating a Bessel beam, thus only axicons will be discussed. Figure 4.11 shows the geometry of a Bessel beam formed by an axicon. Using simple geometry and Snell's law the following equations can be derived to describe various properties of a Bessel beam formed by an axicon [144].

The propagation depth of a Bessel beam is defined as the distance from the tip of the axicon to the end of the "Bessel region". However, in reality the Bessel beam will continue to propagate slightly past this depth. Equation (4.31) shows the propagation depth of a Bessel beam where \cot is the cotangent function ($\cot x = \frac{1}{\tan x}$).

$$z_{max} = R(\cot(\beta) - \tan(\alpha)) \quad (4.31)$$

The propagation angle of the conical waves, β can be calculated using Snell's law and α the angle of the axicon:

$$\beta = \arcsin(n \sin(\alpha)) - \alpha \quad (4.32)$$

The central core of a Bessel beam is defined as the distance to the first zero of the Bessel beam. Equation (4.33) shows the radius of the core, where 2.405 is derived from the position of the first zero of the Bessel function.

$$r_o = \frac{2.405}{k \sin(\beta)} \quad (4.33)$$

Finally, the spacing between Bessel beam rings is:

$$\Delta\rho = \frac{\lambda}{2 \sin(\beta)} \quad (4.34)$$

4.4.2 Validation

To ensure that the method described in Section 4.2 works as intended for Bessel beams several tests are compared to theoretical expressions and experimental data.

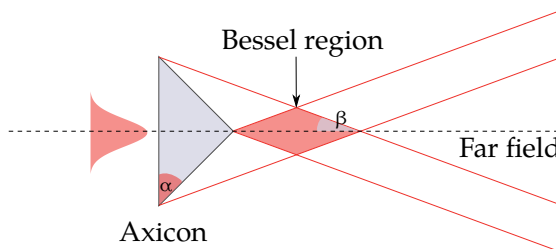


Figure 4.11: Geometry of a Bessel beam, generated by an axicon lens. β is the angle with the optical axis, and the angle of the conical waves. α is the axicon angle.

Comparison to a theoretical Bessel beam

To compare with a theoretical Bessel beam, a Bessel beam is modelled in φMC , and propagated through air into the "Bessel region" and then propagated into the far field to ensure the beam follows the theory in both these regions.

Figure 4.11 shows the set-up for the *in-silico* experiments. The Bessel beam is created with an axicon (conical) lens with an opening angle (α) of 5° , and a radius of 12.7 mm . The input beam is Gaussian in profile with a $\frac{1}{e^2}$ diameter of 1 mm , and a wavelength of 488 nm . The Bessel beam is then propagated to a detector screen 10 mm away from the tip of the axicon, which is in the middle of the “Bessel region” for the first test. For the second test the Bessel beam is propagated past the “Bessel region” into the far field. The detector screen has a size of $40\text{ }\mu\text{m} \times 40\text{ }\mu\text{m}$ with a bin resolution of $1\text{ }\mu\text{m}$. 8×10^{10} photon packets were simulated taking ~ 1 hour on an 8 core Intel Xeon 3.5Ghz machine.

Equation (4.30) gives the profile of a theoretical Bessel beam at a depth z_{max} , this is plotted against the simulation setting the various constants to (see Eq. (4.35)), with the simulation similarly normalised to the maximum intensity of the image generated. Figure 4.12 shows this comparison.

$$\frac{4k_r P_z}{w_0 z_{max}} e^{-2\left(\frac{z}{z_{max}}\right)^2} = 1 \quad (4.35)$$

Figure 4.13 shows the profile of the Bessel beam in the far field, where the theory predicts it becomes a ring. φ MC can also model the self-healing property of Bessel beams, this is shown in Fig. 4.14.

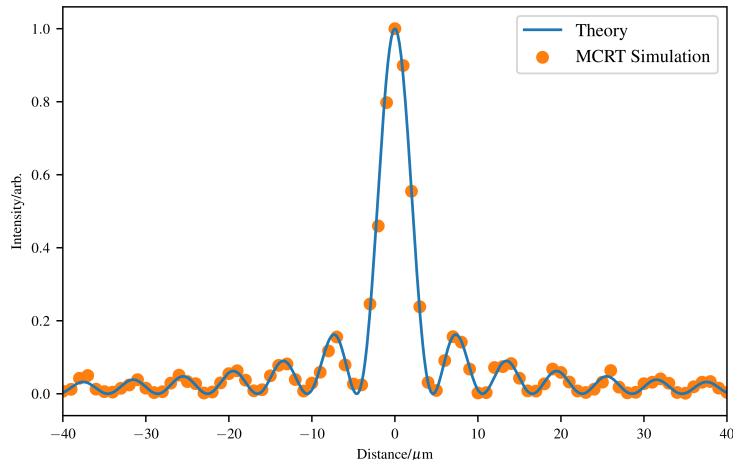


Figure 4.12: Comparison of theoretical and MCRT simulation of a Bessel beam, with intensity normalised. The results from φ MC show good agreement with the theory.

Comparison to experimental data

To ensure our algorithm works in turbid media, experiments were carried out by our collaborators, S. Reidt *et al.*, at the University of Dundee. These experiments allow us to test our algorithms ability to simulate scattering of Bessel beams in turbid media. S. Reidt *et al.* carried out an experiment where a Bessel beam was propagated through a medium of varying turbidity. A laser, wavelength 488 nm , with a Gaussian profile is shone on an axicon lens, with angle 5° . The laser beam had a $\frac{1}{e^2}$ diameter of 2 mm .

The Bessel beam was allowed to propagate through the air for 10 cm before entering a cuvette of side 2 mm . The cuvette was filled with $500\text{ }\mu\text{L}$ of water, and various volumes of a scattering agent added.

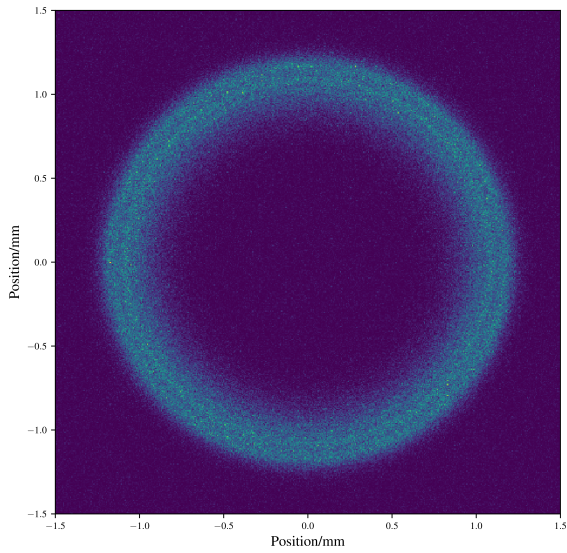


Figure 4.13: Bessel beam in the far field. Bessel beams in the far field become ring beams. Image shows a slice of intensity through the medium.

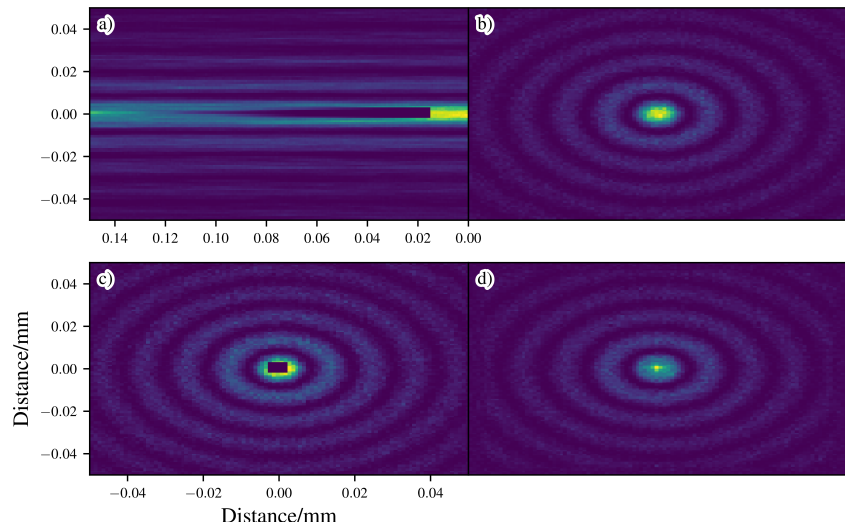


Figure 4.14: Illustration of the Bessel beams self-healing property. Highly absorbing cube placed near the top of the medium. Figure shows that the Bessel beam forms further down the optical axis. a) shows side on view with the obstacle at 0.02 mm, b) shows top down view at surface of the simulated b=medium before the obstacle, c) shows top down view in the middle of the obstacle, and d) shows the top down view after the Bessel beam has “healed”.

The scattering agent used is intralipid 20 % (Sigma-Aldrich), which is diluted as shown in Table 4.1. Figure 4.16 shows the optical properties of Intralipid 20 %. Dilutions of Intralipid are kept below 2% scattering particle concentration, so that the scattering exhibited by the

intralipid is in the independent scattering regime[‡]. This allows the linear scaling of the optical properties by concentrations [145, 147, 148]. Images of the Bessel beam as it emerges from the cuvette are taken for comparison with our algorithm. Figure 4.15 shows the experimental set-up.

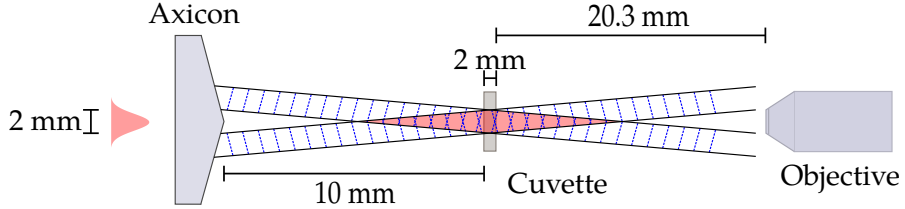


Figure 4.15: Experimental set-up for propagating a Bessel beam through a cuvette filled with varying concentrations of Intralipid 20%. Bessel beam is imaged by an $20\times$ objective lens and a Grasshopper 3 camera.

Intralipid	μL	Intralipid concentration		Optical properties Scattering coefficient/ m^{-1}
		H_2O	Volume/%	Scattering particle/%
0	500	0.00	0.00	0.00
2	500	0.39841	0.0908	557.14
4	500	0.79365	0.1816	1114.28
6	500	1.18577	0.2724	1671.42
8	500	1.57480	0.3632	2228.56
10	500	1.96078	0.4534	2785.71
12	500	2.34375	0.5448	3342.84

Table 4.1: Intralipid solutions used for experiment, see also Fig. 4.16.

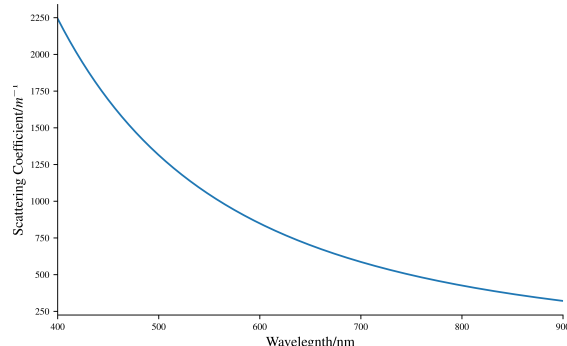


Figure 4.16: Scattering properties of 20% Intralipid [149].

To model within φMC , we simplify the experimental setup considerably. The simulation models the propagation of photon packets through the axicon to its conical surface. On the conical surface the Huygens-Fresnel principle is invoked, and the packet is sampled onto the surface of the medium (cuvette). The sampling of the photon onto the surface of the medium,

[‡]The independent scattering regime is where g is dependent on the size, shape and material properties of the scattering particle, and the material properties of the bulk material, but not the number of scattering particles [145, 146].

speeds the algorithm up, as it does not need to simulate the photons that would “miss” the medium. From there the usual MCRT method propagates the packet through the medium while tracking its phase, and scattering the packet until it leaves the medium. If the packet leaves the medium to any side other than the far side of the cuvette (e.g any side of the cuvette not facing the objective lens), then it is discarded. If the packet leaves the medium on the objective lens facing side, then the packet is recorded by its phase onto an area element. For each intralipid concentration 6.4×10^{10} photons are run over 64 cores, taking ~ 3 hours for the $12\mu L$ intralipid volume. Once all the packets have been run, the phase is converted into intensity, as in Eq. (4.3), but in 2D.

Figures 4.17 and 4.18 show the results from the experiment and simulation. The simulation shows good agreement with experimental data within experimental and simulation uncertainty.

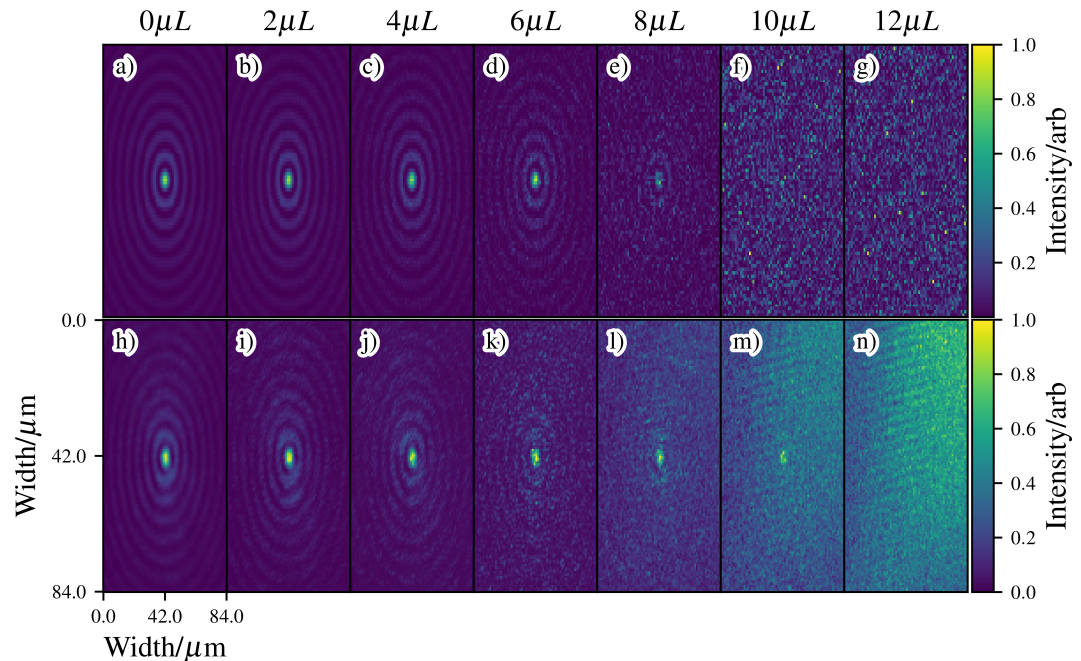


Figure 4.17: Comparison of experimental and simulation data for propagation of a Bessel beam produced by an axicon, through mediums of various turbidity. Images a) to g) is the data from φ MC, and h) to n) are the experimental data. Volumes along the top are the volume of Intralipid in each solution as in Table 4.1. All images are cropped so they are the same size and normalised to the maximum value in each image.

Discussion

As mentioned in previous sections, the power of the MCRT method is that we can track virtually any quantity in the simulation. Alongside generating intensity images, we can also track the average number of scattering per packet, a quantity that is hard to measure experimentally. Table 4.2 shows the average number of scattering per packet alongside the optical depth of the medium from the source to the image plane. The simulations show that above ≈ 2 scatterings of a packet the Bessel beam is “destroyed” and the generated image becomes washed out with noise.

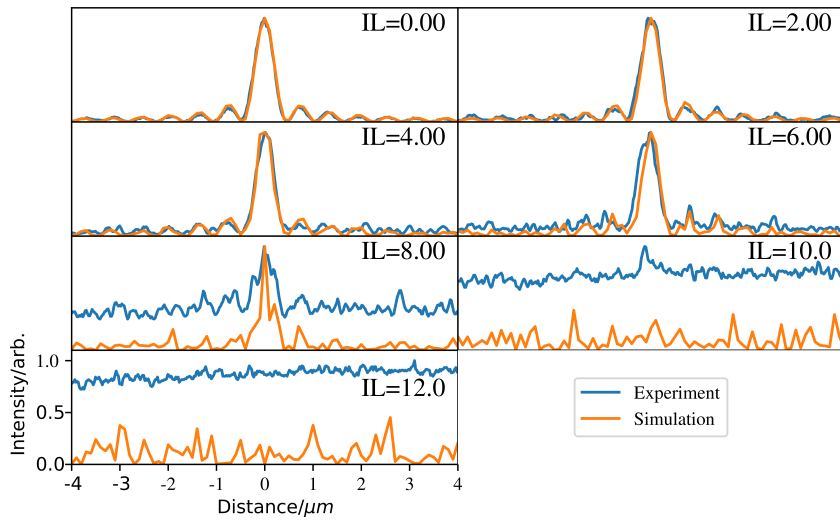


Figure 4.18: Line graph plots of slices taken through the generated and experimental images as shown in Fig. 4.17.

Volume IL/ μL	Avg # scatterings	Optical depth
2	0.734	1.114
4	1.225	2.229
6	1.594	3.342
8	1.899	4.457
10	2.168	5.571
12	2.417	6.686

Table 4.2: Average number of scattering per packet and the optical depths for different volumes of Intralipid.

Originally the medium was modelled as in the experiment, a 2 mm^3 volume. The image created was thus a 2001×2001 with a resolution of $1 \mu\text{m}$. To achieve a good signal to noise ratio for this set-up 6.4×10^{12} packets needed to be run, taking ~ 70 hours on a computer cluster using 64 cores. This was sufficient to get a good signal to noise ratios for all the simulations up to $6 \mu\text{L}$. However, the number of packets needed to get a good signal to noise ratio for $8 \mu\text{L}$ and above was prohibitively computationally costly. Therefore the modelled medium was shrunk in the x and y directions giving: $0.5 \text{ mm} \times 0.5 \text{ mm} \times 2.0 \text{ mm}$. This allowed a smaller image (501×501), whilst keeping the same resolution. Shrinking the medium also has the benefit that the photons are confined closer to the image plane, thus ensuring more photons hit the plane in comparison to the larger medium.

Shrinking the medium's size does have some drawbacks. First the Bessel beams propagation depth rely on the input beams width (see Eq. (4.31)). The input beams width was kept constant between the shrinking of the volumes size. However, shrinking the medium's size in the x and y directions gives the same effect as using a smaller input beam. Therefore, the x and y dimension were carefully chosen such that the Bessel beam would still form a Bessel beam at the image plane. The second issue with shrinking the medium is that some packets may be lost. This means that in the larger medium a packet may scatter toward an x or y medium wall and then scatter back into the centre of the medium and then is recorded. However, this same packet in

the smaller medium would be lost as the packet would exit the medium and cease to be tracked. It is not expected that this will cause much of an issue as any scattering event already degraded the quality of the beam, as that packet is no longer coherent with the rest of the packets, thus it will not contribute positively to the Bessel beam. To ensure this is not an issue, results from a larger medium are compared to that of the smaller medium in Fig. 4.19. The larger and smaller medium yield the same results (within Monte Carlo noise) for Intralipid volumes less than $8 \mu\text{L}$. At $8 \mu\text{L}$ the smaller medium has a Bessel beams central core, whilst the larger medium is noisy, and forms no Bessel beam. This test has shown that shrinking the medium allows accurate modelling of the propagation of a Bessel beam through a turbid medium while using less computational resources.

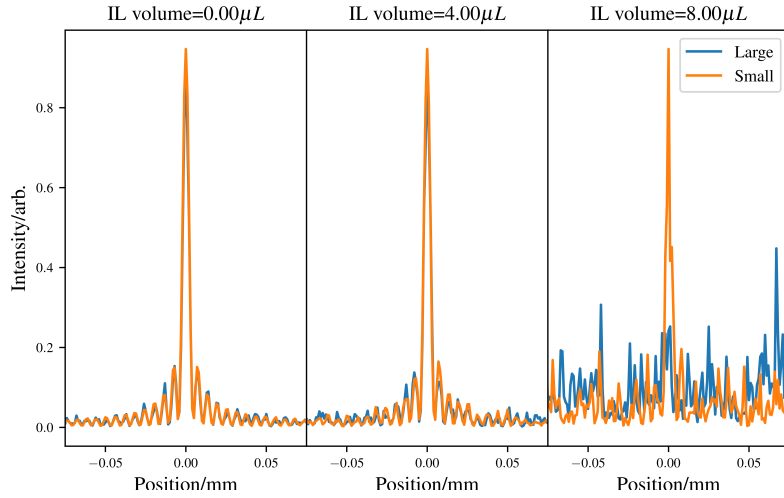


Figure 4.19: Comparison of a larger medium, 2 mm^3 versus that of a smaller medium, $0.5 \text{ mm} \times 0.5 \text{ mm} \times 2.00 \text{ mm}$. The figure shows that the smaller medium gives a better signal to noise ratio, whilst still accurately modelling the experiment.

4.5 Higher Order Bessel Beams

Higher order Bessel beams (HOBBs), are Bessel beams where the electric field has an extra term of $e^{-il\varphi}$, as shown in Eq. (4.36), and $l \neq 0$. HOBBs have found use for optical trapping targets that are reflective/low refractive index, and optical manipulation [150,151]. Our technique outlined in the preceding sections, can also be applied to arbitrary higher order Bessel beams.

As before, the electric field of a l^{th} order Bessel beam is:

$$E(r, \varphi, z) = E_0 J_l(k_r r) e^{-ik_z z} e^{-il\varphi} \quad (4.36)$$

Where:

- 1 is the order of the beam [-];
- $k_z^2 + k_r^2 = k^2$, where k^2 is the wavevector [m^{-1}];
- r , φ , and z are the cylindrical coordinates [m , rad , m];
- and J_l is the l-order Bessel function of the first kind [-].

To generate higher order Bessel beam, a helicon is used. A helicon (shown in Fig. 4.20) is an axicon attached to a helix phase delay element. The helical element imparts a helical phase

delay to photon packets as they pass through the element.

The distance travelled though the helicon is shown in Eqs. (4.37), (4.38) and (4.40) [152]. h_1 is the path length travelled by a photon through the helical element. h_2 is the path through an axicon, and Δh is the height of the helical discontinuity.

$$h_1 = \frac{l\phi\lambda}{(n-1)2\pi} \quad (4.37)$$

$$h_2 = r \tan(\alpha) \quad (4.38)$$

$$h_3 = h_1 + h_2 \quad (4.39)$$

$$\Delta h = \frac{l\lambda}{n-1} \quad (4.40)$$

Where ϕ is the azimuthal angle, r is the radial position, l is an integer that describes the order of the Bessel beam, and α is the axicon angle.

The path length in the above equations can be converted into a phase delay by considering the transmission functions of the individual elements [153–156]:

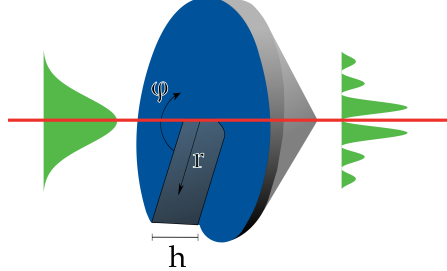


Figure 4.20: Helical delay element attached to an axicon. The Axicon introduces a radial delay in addition to that of the helical element. If the input beam is a Gaussian, the output beam is a higher order Bessel beam, $l > 0$.

$$T_1(\varphi) = e^{-ik(n-1)h_1} = e^{-il\phi} \quad (4.41)$$

$$T_2(r) = e^{-ik(n-1)h_2} = e^{-ik_r r} \quad (4.42)$$

$$T_3(r, \varphi) = T_1 * T_2 = e^{-ik_r r - il\phi} \quad (4.43)$$

$$(4.44)$$

Where T_1 is the transmission function for the helical element, T_2 is the transmission function for the axicon, and T_3 is the total transmission function. Using the small angle approximation for β and Eq. (4.32), and knowing $k_r = \sin(\beta)$ yields the phase delay as a function of angle and radial position:

$$\varphi(\phi, r) = k(n-1)r\alpha + l\phi \quad (4.45)$$

To implement a helicon in the φMC algorithm, an additional helical phase delay is added. The additional delay is implemented by adding $l\phi$ where $0 < \phi < \frac{2\pi}{l}$. An actual helix element is not modelled explicitly in the code, but rather just the phase delay. This method is similar to using a spatial light modulator in an experiment to impart a phase delay on a beam.

Figure 4.21 shows the comparison between theoretical higher order Bessel beam and the higher order beam simulated by φMC .

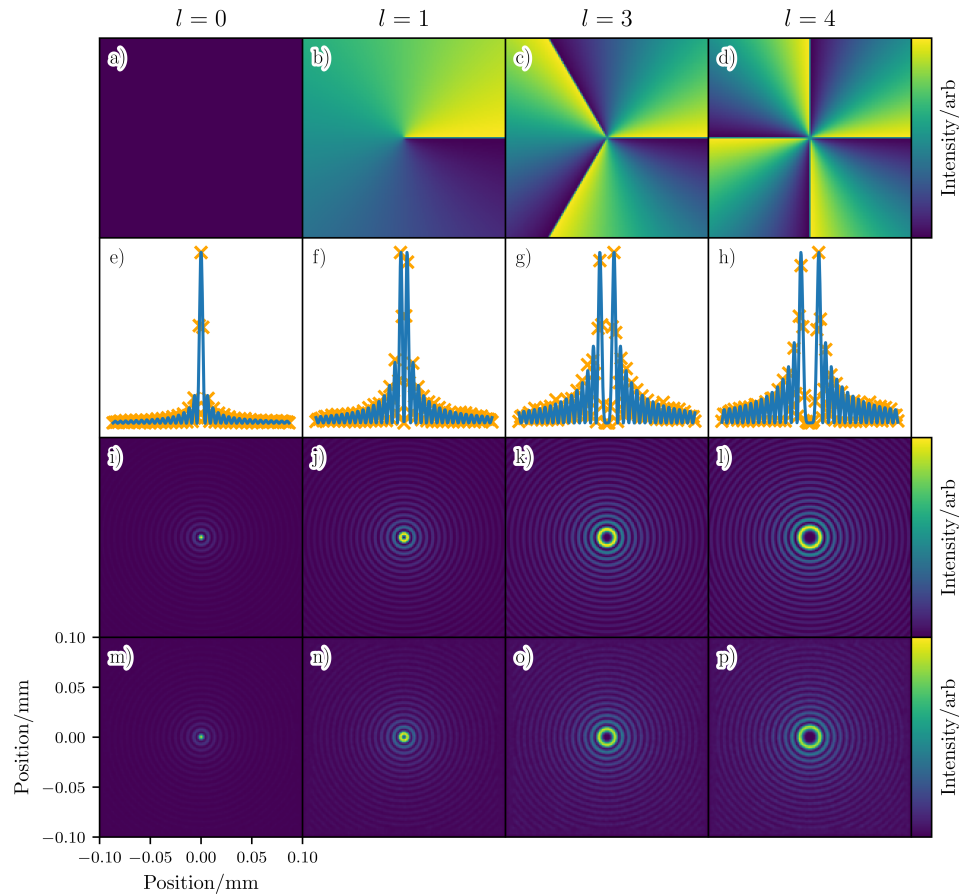


Figure 4.21: HOBBs. a) to d) show the phase shift due to the helical element. e) to h) show line plots of the simulation data compared to the theory. i) to l) and m) to p) show the higher order Bessel beam images for theory and simulation data respectively.

4.6 Comparison

As Bessel and Gaussian beams are radically different from one another it is hard to directly compare the two beams. Gaussian beams carry all their power in the “central core” of the beam, whereas in a Bessel beam, it carries the same amount of power in each ring. Bessel beams also have a much larger depth of focus than Gaussian beams. This section attempts to compare the two beams, to predict which beam performs better in a heavily scattering medium using φ MC. Bessel beams are expected to perform better than Gaussian beams, due to their self-healing properties and non-diffractive core, this section aims to quantify how this property may or may not help penetration through a highly scattering medium.

As mentioned, Bessel beams and Gaussian beams are not alike, so to ensure a fair comparison the Bessel beams central core width is set to that of the Gaussian beam’s waist.

$$r_0 = \frac{\kappa}{k \sin\beta} \quad (4.46)$$

Where κ is a constant that determines the metric used to measure the Bessel beam’s core, and the other symbols have the same meanings as before. For $\kappa = 2.408$ the radius is measured from the maximum of the core to the first zero of the Bessel beam. $\kappa = 1.75$ measures the Bessel beam’s core from the maximum to $\frac{1}{e^2}$ of the maximum. For both beams central cores to be equal, the axicon used to generate the Bessel beam is adjusted. This is achieved by calculating the “correct” α based upon the optical setup used to focus the Gaussian beam. Using the small angle approximation[§] and $\kappa = 1.75$ we can compare the Bessel beam’s core radius to a Gaussian beam’s waist:

$$\frac{1.75\lambda}{2\pi\sin\beta} = \frac{2\lambda f}{\pi D} \quad (4.47)$$

$$\alpha = \frac{1}{n-1} \arcsin \left(\frac{1.75D}{4f} \right) \quad (4.48)$$

Where α is the axicon angle as before, n is the refractive index of the axicon, D is the $\frac{1}{e^2}$ diameter of the incident Gaussian beam on the lens, and f is the focal length of the lens used to focus the Gaussian beam. Both D and f are properties of the optical system used to focus the Gaussian beam. The lens used to focus the Gaussian beam is the same as used in the previous section to validate that φ MC can model a Gaussian beam, a convex-plano lens, with radius of curvature 4.6 mm, a working distance of 8.5 mm and thickness of 2.2 mm.

The first simulation comparisons carried out between the Bessel and Gaussian beams is to use the same power to generate both beams. The beams are then propagated through mediums of varying degrees of Intralipid solution. Volumes of 0.0, 26, 52, 78, and 104 μL are used of Intralipid in 500 μL of water. The medium has a volume of 0.1 mm \times 0.1 mm \times 0.2 mm, and voxel resolution of 1 μm . For both beams a wavelength of 488 nm and a power of 1 mW is used. One hundred million packets are simulated for each simulation. The results of this are shown in Figs. 4.22 and 4.23

The results show that for the same power, Gaussian beams propagate deeper into the medium compared to Bessel beams. This is to be expected as in a Gaussian beam all the power is in its “central core”, whilst the power is evenly distributed between all the Bessel beam’s rings. Therefore, for a second comparison the power given to the Bessel beam is such that the central core maximum matches that of the Gaussian beam’s at its focus for the case where there is no

[§]for small α and β : $\beta = (n-1)\alpha$.

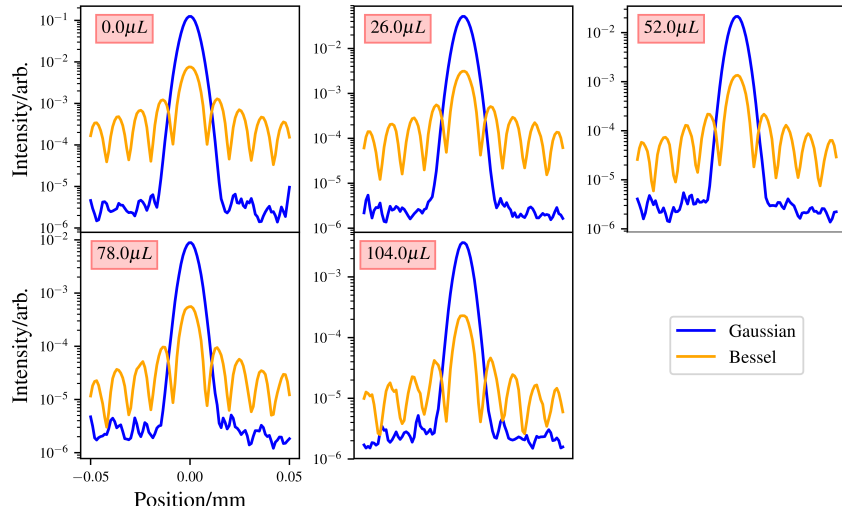


Figure 4.22: First comparison of Bessel and Gaussian beams with equal power used to generate both beams. Plots taken at the Gaussian beams focus. The maxima at the sides of the Gaussian beam in the $0.0\mu\text{L}$ plot are due to simulation effects, mainly the small size of the medium not allowing photons from further off the optical axis to interfere destructively.

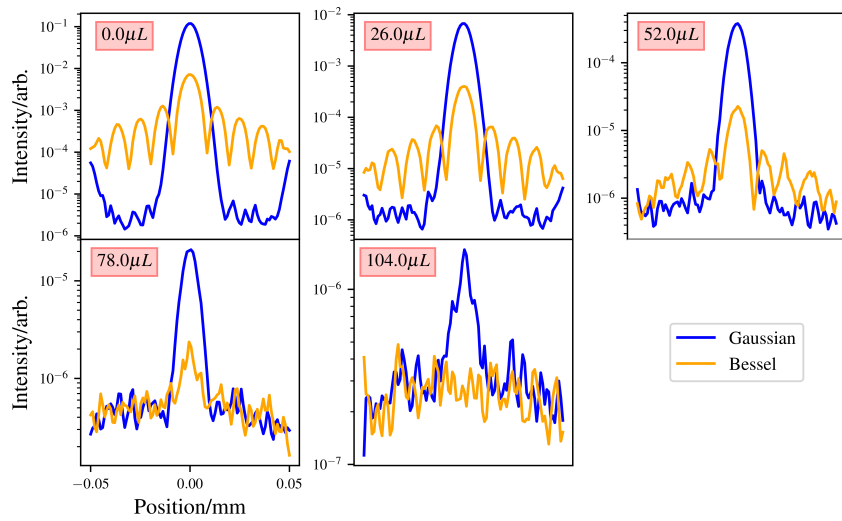


Figure 4.23: First comparison of Bessel and Gaussian beams, with equal power used to generate both beams. Plots taken at the bottom of the simulated medium.

scattering. To achieve this the Bessel beam was given $\sim 15\times$ the power given to the Gaussian beam. The results of this comparison are illustrated in Fig. 4.24.

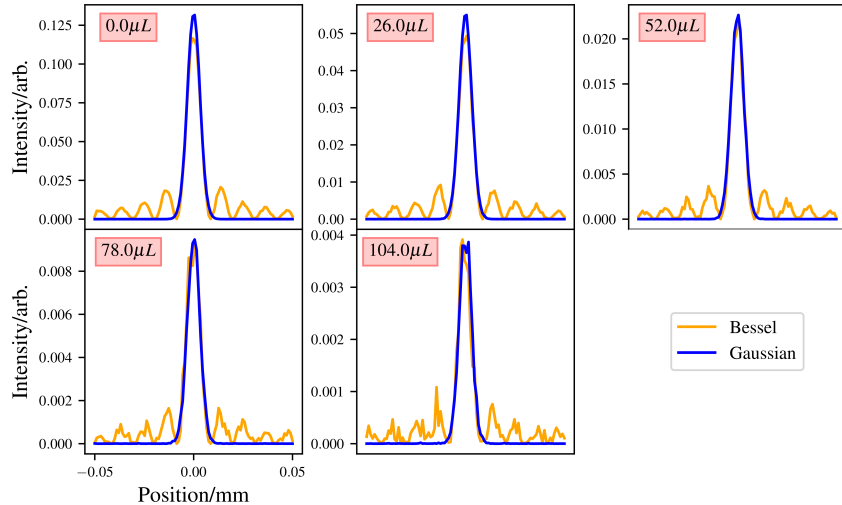


Figure 4.24: Second comparison of Bessel and Gaussian beams for the case where the power given to each beam, yields the same maximum at the Gaussian beams focus. These plots are taken from the Gaussian beams focus.

These results show as expected that the Bessel beam now performs comparably with the Gaussian beam in lower scattering media, with a drop off in performance in the higher scattering media.

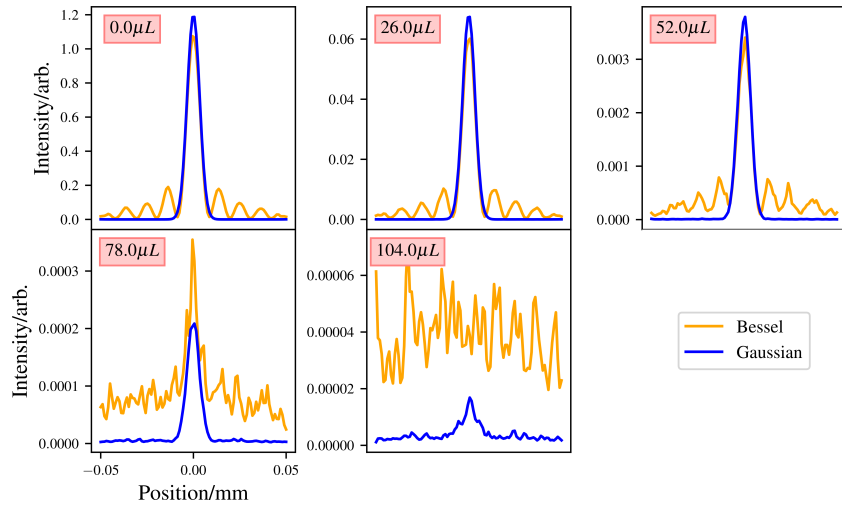


Figure 4.25: Comparisons of unequal powered beams at the bottom of scattering medium.

4.6.1 Discussion

For equal power beams in the previous section, Gaussian beams perform “better” in the highly scattering mediums. Though this is expected due to the Bessel beams property that the power in the beam is spread evenly over its rings. Thus, the power in the central lobe is much less than that of the Gaussian beam.

To give a slightly more fair comparison of intensity in the central lobes of the beams, the Bessel beam was given $15\times$ more power than the Gaussian beam. This allows a better comparison between the Gaussian beams’ core and the Bessel beam’s core and gives a more comparable intensity between the beams at the location of the Gaussian beams focus. In this case, the Bessel beam appears to perform better in a highly scattering medium, as shown in Fig. 4.25. The Bessel beam shows comparable intensity with the Gaussian beam in the first three mediums, though the Gaussian beam out performs the Bessel beam in the higher scattering media. It would appear that the Bessel beams self-healing property does not help a Bessel beam propagate through a highly scattering medium. Figure 4.26 shows how the Bessel beam may become degraded due to scattering. As photons propagate though the medium they interfere with one another constructively and destructively to form a Bessel beam. However, if enough photons are scattered, then the Bessel beam becomes degraded and thus no longer is a Bessel beam, as these photons are no longer coherent with the rest of the beam, so they act as a negative factor in the beams formation. Another reason that the “self-healing” property of the Bessel beam does not “save” the beam from scattering is that the “self-healing” is not self-healing. The self-healing in reality is just photons from further off the optical axis forming the Bessel beam further down the optical axis, e.g the photons that are impeded by the blockage are stopped, but the photons that are not impeded form a Bessel beam as expected. If you placed a blockage in front of the Bessel beam larger than the width of the input beam, then the Bessel beam would not form at all.

Bessel beams do have their positives, their self-healing property does help “reform” the beam past small blockages, and their depth of field is superior to an equivalent Gaussian beam, as their central cores is “non-diffractive”.

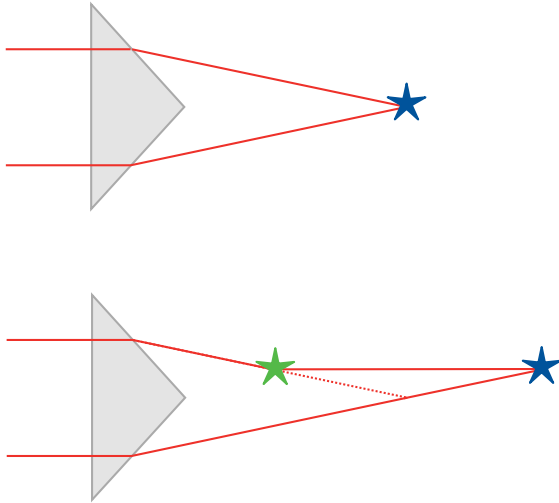


Figure 4.26: Illustration of how a Bessel beam becomes degraded due to scattering. Top image shows how two photons propagate through the axicon and constructively interfere to produce a Bessel beam. Bottom image shows how scattering can affect this process.

4.7 Conclusion

This chapter has shown that it is possible to transform a traditional particle behaviour MCRT method into a method that allows the simulation of quasi-wave/particle behaviour of photons. This is achieved by introducing two principles to the algorithm: the tracking of the complex phase of each packets and the Huygens-Fresnel principle. The tracking of the complex phase of each packet allows interference of the quasi-wave/particles to be simulated. The Huygens-Fresnel principle allows diffraction to be accurately modelled. φMC has been thoroughly validated against several experiments where modelling the wave behaviour of light is vital to the experiment. Alongside the above, presented in this chapter is the modelling of complex beam types: Gaussian and Bessel beams. Both beam types have been validated against both theoretical and experimental results. Finally, Gaussian beams and Bessel beams were compared with one another in a highly scattering medium, where Bessel beams appear to give better performance. However, φMC is not a silver bullet for modelling these complex beams in a scattering medium. Depending on the problem at hand, the computational load can be excessive. For example, if you want to know the intensity of the beam at all locations though a large ($> 1mm^3$) scattering medium with a complex 3D structure, then the time taken to get a good signal to noise ration may be computationally prohibitive. Though it is expected that in most cases the intensity is not needed at all locations in a medium, and an image is all that is need to be calculated, then even in a complex 3D structure φMC should perform better than the methods listed at the start of this chapter[¶]. Where φMC excels is that it can accurately model scattering effects on the propagation of complex beams through scattering media.

[¶]Though to achieve better performance with the current code, adaptive mesh grids would have to be implemented.

Chapter 5

Modelling Autofluorescence in Skin for Novel Biomarkers of Cardiovascular Diseases

5.1 Introduction

Cardiovascular diseases (CVDs) are the leading cause of death in the world [157]. It is estimated that around 18 million people died in 2016 from CVDs, accounting for 31% of global deaths [157]. Despite the decreasing burden of CVDs in the UK, it was still the number two cause of death in the UK in 2014 [158].

Currently risk factors are used to try to determine if a patient has cardiovascular disease (CVD). However, these risk factors are only a “causal pathway leading to the disease” [159].

The risk factors such as high blood pressure, smoking, diabetes, physical inactivity, and dyslipidemia do not fully explain incidence of disease [160, 161]. Therefore research has moved to examining more novel biomarkers for detecting the disease. Among these novel biomarkers, the autofluorescence response of tissue is of much interest.

Autofluorescence is the natural fluorescence released by biological structures upon excitation by light. Autofluorescence is particularly attractive as a biomarker as it requires no exogenous dyes, which can be toxic, non-specific, or interfere with biological function [162]. In tissue there are several fluorophores responsible for this autofluorescent response, including: NADH (nicotinamide adenine dinucleotide), structural proteins like collagen and elastin, aromatic amino acids (tyrosine and tryptophan), porphyrins, and FAD (flavin adenine nucleotide) [163]. Changes in the autofluorescent response of tissue has been linked to cancer, Alzheimers, diabetes and CVDs [164–168]. Autofluorescence can be linked to these diseases as the fluorophores responsible for the autofluorescence either originate in the mitochondria, or are involved in important biochemical pathways that regulate apoptosis, free-radical generation, oxidative stress and biomolecular sensing of glucose, oxygen and nitric oxide.

NADH has recently been the subject of interest in particular as a biomarker for CVDs [169–171]. NADH is an intracellular co-enzyme that is a biomarker for metabolic activity, and mitochondrial anomalies. It is involved in mitochondrial function, energy metabolism, calcium homoeostasis, gene expression, oxidative stress, ageing, apoptosis and glycolysis (see Fig. 5.1). Therefore if there is dysfunction, then the autofluorescent signal from NADH will be affected, thus it can be used as biomarker for disease.

Despite the appeal of using autofluorescence to diagnose and assess disease risk more research needs to be carried out on various unknowns: information on the location of fluorescence, which fluorophores contribute to the signal and how much, how much the optics of tissue affect the signal, and the variability of the signal from different locations on the body. This chapter aims to determine how much the tissue optics affects the autofluorescent signal, which fluorophores contribute to the signal, and from which layer of the skin do they contribute from. Finally we introduce our ameboMCRT algorithm, created to determine the relative concentrations of the intrinsic fluorophores in the skin to assess clinical outcomes.

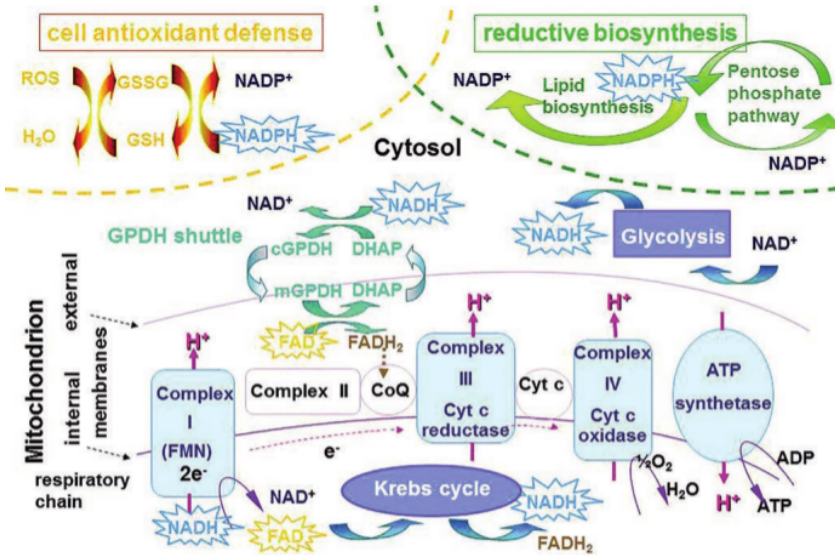


Figure 5.1: Simplified schematic showing the roles of NADH and FAD in various different metabolic pathways. The star boxes indicate fluorescing forms of NADH and FAD. Taken from Croce et al. [172].

5.2 Skin Model

So far in this thesis all tissue models have been simplified, by assuming that tissue is a homogeneous structure with uniform optical properties. However, this is not the case in reality. Tissue is inhomogeneous with nonuniform optical properties. However, to create a one to one model of tissue in a simulation is impractical due to the resolution required to resolve all the constituent parts of the tissue down to the cell level. Therefore, we need to make a compromise between reality and what is possible to model efficiently. This section presents a five layer model of human skin.

Dermatologists categorise the skin into several layers based upon the morphology, function, and contents of each layer [173, 174]. The layers are named from outer layer to inner most layer: stratum corneum, stratum lucidum, stratum granulosum, stratum spinosum, stratum basale, papillary dermis, reticular dermis, and hypodermis. Not all these layers are optically distinct, are too small to model or not present in a given location on the body. Therefore, we simplify this into just 5 layers: stratum corneum, epidermis, papillary dermis, reticular dermis, and hypodermis, with the epidermis comprising of stratum lucidum, stratum granulosum,

stratum spinosum, stratum basale. Figure 5.2 shows the geometry of this model.

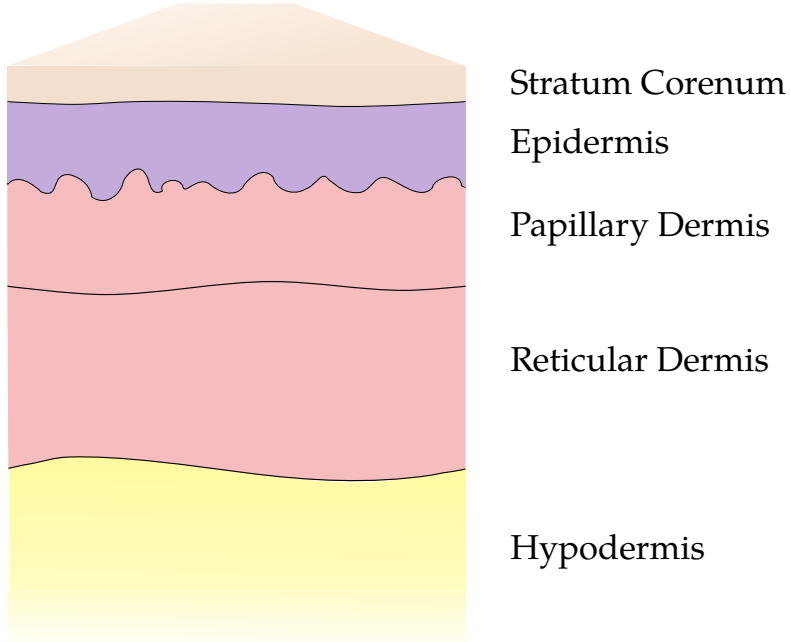


Figure 5.2: Illustration of our five layer skin model. Image not to scale.

Each of these layers have various amounts of chromophores and scatterers. To accurately model these various chromophores and scatterers, and therefore the skin, we must discuss the biological make up and spatial structure of the skin.

Stratum Corenum

The outer most layer of the skin is the stratum corenum. This layer mostly consists of dead skin cells (keratinocytes). Keratinocytes, which make up approximately 80 percent of the cells in the epidermis, are born in the stratum basale and live for approximately 14 days. During this period they move upwards to the surface of the skin undergoing a series of complex morphological and metabolic events, which ends with the cells undergoing apoptosis by the time they reach the stratum corenum. The keratinocytes are flat in shape, cornified and stacked on top of each other in this layer. The function of this layer is to be a protection barrier to prevent damage, infection and diffusion of unwanted chemicals further into the skin. The stratum corenum also prevents water loss and provides some UV protection [173, 174].

Epidermis

Below the Stratum corenum is the epidermis. The epidermis consist of several layers that are optically similar so we restrict our model to modelling this as one whole layer. The layers that make up the epidermis are the stratum basale, stratum spinosum, stratum granulosum, and stratum lucidum*. Each of these layers are distinct from one another, in the fact that

*The stratum lucidum only appears in areas of the body where skin is thick, e.g the palm or the sole of the foot.

the keratinocytes in each layer are different from one another. In the stratum lucidum the keratinocytes are dead, and fairly flat. In the stratum granulosum the keratinocytes are grainy and becoming fairly flat in comparison to the layers below. In the Stratum spinosum the keratinocytes appear spiny (hence the name of the layer), and are polyhedral in shape. It is in the stratum spinosum that the cells begin to become keratinized and start the process of dying as they move upwards. Finally the last layer of the epidermis, the stratum basale, is the layer where the keratinocytes are born. Here the keratinocytes are columnar or cuboid in shape.

The purpose of the epidermis is as before to provide a protective barrier to the underlying layers. In the stratum basale there are also melanocytes which produce the pigment melanin which is responsible for the color of the skin, and providing some protection from harmful UV light. Other types of cells found in the epidermis are Langerhans cells and Merkel cells which are part of the immune system and nervous system respectively. Overall the epidermis provides protection from mechanical stress, flexibility to the skin, UV protection, retains water, and stops foreign bodies or chemicals from entering the skin [173, 174].

Dermis

The dermis is the layer of skin below the epidermis, and makes up the majority of the skin by size. The cellular makeup of the dermis is different from that of the epidermis, as the dermis is mostly made up of filamentous or fibrous proteins such as elastin or collagen. The dermis also contains various nerves and blood vessels. The dermis is split into three layers; the papillary dermis, the reticular dermis, and the hypodermis. The boundary between the papillary and reticular layers is demarcated by the subpapillary plexus, which is a horizontal plane of blood vessels. The boundary between the reticular and the hypodermis is marked by an abrupt change from fibrous to adipose tissue. The function of the dermis is to protect from mechanical injury, thermal regulation, contains receptors of sensory stimuli, giving the skin pliability, elasticity and tensile strength [173, 174].

5.2.1 Optical Properties

With a discussion of what makes up the skin and what molecules contribute to the skin's optical properties, this section gives an account of how our model incorporates the optical properties of skin. First we will discuss the absorbers that are found in the skin and what their absorption properties are as a function of wavelength. Scattering properties of the several layers of tissue will then be discussed followed by a quick discussion on refractive indices and anisotropy values. Finally a discussion of the fluorophores found in the skin will be presented.

The first chromophore we will examine is blood. To model blood we first split blood into its deoxygenated and oxygenated components. This is done as the absorption coefficient differs between the two types of blood. We mix these two groups using the tissue oxygenation coefficient S . Blood absorption spectra are taken from S. Prahl [175]. Equations (5.1) and (5.2) give the absorption coefficients for oxygenated, deoxygenated, and whole blood.

$$\mu_{a,Oxy/DeOxy} = 150 \ln 10 \frac{\epsilon_{Oxy/DeOxy}}{64458} \quad (5.1)$$

$$\mu_{a,blood}(\lambda) = S\mu_{a,Oxy} + (1 - S)\mu_{a,DeOxy} \quad (5.2)$$

Where:

$\epsilon_{Oxy/DeOxy}$ is the extinction coefficient of hemoglobin [cm^{-1}];
 64458 is the molecular weight of hemoglobin [$g mol^{-1}$];

150 is the normal concentration of hemoglobin in blood [$g L^{-1}$]; and $\mu_{a,Oxy}$, $\mu_{a,DeOxy}$, and $\mu_{a,blood}$ are the absorption coefficients for oxygenated, deoxygenated and blood respectively [cm^{-1}].

We also include water in our skin model. Water's absorption spectrum is taken from the work of Wieliczka *et al* and Segelstein [49, 176].

The next chromophores are bilirubin and β -carotene. These chromophores are yellow/orange pigments. Bilirubin is usually responsible for the yellow skin colour seen in people with jaundice [177]. The spectra are taken from S. Prahl's compilation of PhotochemCAD data [178, 179]. Equations (5.3) and (5.4) give the absorption coefficients of bilirubin and β -carotene:

$$\mu_{a,Bilirubin}(\lambda) = \frac{\epsilon_{bilirubin}}{585} \ln 10 C_{bilirubin} \quad (5.3)$$

$$\mu_{a,\beta-Caro}(\lambda) = \frac{\epsilon_{\beta-Caro}}{537} \ln 10 C_{\beta-Caro} \quad (5.4)$$

Where:

$\epsilon_{bilirubin}$ and $\epsilon_{\beta-Caro}$ are the extinction coefficients for bilirubin and β -carotene respectively [cm^{-1}];

585, and 537 are the molecular weights of bilirubin and β -carotene [g];

finally, $C_{bilirubin}$, and $C_{\beta-Caro}$ are the concentrations of bilirubin and β -carotene in the skin [$g L^{-1}$].

Melanin is the next chromophore we model. To model melanin's absorption coefficient we use Eqs. (5.5) and (5.6), taken from [53].

$$\mu_{a,eumel}(\lambda) = 6.66 \times 10^{11} \times \lambda^{-3.33} \quad (5.5)$$

$$\mu_{a,phomel}(\lambda) = 2.9 \times 10^{15} \times \lambda^{-4.75} \quad (5.6)$$

Finally we use a base absorption coefficient to model the absorption due to the other parts of the skin that contribute to its optical properties, but individually do not have a large effect. The equation for modelling this was taken from I. Sahdi [52].

$$\mu_{a,base} = 7.84 \times 10^8 \times \lambda^{-3.255} \quad (5.7)$$

Figure 5.3 shows the absorption spectra for the above chromophores as a function of wavelength.

To create the five layer skin model we mix different amounts of the chromophores found in each layer, as described above. Equations (5.8) to (5.11) show the respective equations for the total absorption coefficient for each layer. These equations were adapted from [43, 53, 100].

$$\mu_{a,strat} = ((0.1 - 0.3 \times 10^{-4} \cdot \lambda) + (0.125(\lambda/10.)) \times \mu_{a,b}(\lambda)) \times (1. - W) + W \cdot \mu_{H_2O}(\lambda) \quad (5.8)$$

$$\begin{aligned} \mu_{a,epi} = & (\nu_m \cdot (\mu_{phomel}(\lambda) + \mu_{eumel}(\lambda)) + (\mu_{a,b}(\lambda) + \ln 10 \cdot \mu_{a,\beta-caro}(\lambda) \cdot C_{caro}) \\ & \times (1. - \nu_m)) \times (1. - W) + W \cdot \mu_{H_2O}(\lambda) \end{aligned} \quad (5.9)$$

$$\begin{aligned} \mu_{a,pap/ret} = & ((S \cdot \mu_{a,oxy}(\lambda) + (1. - S) \cdot \mu_{a,deoxy}(\lambda) + \ln 10 \cdot \mu_{a,\beta-caro}(\lambda) \cdot C_{caro} + \\ & \ln 10 \cdot \mu_{a,bili}(\lambda) \cdot C_{bili}) \cdot B + (1. - B) \cdot \mu_{a,b}(\lambda)) \times (1. - W) + W \cdot \mu_{H_2O}(\lambda) \end{aligned} \quad (5.10)$$

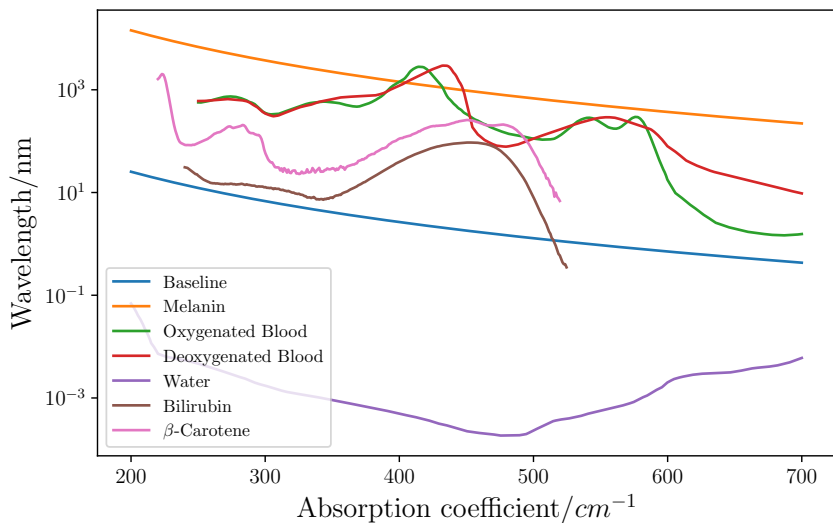


Figure 5.3: Absorption coefficients for the various chromophores found in our skin model.

$$\mu_{a,hypo} = ((S \cdot \mu_{a,oxy}(\lambda) + (1 - S) \cdot \mu_{a,deoxy}(\lambda)) \times B + \mu_{a,b}(\lambda) \cdot (1 - B)) \times (1 - W) + W \cdot \mu_{a,H_2O}(\lambda) \quad (5.11)$$

Where:

W is the volume fraction of water in a layer [-];

ν_m is the volume fraction of melanin in a layer [-];

B is the volume fraction of blood in each layer [-];

and all the other symbols have the same meanings as described above.

Table 5.1 shows the amount of each chromophore included in each layer, and the size adopted for each layer as well as the refractive index for each individual layer. Figure 5.4 shows the total absorption coefficient as a function of wavelength for the five layers.

Layer	Thickness/cm	Refractive index	Blood volume/%	Melanin volume/%	Bilirubin/gL ⁻¹	β -Carotene/gL ⁻¹	Water volume/%
Stratum Corenum	0.02	1.50	0.0	0.0	0.0	0.0	0.05
Epidermis	0.08	1.34	0.0	1.0	0.0	2.1e-4	20.0
Papillary Dermis	0.18	1.40	6.0	0.0	0.05	7e-5	50.0
Reticular Dermis	1.82	1.395	4.5	0.0	0.05	7e-5	70.0
Hypodermis	5.90	1.41	5.0	0.0	0.0	0.0	70.0

Table 5.1: Table of values used for the various concentrations and volumes fraction of the chromophores in the five layer skin model. Values taken from [53, 100, 180, 181].

With the absorption properties of the various chromophores in the skin defined we can now discuss the scattering properties of the skin. As the scattering properties do not vary from layer to layer by too much we use the same equation to describe the scattering coefficient [43, 53, 182].

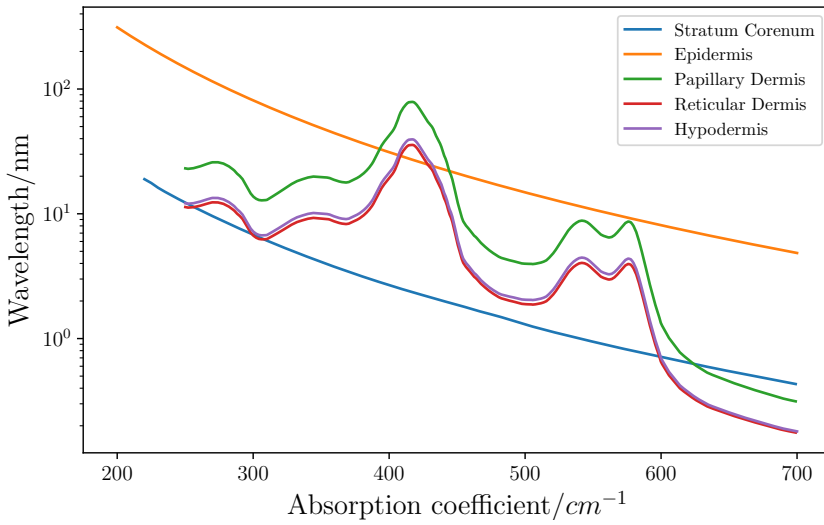


Figure 5.4: Absorption coefficients for the different layers in our skin model.

$$\mu'_s(\lambda) = a' \left(f_{ray} \left(\frac{\lambda}{500(nm)} \right)^4 + (1 - f_{ray}) \left(\frac{\lambda}{500(nm)} \right)^{-b_{mie}} \right) \quad (5.12)$$

$$\mu'_s(\lambda) = 1050.60 \times \lambda^{-0.68} \quad (5.13)$$

Where:

- μ'_s is the reduced scattering coefficient [cm^{-1}];
- a' is a scaling factor [cm^{-1}];
- f_{ray} is the fraction of Rayleigh scattering [-];
- λ is the wavelength of light [nm];
- and b_{mie} is the “scattering power” [-].

This equation mixes both Mie and Rayleigh scattering into one equation. The first term represents the Rayleigh scattering terms, whilst the second represents the Mie scattering term. Figure 5.5 shows the reduced scattering coefficients for the different layers of the skin. Table 5.2 show the values used in the model for the scattering equation for the different layers.

Layer	a'/cm^{-1}	f_{ray}	b_{mie}
Epidermis	66.7	0.29	0.69
Dermis	43.6	0.41	0.35

Table 5.2: Values of the constants for the scattering equations for the different layers of our skin model. Here epidermis represents the stratum corneum and the epidermis, and dermis represents the papillary, reticular and hypodermis in our model.

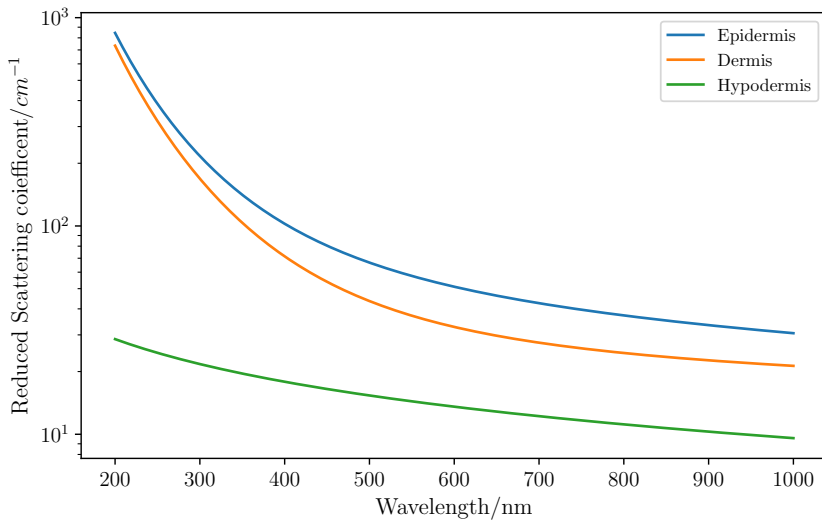


Figure 5.5: Figure shows the reduced scattering coefficient for the different layers of our skin model.

Finally we discuss the anisotropy values and refractive indices of our model.

First, the anisotropy g value is dependent on wavelength [182, 183] (See Section 2.2.2 for discussion of g values).

$$g(\lambda) = 0.62 + 0.29\lambda \times 10^{-3} \quad (5.14)$$

Where:

g is the anisotropy value [—];
 λ is the wavelength [nm].

The refractive indices of each layer is broadly the same and does not vary form layer to layer by a large amount. Table 5.3 shows the refractive indices adopted for our skin model.

Layer	Refractive index
Stratum corenum	1.5
Epidermis	1.34
Papillary dermis	1.40
Reticular dermis	1.395
Hypodermis	1.41

Table 5.3: Refractive indices used for the five layer skin model. Values are taken from [100].

As information on wavelength dependent refractive indices is not readily available, we assume that the refractive indices are the same for all wavelength used in this chapter.

5.2.2 Fluorophores in the Skin

As mentioned in the introduction there are various molecules and proteins responsible for the autofluorescent response of the skin. These include NADH (nicotinamide adenine dinucleotide), structural proteins like collagen and elastin, aromatic amino acids (tyrosine and tryptophan),

porphyrins, and FAD (flavin adenine nucleotide). Figure 5.6 shows the emission and absorption spectra for these fluorophores. As NADH and FAD are found in cells, both are typically found in all layers of the skin. Elastin and collagen are only found in the dermis [184]. Tyrosine and tryptophan are found in all layers of the skin [184].

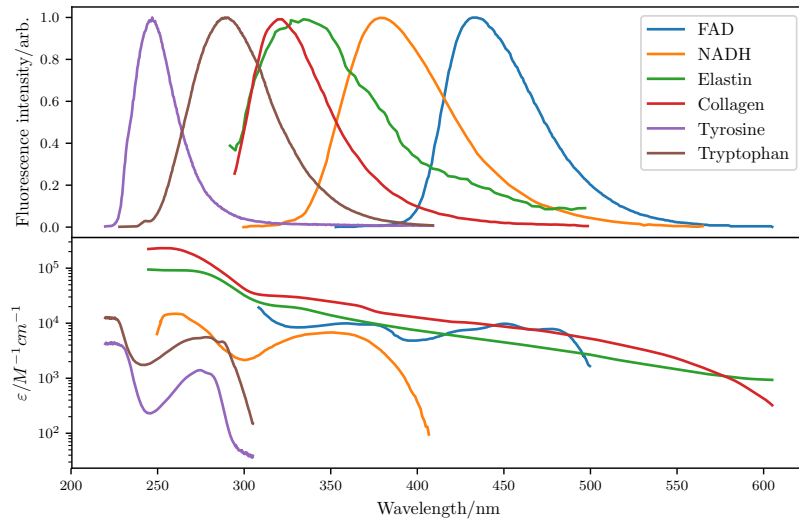


Figure 5.6: Top) Shows the fluorescent emission for the various different fluorophores. Bottom) Extinction coefficients for a selection of fluorophores found in the skin [185–192].

5.3 Modelling Fluorescence

Fluorescence is the process in which light of a certain wavelength is incident on a molecule, the molecule absorbs the light and re-emits the light at a new longer wavelength. This process can be illustrated by a Jablonski diagram. A Jablonski diagram shows the electronic states of a molecule and the possible transitions between them. This allows the illustration of various radiative and nonradiative transitions that are possible for a give molecule, including fluorescence and phosphorescence. Figure 5.7 shows an example of Jablonski diagram for a molecule that absorbs light and re-emits it as fluorescence.

To model fluorescence from multiple fluorophores requires a change of the MCRT code presented thus far. This change is to the interaction portion of the algorithm, so that it will now include the option for a packet to undergo fluorescence. To calculate whether a packet absorbs, scatters, or fluoresces, first the probability of each of these events must be calculated. Discussion of scattering and absorption (by the bulk medium) was described in Section 3.3.1. To calculate the probability of fluorescence we first assume that the quantum yield of the molecule is unity. The quantum yield of a fluorescent molecule is the ratio of photons emitted to photons absorbed. This is physically unrealistic however, it does not affect the simulations accuracy as modelling a realistic quantum yield would mean that more packets would be discarded, and thus the signal to noise ratio would be worse than if we assume a quantum yield of unity. Furthermore, information on the fluorophores, used in this work, quantum yield's is not readily available. To calculate the probability of fluorescence the absorption coefficient of the fluorescent molecule must be calculated. This is shown in Eq. (5.15):

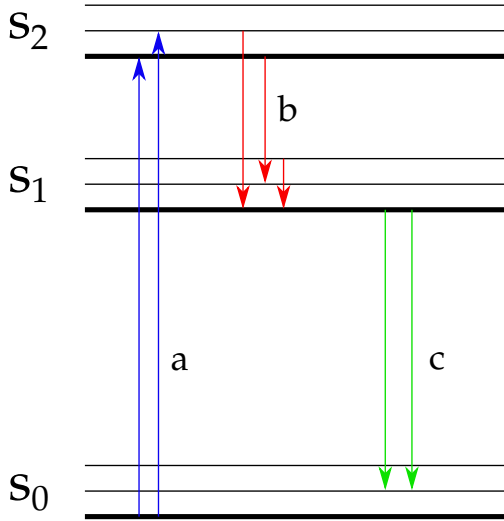


Figure 5.7: Jablonski diagram for PPIX. Bold lines indicate the lowest vibrational state of the electronic state, and thinner lines indicate higher vibrational modes of the electronic states. a) shows excitation of the ground singlet state via absorption of a photon to the second singlet state, b) non-radiative transition, and c) fluorescence.

$$\mu_f = \ln(10) \varepsilon C \quad (5.15)$$

Where C is the concentration of the fluorophore, ε is the extinction coefficient of the fluorophore, and $\ln(10)$ is the natural logarithm of 10^{\dagger} .

The next step is to calculate the total attenuation coefficient for a given species as in Eq. (5.16)

$$\mu_{t,i} = \mu_{s,i} + \mu_{a,i} + \mu_{f,i} \quad (5.16)$$

Where as usual μ_a and μ_s are the absorption and scattering coefficients, and μ_f is the fluorescence coefficient as defined in Eq. (5.15). As the absorption coefficient of fluorophores are small in comparison to the medium, and that the absorption coefficient of fluorescent molecules are generally much larger than that of their scattering coefficient, we assume that the scattering coefficient is negligible. Finally we calculate the probability of interacting with a given species using Eq. (5.17)

$$P_i = \frac{\mu_{t,i}}{\sum_{i=1}^N \mu_{t,i}} \quad (5.17)$$

Where P_i is the probability of interacting with the i^{th} species, the numerator is the attenuation coefficient for i^{th} species, and the denominator is the total attenuation coefficient for all the species.

Algorithm 1 shows the process used to determine which species to interact with.

[†]This factor appears as historically ε was measured in base 10 [43].

```

set  $\mu_{t_i}$ ;
set all  $P_i$ 's;
set  $\xi_1$ ;
if  $\xi_1 \leq P_1$  then
    set  $\xi_2$ ;
    if  $\xi_2 \leq a_m$  then
        | Scatter in medium;
    else
        | Absorb in medium;
    end
else if  $\xi_1 \leq P_1 + P_2$  then
    | Species 1 fluoresces;
else if  $\xi_1 \leq P_1 + P_2 + P_3$  then
    | Species 2 fluoresces;
else if  $\xi_1 \leq P_1 + P_2 + P_3 + \dots + P_n$  then
    | Species n fluoresces;
else
    | Error, no interaction;
end

```

Algorithm 1: An algorithm to determine which species to interact with. P_1 is the probability of interacting with the bulk medium, P_2 to P_n is the probability of interacting with a fluorescent species, a_m is the albedo of the bulk medium, ξ_i is a random number, and μ_{tot} is the total attenuation coefficient of all the species summed. The error condition should never be met.

This method allows an arbitrary number of fluorophores to be modelled. To ensure that this method works as intended, the method is compared to experimental data taken by C.L. Campbell *et al.* [182].

C.L Campbell *et al.* filled a cuvette with Intralipid 20% diluted with water, and a fluorescent agent Coproporphyrin III. The total volume of this mixture was 6 ml, consisting of 1 ml of Coproporphyrin III, 4.99 ml of water, and 0.01ml of Intralipid 20%, of which 2 ml was pipetted into the cuvette. 405 nm light was shone on a cuvette of area 10 mm × 10 mm, and collected via the same fiber, of diameter 600 μm , and NA[‡] of 0.22. The signal was recorded by an optical biopsy system (OBS). The OBS uses a 405 nm laser diode ($\sim 1 \text{ mW}$ output). The light was delivered by the aforementioned fiber, and fluorescent light was also collected by the same fiber.

The simulation is setup to mimic the experimental setup. The medium is uniform, so that only one voxel can be used which increases the speed of computation. A medium has a volume of 10 mm³. As before Intralipid is assumed to be wholly scattering with no absorption, so an albedo of 1 is used. Conversely the Coproporphyrin III is wholly absorbing with no scattering. Coproporphyrin III absorption spectrum is as shown alongside its emission spectrum in Fig. 5.8. If a photon packet leaves the top face of the simulated medium, within the radius of the fiber at an angle the fiber could accept, then the packet is recorded. The simulation is run with 10^7 photons which yielded Fig. 5.9. The algorithm presented above gave a good fit to the experimental data.

[‡]NA is the numerical aperture. The numerical aperture a measure of the range of angles that a system can accept light.

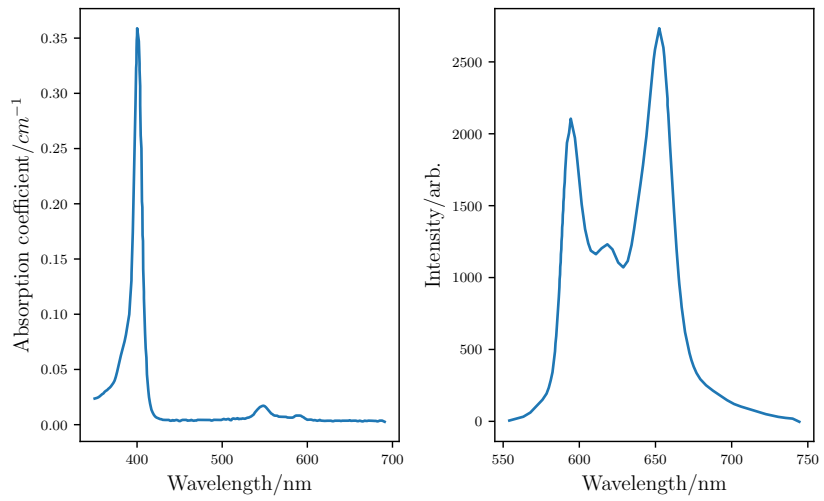


Figure 5.8: Optical properties of Coproporphyrin III. The figure on the left shows the absorption coefficient as a function of wavelength. The figure on the right shows the emission spectrum as a function of wavelength.

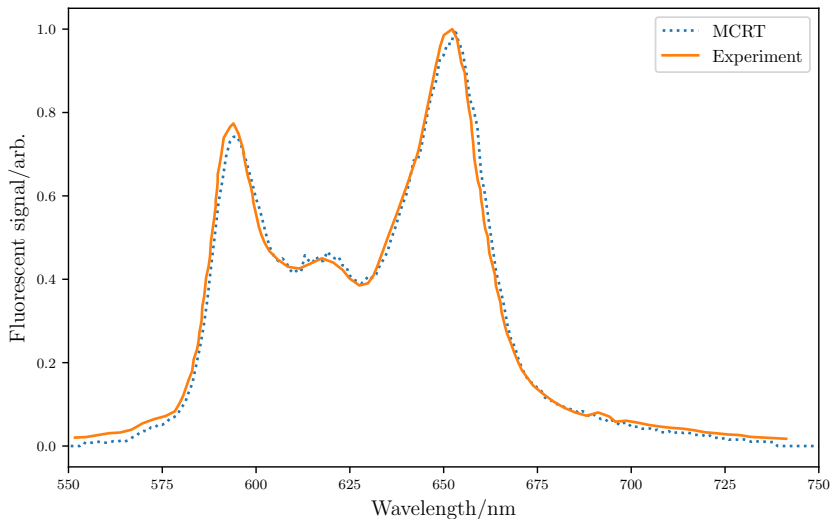


Figure 5.9: Validation of fluorescence modelling technique as described above. Figure shows that the MCRT method matches closely to the experimental results.

5.4 Nelder-Mead Method

To determine the contribution of individual fluorophores and their concentrations, emission profiles of these fluorophores cannot simply be fitted to autofluorescence signals. This is due to the nonlinear effect that tissue optics have on the emission profiles. Therefore, MCRT can be used to compute this effect. This leaves the problem as an optimisation problem. The Nelder-Mead method is an algorithm for unconstrained optimisation. The algorithm is based upon iteratively updating a simplex. A simplex is a structure in n -dimensional space, consisting of $n + 1$ points. Therefore in 1D, the simplex is a line, in 2D a triangle, in 3D a tetrahedron, etc. The Nelder-Mead method is a gradient free method, meaning that it does not require derivatives to be calculated and that the search space does not need to be smooth. This makes it ideal for problems where derivatives are not able to be computed easily, or the search space is not smooth. However, the NM method can also get stuck at local minima so care must be taken to avoid this. Genetic algorithms, which do not easily get stuck in local minima, were trialled but the computational cost of using them made it unfeasible.

The NM algorithm works by removing the worst vertex of the simplex and replacing it with a “better” vertex calculated via a number of different operations. These operations can be seen in Fig. 5.10.

The first step of the NM method is to sort the initial vertices according to their fitness. For $n = 2$, we define x_w as the “worst” point, x_l and the “lousy” point, and x_b the “best” point, such that $f(x_b) \leq f(x_l) \leq f(x_w)$, where $f(x)$ is evaluating the ‘fitness’ of a point x . The fitness function varies from problem to problem, and usually takes the form of the function that is being optimised.

With the vertices sorted, the centroid of the simplex is calculated as in Eq. (5.18). The centroid is the mean of all the vertices except the “worst” point.

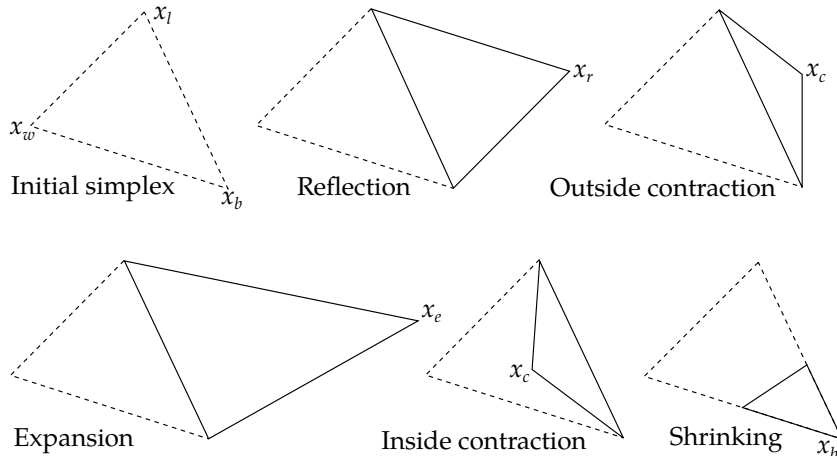


Figure 5.10: Operations that can be preformed on a simplex for $n = 2$.

The next step is to move the simplex via a reflection. To calculate the new vertex via reflection Eq. (5.19) is used, where α is the reflection factor. If this new point, x_r , is better[§] than the current “best” point then we calculate a new point in the same direction but further using the expansion operation Eq. (5.20), where γ is the expansion factor. If this new point, x_e ,

[§]Here better means the point has a lower fitness score.

is better than the “best” point then we replace x_w with x_e and start the process again. However, if x_e is not better than the “best” point, then we discard it and replace the worst point with x_r the reflected point.

If when calculating x_r , we find that it is worse than the “best” point, we then check if x_r is better than the ‘lousy’ point. If x_r is better than x_l then we replace the “worst” point and start the process again. However, if the x_r is worse than x_l , we then compare it to the “worst” point. If x_r is better than the “worst” point then we preform and inside contraction Eq. (5.22), where β is the contraction factor. If this new point, x_{ic} , is better than the “worst” point then we keep it, otherwise we preform the shrink operation, shrinking the whole simplex around the “best” point.

If x_r is not worse than the “worst” point then we preform an outside contraction Eq. (5.21). This computes a new point x_{oc} . If x_{oc} is better than x_w , then we keep it, otherwise again we shrink around the “best” point. The process described above is summarised in Fig. 5.11.

$$c = \frac{1}{n} \sum_{i=1, i \neq w}^{n+1} x_i \quad (5.18)$$

$$x_r = c + \alpha(c - x_w) \quad (5.19)$$

$$x_e = c + \gamma(x_r - c) \quad (5.20)$$

$$x_{oc} = c + \beta(x_r - c) \quad (5.21)$$

$$x_{ic} = c + \beta(x_w - c) \quad (5.22)$$

Standard values for the factors are: $\alpha = 1$, $\beta = \frac{1}{2}$, $\gamma = 2$, and $\delta = 0.5$. Though in practice these values are adjusted for the problem at hand. For higher dimensions, i.e. where $n > 2$ F. Gao *et al.* suggest that the parameters should be changed based upon how many dimensions are used for the simplex [193]. The values F. Gao *et al.* suggest are: $\alpha = 1$, $\beta = 1 + \frac{2}{n}$, $\gamma = 0.75 - \frac{1}{2n}$, and $\delta = 1 - \frac{1}{n}$. Where n is the order of dimensions. Therefore, we adopt F. Gao *et al.* values for $n > 2$ and the “standard” values for n less than equal to 2.

As the Nelder-Mead method has no inbuilt convergence criteria, this must be added. We use two different criteria based upon simplex size, and vertex fitness. The size of the simplex is calculated using Eq. (5.23):

$$\text{size} = \sum_{i=1}^{n+1} |p_i - p_{i+1}| \quad (5.23)$$

Where p_i and p_{i+1} are vertices in the simplex that are connected by an edge. If the size of the simplex falls below a pre-set value, then we preform a factorial test to see if the simplex should be restarted or if the algorithm should terminate. The factorial test checks the space around the current simplex to ensure that we have converged to a global minima. If the check fails then the algorithm is restarted with the current best point kept, and new vertices generated.

The other convergence criteria is a check to see if the best point is “good enough”. The current best point is compared to a pre-set fitness value. If the best point is better than the pre-set value then the algorithm terminates.

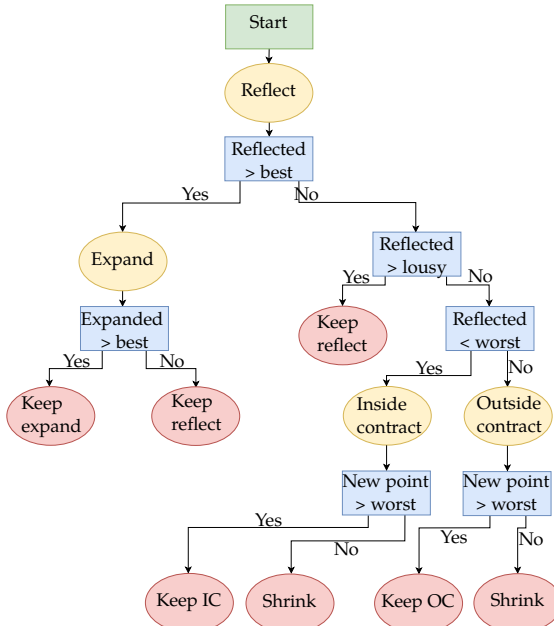


Figure 5.11: Nelder-Mead decision tree. Here $>$ means better, and $<$ worse. Best, lousy, and worst have the same meanings as in the main text.

5.5 Validation

The NM method was coded in modern Fortran, so that it could be easily interfaced with the MCRT code developed as part of this thesis. To test that the NM method works as intended a number of trial optimisation functions were tested, see Table 5.4. This was achieved by selecting an initial simplex, and the method allowed to iterate until it converged. The results of this are shown in Fig. 5.12.

Name	Formula	Global Minimum
Sphere	$x^2 + y^2$	$f(0, 0) = 0.$
Rosenbrock	$(a - x)^2 + b(y - x^2)^2$	$f(1, 1) = 0.$
Ackely	$-20 \exp \left[-0.2 \sqrt{0.5(x^2 + y^2)} \right] - \exp [0.5(\cos 2\pi x + \cos 2\pi y)] + e + 20$	$f(0, 0) = 0.$
Himmelblau's	$(x^2 + y - 11)^2 + (x + y^2 - 7)^2$	$f(3, 2) = 0.,$ $f(-2.805118, 3.131312) = 0.,$ $f(-3.779310, -3.283186) = 0.,$ $f(3.584428, -1.848126) = 0.$

Table 5.4: Table of standard test functions for numerical optimisation.

Some of these functions (Sphere, and Rosenbrock's) can also be extended to arbitrary dimensions. These functions were used to check that the NM method works as intended in these higher dimensions where the NM method will primarily be used in this thesis.

To ensure that the NM method can be used to find the unknown concentrations of the autofluophores, we test the method with two different toy models. The first model is a “2D”

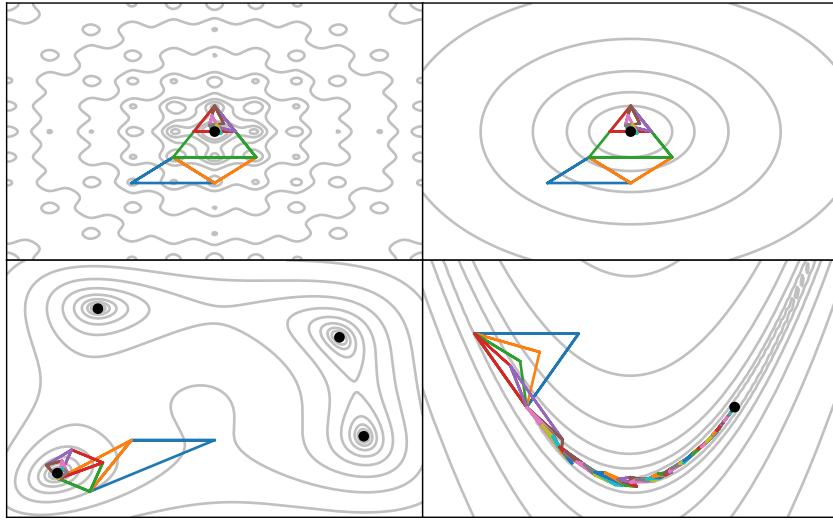


Figure 5.12: Contour plots of test functions with Nelder-Mead simplexes over plotted. Top left is the Ackley function, top right is the sphere function, bottom left is the Himmelblau's function, and the bottom right is the Rosenbrock function. Grey lines are contours, coloured lines are the simplices with the blue simplex being the initial simplex. Finally, the black dots represent the global minima for that function.

model, with two different fluorophores evenly distributed over all 5 layers of our skin model, i.e $n = 2$. The two different fluorophores are NADH, and a fictitious fluorophore that has similar properties to FAD and tryptophan, such that the excitation spectrum is that of FAD and the emission spectrum is that of tryptophan. The concentration in these layers is such that the bulk optical properties are not affected: NADH has a concentration of $1.0 \mu M$, and the fictitious fluorophore has a concentration of $2.5 \mu M$. To generate a spectrum to which the NM method can compare to, the MCRT code is run with the above configuration of fluorophores. This generated Fig. 5.13.

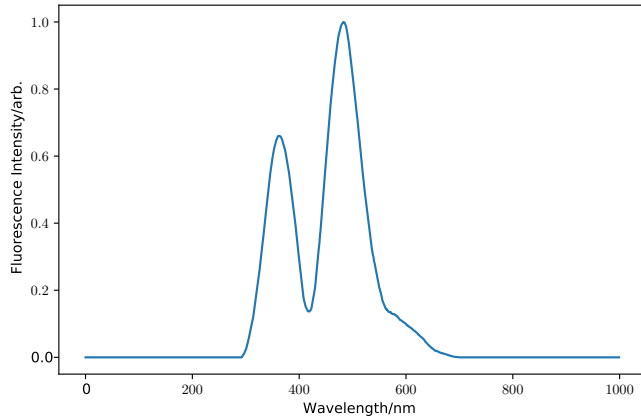


Figure 5.13: Example of toy model spectrum for testing NM method. The two peaks correspond to the fictitious fluorophore, and NADH.

The fitness function chosen to check whether the NM method is converging to the generated spectrum is as:

$$fitness = \sum_{i=1}^n (x_i - m_i)^2 \quad (5.24)$$

Where x_i is a data point at a wavelength λ_i produced by the MCRT, and m_i is a data point in the model at a wavelength λ_i .

As the NM can get stuck in local minima, we run the method for several different initial simplices to ensure that this does not occur. As the MCRT code is called multiple times per simplex iteration, and the fluorophore concentration is low meaning that many packets need to be run to achieve a good signal to noise ratio. These two conditions result in a computational load that is infeasible to run. Therefore the MCRT algorithm has to be computationally efficient in order to arrive at an answer within a reasonable time. As the optical properties only vary in the z direction, the voxel model is shrunk to $1 \times 1 \times 500$, with 500 voxels representing the z direction. To this end the 3D skin model is shrunk to a 1D model in the z direction so that the optical integration routine can efficiently move the packet through the simulated medium. The optical properties of the incident wavelength are also stored so that when a new packet is started the optical properties can easily be adjusted without need for any calculation. Finally a filter is employed on the output fluorescence spectrum to smooth the noise out.

The filter used is a Savitzky-Golay filter. This filter fits multiple low-degree polynomials to subsets of the data, thus smoothing the data [194]. Equation (5.25) shows the functional form of the Savitzky-Golay filter, where for a data set consisting of n (x_j, y_j) points, and C_i are the set of m convolution coefficients. m is the “window” of data the polynomial of order k if fitted to via the linear least squares method.

$$Y_j = \sum_{i=\frac{1-m}{2}}^{\frac{m-1}{2}} C_i y_{j+1} \quad (5.25)$$

Figure 5.14 shows the use of the Savitzky-Golay filter on sample output data from the MCRT simulation.

Using the above set-up with the Savitzky-Golay filter on the output spectrum, allowed the NM method to efficiently run many models of various different concentrations and “find” a set of concentrations that resulted in a close match with the target spectrum. However, as the detected fluorescence spectra are normalised to their peak values we cannot use this method to determine the original concentration, but rather the ratio between the two concentrations. Figure 5.15 shows the search space and the spread of the concentration values calculated by the NM method compared to the original target concentrations. The spread of the concentrations calculated by the NM method follow a linear relationship as would be expected. Therefore, a line of best fit was fitted to the concentrations. This yielded a line ($y = m x$) with $m = 2.49 \pm 0.05$. The expected relation between the concentration is where $m = 2.5$ therefore, the NM method can be used to determine the relative difference in concentrations within one standard deviation.

The NM method was also tested on a toy model for $n = 3$. Here the fluorophores used were: NADH, FAD, and a fictitious fluorophore with the absorption properties of NADH and the emission properties of Tyrosine. The fluorophores had concentrations of $1.05\mu M$ $525\mu M$, and $125\mu M$ respectively. The set-up is the same for the above $n = 2$ case, with the same filter and computational speed ups used. Figure 5.16 shows various concentrations as calculated by the NM method compared to the original concentration. Again a line of best fit was fitted to

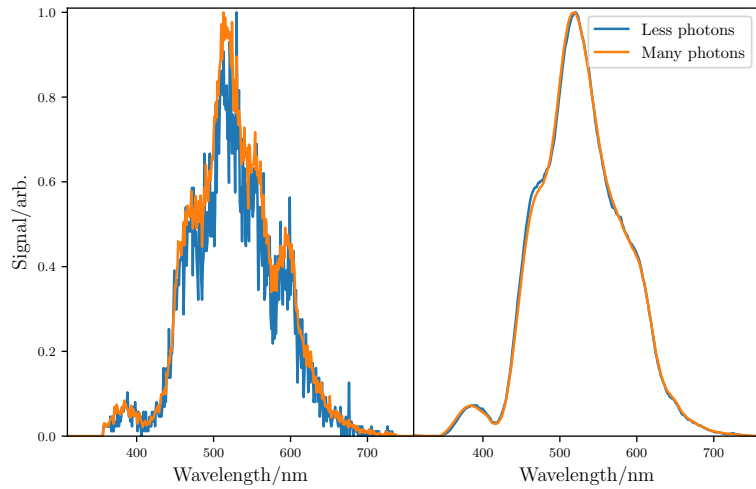


Figure 5.14: Illustration of how the Savitzky-Golay filter works on noisy data and recovers the roughly the same signal on the same data set with less noise. Left image shows the raw signals from the simulations with a packets difference of 10^{-3} . Right image shows the data set after the Savitzky-Golay filter is applied. A window size of 101, and polynomial of order 2 were used as the filter settings.

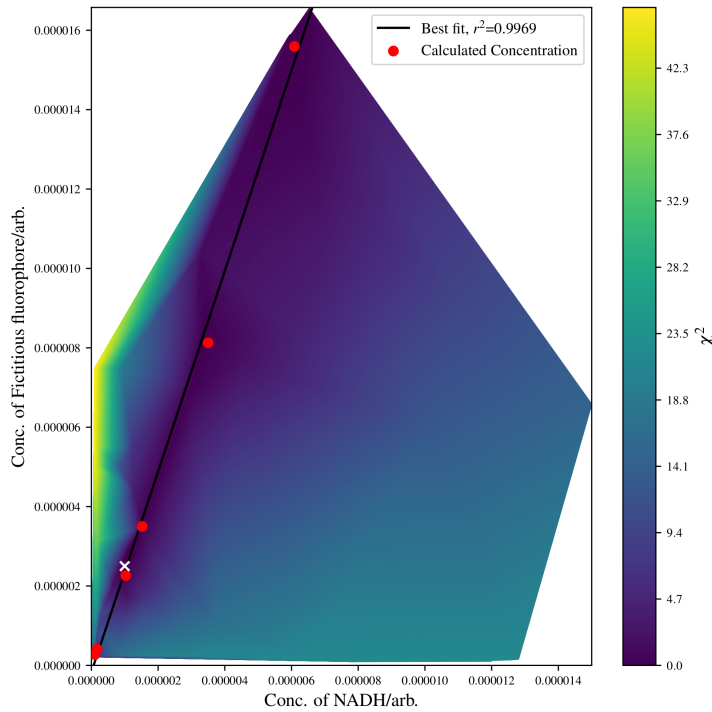


Figure 5.15: Figure shows the search space for the 2D toy problem outlined above. A line of best fit is fitted to the concentrations found by the NM method. Note also the valley of good fit where the line of best fit lies. The search space is also fairly smooth.

the calculated points [¶]. As there is no closed form solution for the equation of a line in $n > 2$ dimensions, the equation of a line in 3D can be represented by Eq. (5.26):

$$\vec{r} = \vec{r}_0 + t \vec{v} \quad (5.26)$$

Where \vec{r} and \vec{r}_0 are position vectors for P and P_0 respectively, \vec{v} is a vector parallel to the line we are examining, and t is some real number. This equation also holds for an arbitrary number of dimensions. The line of best fit yielded $\vec{v} = [0.0013, 0.9858, 0.1682]$. Where as the “real” \vec{v} is equal to $[0.0019, 0.9728, 0.2316]$. This again shows that the NM method can be used to find the relative concentrations of the fluorophores in the skin, even in dimensions higher than 2.

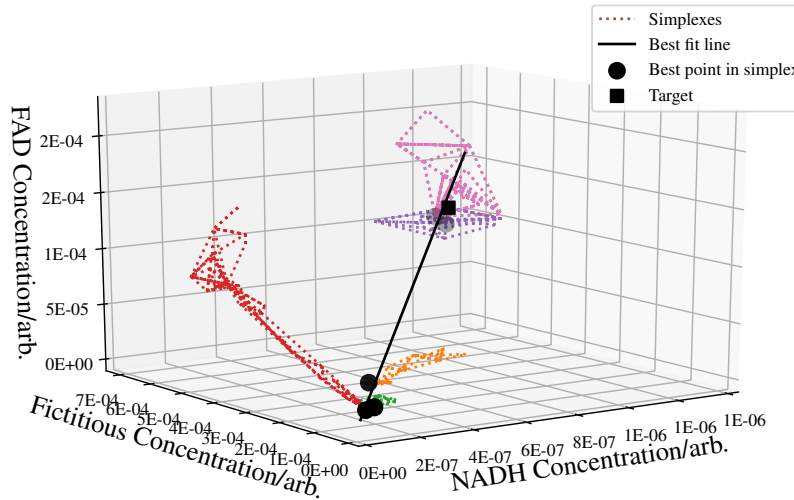


Figure 5.16: Figure shows the line of best fit for the case where $n = 3$. Figure also shows the simplices path over their whole lifetime, from initial guess to final simplex.

5.6 Results

5.6.1 Experimental Work

Experimental work discussed in this section was carried out by my collaborators S. Smirni *et al.* at the University of Dundee and Ninewells Hospital.

S. Smirni *et al.* took autofluorescence spectra from the volar forearms of volunteers using the LAKK-M multi-functional laser non-invasive diagnostic system (MLNDS). The LAKK-M system combines laser-Doppler flowmetry, tissue reflectance oximetry, pulse oximetry, and laser fluorescent diagnostics in one machine. The LAKK-M system delivers and collects light via the same optical fiber package. The fiber package has seven optical fibers, one for each probing wavelength (365 nm, 430 nm, 532 nm, 635 nm), two detectors, and a spectrometer. The fibers radii are 0.4 mm, and the separation between the fibers is around 1 mm. S. Smirni *et al.* took autofluorescence spectra from volunteers as they underwent a post occlusive reactive hyperemia

[¶]The line of best fit was calculated using the singular value decomposition (SVD) method of solving the least squares.

(PORH) test. A PORH test is used to investigate and assess microvascular function. It achieves this by usually inflating a cuff on an arm of a patient for a period of time and then letting it deflate. Whilst this is happening laser Doppler flowmetry is used to asses the flow of blood before inflation, during inflation and after inflation. How the micro-vascular system responds to this test can be indicative of various CVDs. Figure 5.17 shows an example of the data collected during a PORH test.

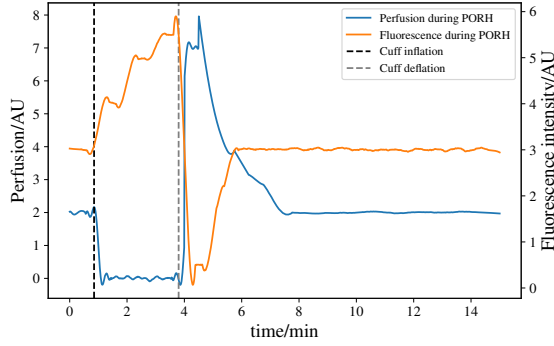


Figure 5.17: Example of a PORH test whilst measuring autofluorescence and perfusion. The perfusion of blood in the skin decreases once the cuff is inflated, and then rapidly reaches a maximum once the cuff is removed. The inverse of this can be seen in the autofluorescent response of NADH in the tissue.

S. Smirni collected around 27 spectra at the rate of 1 per minute over a period of 27 minutes as the PORH test was undertaken, 11 for a baseline before inflation of the cuff, 5 during occlusion and 11 post occlusion. Spectra were taken at each of the possible wavelengths (635 nm, 532 nm, and 365 nm) that the LAKK-M provides, yielding a total of 81 autofluorescence spectra per volunteer. S. Smirni also collected laser Doppler flowmetry data during this period, however as this work only concerns the modelling of autofluorescence, we restrict the analysis to that of the UV (365 nm) autofluorescence spectra. Figure 5.18 shows an example of a raw spectrum taken during the baseline portion of the experiment.

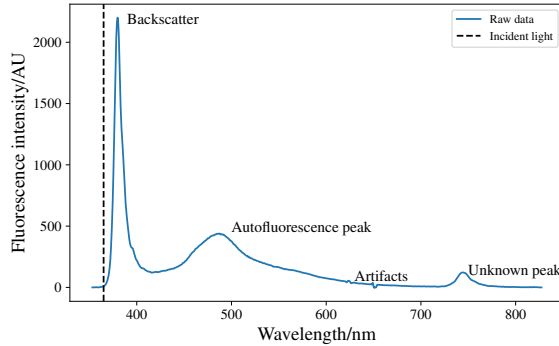


Figure 5.18: Figure shows an example of a raw spectrum taken by S. Smirni et al.. This figure illustrates how the spectrum is red-shifted, along with some of the artifacts, backscatter, and autofluorescence peaks. There is also a third peak in the red end of the spectrum. The cause of this is unknown, but most likely due to an unidentified fluorophore.

5.6.2 Effect of Tissue Optics on Fluorescent Signal

As mentioned in the introduction to this chapter information about how tissue optics affects the fluorescent signal, which fluorophores contribute to the signal, the variability of the signal in different test sites, and location of the fluorescent signal are not well elucidated. Therefore, before running the NM method on the experimental data, we analyse these various unknowns. We also present results on how the excitation wavelength affects the signal.

Figure 5.19 shows the fluence as a function of depth for the incident UV light. The figure shows that most of the incident light is contained within the top three layers, with little getting to the Reticular dermis, with none reaching the Hypodermis. The fluence drops to 50% of its peak value 0.026 cm into the tissue which equates to inside epidermis, and 10% of its peak value by 0.058 cm into the tissue which again is in the epidermis.

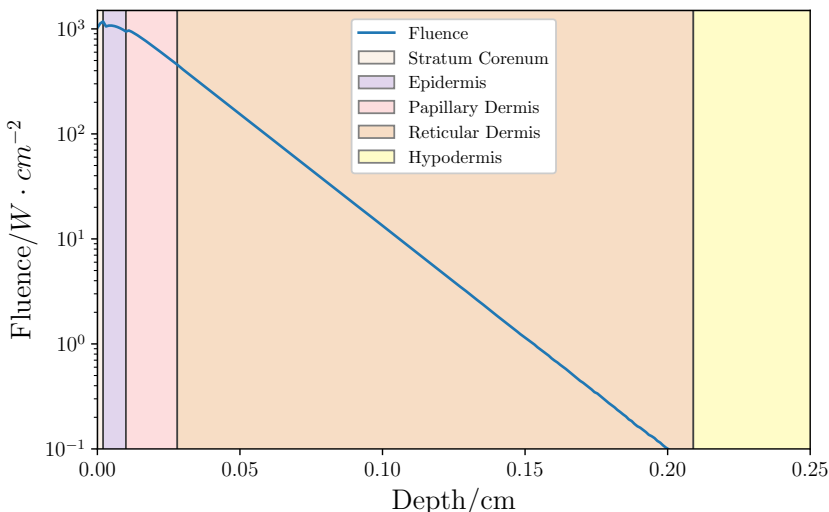


Figure 5.19: Penetration of UV radiation as a function of depth.

Figure 5.20 shows the fluence^{||} of detected fluorescent light (see Appendix B for discussion of how this is tracked). The figure shows the fluence of light for each fluorophore that is detected. The figure shows that the fluence is highest in the Papillary dermis and a number of peaks at the boundaries of the layers. First the refractive indices of the layers are different, this can lead to light getting “trapped” in a layer as it can be internally reflected off the layer boundary, thus leading to increased fluence. Second, fluorescent light is emitted isotropically which means that fluorescent light emitted in the upper layers of the skin, may be emitted in the direction of the Papillary dermis, that and light emitted from below the papillary dermis has to travel though the papillary dermis in order to be detected. Finally the optical properties also have an effect on the detected light fluence. The dermal layers have a minimum in their absorption spectra at the range of wavelengths that NADH and FAD emit at, thus light is more likely to “survive” though the dermal layers than the other layers such as the epidermis. Finally the geometry of the layers most likely has an effect as well. The stratum corneum’s and the epidermis’s thickness is small in comparison to that of the dermal layers, thus there will be less fluorescent light emitted from these layers when the concentration are the same.

^{||}Though this is not real fluence, as all photons would contribute to the overall fluence. An accurate name for this quantity would be the contribution to the fluence by the detected fluorescence of a fluorophore.

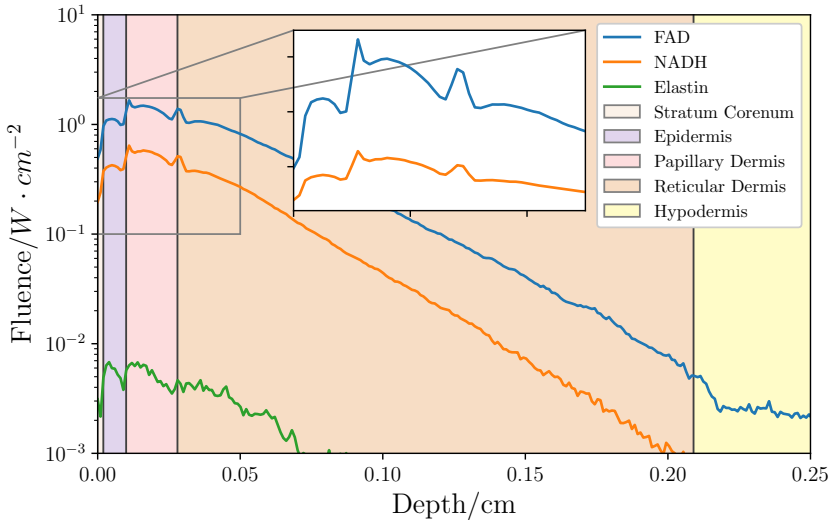


Figure 5.20: Detected “fluence” for FAD, NADH, and elastin fluorescence. Inset shows zoom in of top layers of the skin, note the inset is a linear scale.

Figure 5.21 shows the location of where the fluorescent light is emitted from. For both NADH, and FAD their peaks depth is just inside the epidermis. However, the vast majority of emitted Fluorescent light originates in the papillary dermis. This occurs as enough light gets to this layer, which allows more light to undergo fluorescence.

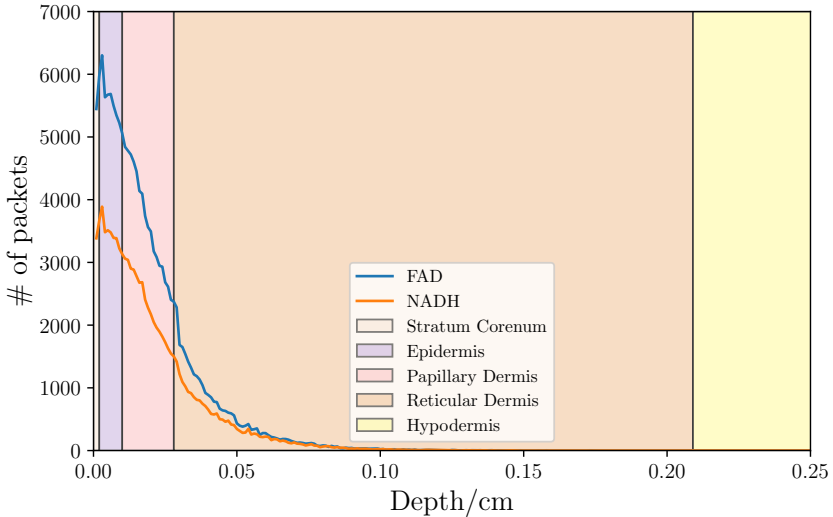


Figure 5.21: Amount of packets escaping as a function of depth for FAD and NADH fluorescence.

Finally, we analyse the effect excitation wavelength has on the detected signal of NADH and FAD. To achieve this we run several models in order to create an excitation emission matrix (EEM). A EEM is a way of investigating and displaying the effect excitation wavelength has on the fluorescent output of a sample. Using the same setup as above, we vary the fluorophore

concentration in each layer, such that only one layer at a time has any fluorophores in it. We then excite the model over a range of wavelengths. For NADH we use wavelengths in the range of 250 to 400 nm, and for FAD we use 250 to 500 nm. Figures 5.23 and 5.24 show the EEM for NADH and FAD. The EEM for NADH shows that the strongest signal comes from the papillary dermis when compared to other layers. The EEM also shows a maximum of emission for excitation wavelengths corresponding to around 260 nm and 320–380 nm. For FAD the layer that yields the most fluorescence is the reticular dermis. The EEM shows that for excitation wavelengths of around the range 450–500 nm gives the most fluorescence.

For the case of NADH the optimal excitation wavelengths coincide with maxima in the absorption spectrum of NADH (see Fig. 5.22). However, for FAD the maximum in fluorescence does not coincide with the largest maxima in its absorption spectrum (see Fig. 5.22), but rather it falls within a smaller maximum. This is because that light at the maximal absorption peak (~ 300 nm) is highly absorbed by tissue, especially in layers such as the epidermis. Therefore, light at a longer wavelength is more likely to escape the tissue due to the tissue optical properties.

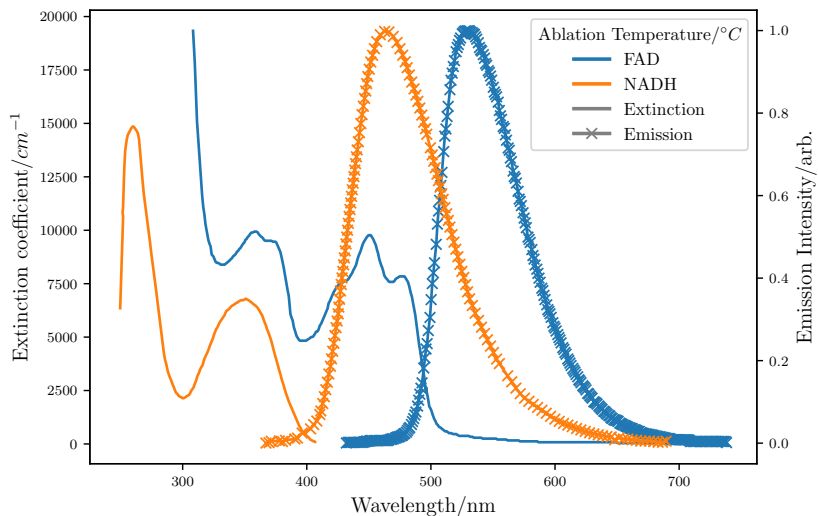


Figure 5.22: NADH and FAD absorption and emission spectra.

5.6.3 Using the NM Method

We model the experimental setup by S. Smirni *et al.* as described in a previous section. The computational speed ups described in the validation sections are also used. The 5 layers skin model is setup with NADH, FAD and collagen distributed in different layers. NADH and FAD are initially in all layers except the hypodermis, and collagen is contained in just the papillary and reticular dermis**. Each layer has its own concentration of the fluorophores giving n for the NM method of 10. An initial guess of the concentration of the fluorophores is made, and the NM method is allowed to run until it stagnates. The target spectrum for the NM is taken from S. Smirni experimental data. Before the target spectrum could be used it was first “cleaned up”. This “cleaning” process was required as the spectrum was shifted by 20 nm into larger wavelengths. The cause of this systematic shift is unknown. As a backscatter peak is included

**We omit any fluorophores form the hypodermis as they are not expected to contribute to the signal at all, or by much. This also simplifies the problem from $n=13$ to $n=10$.

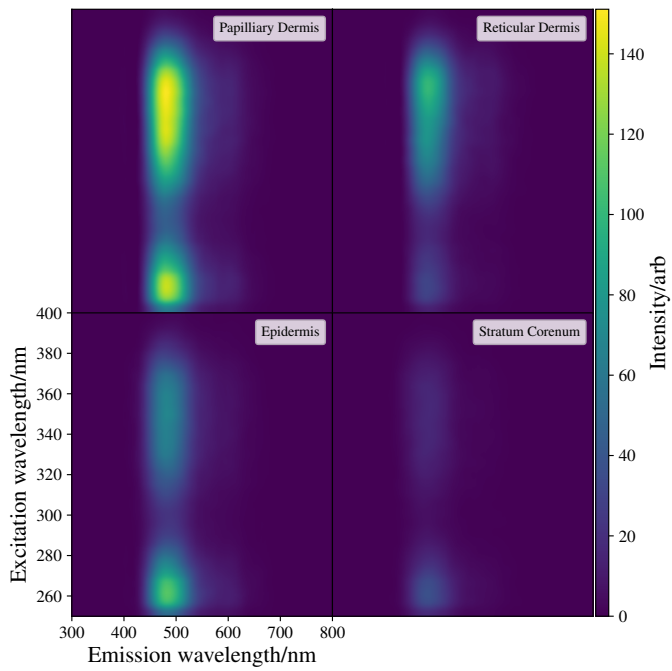


Figure 5.23: Excitation-emission matrix for NADH. Figure shows that the fluorescent signal from NADH is strongest in the papillary dermis.

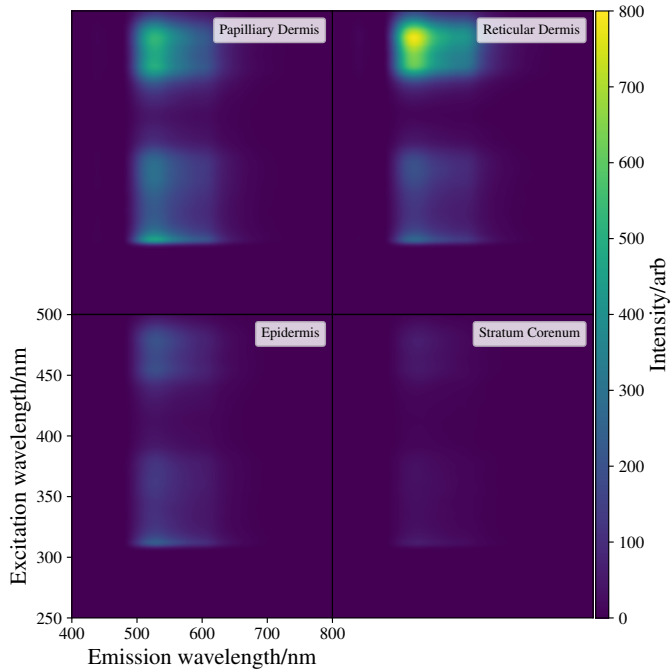


Figure 5.24: Excitation-emission matrix for FAD. Figure shows that the fluorescent signal from FAD is strongest in the reticular dermis.

within the spectrum, the spectrum can be moved to its correct position. The next step in the “cleaning” process is to filter out spectra that are “defective”. Several of the autofluorescence spectra have artificial peaks caused by various experimental errors or machine faults. The final stage of the “cleaning” process, is to smooth the data out and remove the backscatter peak. Now the spectra can be used as a target spectrum for the NM method.

Figure 5.25 shows the output of the NM method during a run with the above parameters. The figure shows that as the simplex iterates, the average fitness improves, the average number of calls to the MCRT algorithm tends to ~ 1.4 . This suggests that the NM keeps the reflected point more often than not. The size of the simplex fluctuates as the simplex tries to find the global minima. This happens as the simplex moves over the search space it sometimes needs to grow in size, then when it finds a minimum it shrinks around it. The size of the simplex will then grow when the algorithm is restarted.

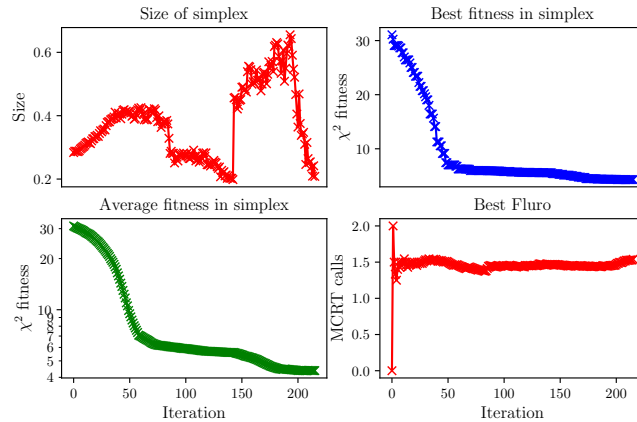


Figure 5.25: Figure shows the diagnostic information output by the NM method. Top left) shows the size of the simplex as it evolves. Top right) shows the best point in the simplex as it evolves. Bottom left) shows the average fitness of the simplex. Bottom right) shows the number of calls to the MCRT code per iteration of the simplex. The more call to the MCRT the simplex requires, the longer the runtime.

Figure 5.26 shows the output of the NM. The “best” fitness achieved by the algorithm was ~ 3 , which is a fairly poor fit when compared to the validation examples above. The figure also shows the contribution of the individual fluorophores to the overall autofluorescence signal. As expected the main contribution is from NADH, with a little contribution by FAD. However, collagen contributes to the main peak and is multi-peaked, with peaks at ~ 380 nm and ~ 465 nm. This is unusual as the peak of emission for collagen used in this work is around 395 nm, therefore it was not expected to contribute to the signal around the NADH peak. The reason that the collagen signal is multi-peaked is due to the tissue optics. There is a large peak at around 400–410 nm in the absorption spectra in the dermal layers. This causes a dip in the emission of collagen, giving it the multi-peaked profile.

5.7 Discussion

There are several probable reasons why the spectrum generated by the MCRT and NM does not match the experimental data exactly. A first possible reason for the mismatch, is that the optical properties of the fluorophores are not accurately known. Optical properties of the

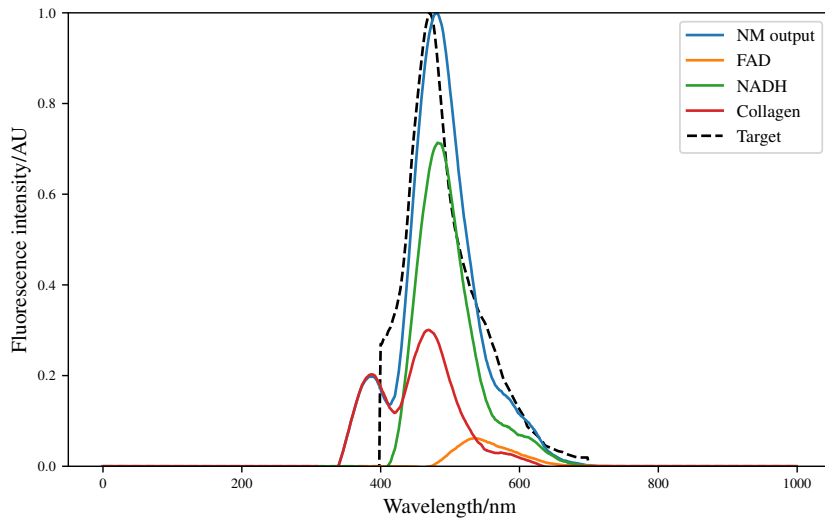


Figure 5.26: Figure shows the best result from the NM operating on the experimental data from S. Smirni et al.. The spectrum has a fitness of ~ 3 . The figure also shows the makeup of the final spectrum by the individual fluorophores.

fluorophores used in the work are not readily available. There are various sources that have measured them, but they are usually confined to several wavelengths of the authors interest and not a full spectrum. The extinction coefficients for the fluorophores are measured in various buffer solutions, and not taken from *in-vivo* tissue. This could give rise to a discrepancy between the computed results and the experimental results. The emission spectra for the fluorophores could also be incorrect. Eission spectra used in this work are also measured in various buffer solutions, which again may be different from what they are *in-vivo*. Finally the emission spectra are measured for a single excitation wavelength. As the spectra were not readily available for the excitation wavelength used in this work, the emission spectra were taken from the nearest possible excitation wavelength found in the literature. This again may introduce a difference from the experimental work. However, what optical properties that have been published are pretty consistent from author to author therefore, this is an unlikely problem.

The mismatch in the target spectrum and the calculated spectrum could be due to missing fluorophores. The model presented here only included NADH, FAD, and collagen which are thought to be the three main contributers to the autofluorescence signal. However, the inclusion of riboflavin (peak at 529 nm), β -carotene (395 nm), elastin (425 nm), and different types of collagen (420, 370, 395 nm) may be able to correct this.

A final possible reason for the mismatch is that the LAKK-M device creators seem to have mis-calibrated their machines for finding the peaks of various fluorophores. Table 5.5 shows a comparison between the literature and the values used by the LAKK-M team.

For whatever reason, they seem to be consistently off by around 25 to 30 nm. From this chapter's work on how tissue optics affects the fluorescent signal, tissue optics cannot account for the discrepancy. One possible cause for this is that the UV light they use to probe autofluorescence is an LED. LED light sources are not monochromatic, but rather have a range of wavelengths they emit, on the order of 25 nm FWHM. Therefore, they could be exciting with a different range of wavelengths, which could possibly contribute towards the difference in what they measure and the literature values.

Fluorophore	LAKK-M peak/nm	Literature peak/nm
FAD	550	525
NADH	490	465
Elastin	450	425
Collagen	420	370(IV), 395(I,V), 600(VII)

Table 5.5: Comparison of LAKK-M emission peaks and that found in the literature. AS there are different types of collagen multiple types were included in the literature comparison. LAKK-M data from [195–198]. Literature values taken from [189, 192, 199, 200].

5.8 Conclusion

In conclusion, this section has introduced a five layer skin model, that has the ability to vary the various constituent parts to tailor a model for a generic or specific patient. We have also shown in this chapter a method of coupling an optimisation technique to MCRT. This was done in order to investigate the concentrations of naturally occurring fluorophores in the skin. Differing levels of the fluorophores can indicate various diseases such as diabetes and CVDs. We validated this technique against a toy model in various dimensions, with good agreement. Before experimental data was analysed, the effect of tissue optics on the autofluorescent signal was tested. We then used our numerical model on experimental data. We found good, but not excellent agreement with the data. A discussion of why our model does not fit the experimental data, with several possible reasons presented. Future work would involve taking known “good” data that would be worthwhile to validate against. Finally, if the model can be validated against this data the model could be used in future to explore the relationship between various diseases and autofluorescence.

Chapter 6

Conclusion

6.1 Summary

To summarise this thesis, MCRT is a powerful technique that can be used to calculate the transport of light (as particles or quasi-wave/particles) through turbid media, whilst modelling multiple anisotropic scattering alongside a variety of microphysics. The only noted downsides to the MCRT method noted in the literature (as well as discussed at length in this thesis) is the computational load required for some problems and the optical properties. With the growing computational power year on year, more and more the computational load of MCRT becomes less of a factor. Likewise the optical properties of various biological tissues, are increasing being measured with greater precision and accuracy.

Chapter 1 introduced the concept at the heart of this thesis, the Monte Carlo method. The chapter gave examples of how the Monte Carlo method can be used to sample from spectra, and how it is used to model various physical events. Chapter 2 followed on from chapter 1 explanation of the Monte Carlo method, by introducing MCRT used in all subsequent chapters. Chapter 2 covered the theory behind the method and presented details of the implementation into code alongside various computational speedups.

Chapter 3 described the application of the MCRT method to modelling tissue ablation. Details of how the MCRT was coupled up to a numerical model of heat diffusion and thermal damage model was presented. The chapter showed that we can successfully model experimental and theoretical data with our numerical model. The power the model has is that we can predict thermal damage, and ablation crater size for any laser, and configuration thereof, without the need to test on humans or animals. It also allows the testing of different lasers without the purchase of said laser, which could allow clinicians to “try before they buy”. The chapter also presented (with tongue firmly in cheek) the application of this numerical model to humane spy disposal.

Chapter 4 presented the modification of the MCRT method, such that it would allow the modelling of the photon packets as quasi-wave/particle packets, in place of the usual particle model MCRT models. This was achieved via a few small changes within the code, based upon well understood theoretical models, namely the Fresnel-Huygens principle. The method was thoroughly validated against several theoretical expressions. The method was validated against experimental results from collaborators at the University of Dundee. The new method was then used to compare Bessel and Gaussian beams performance in highly turbid media. The method showed that blah

Chapter 5 presented a model of skin autofluorescence using MCRT. The chapter detailed a five layer skin model created to accurately model the skin effect on light transport. The five layer model included the various chromophores found in the skin such as blood, water, and melanin. The model also includes various naturally occurring fluorophores. Changes in the autofluorescent response of tissue has been shown to be indicative of various diseases. Therefore the MCRT algorithm was coupled to an optimisation technique to determine relative concentrations of the fluorophores in the skin. The technique chose was the Nelder-Mead method. The NM method uses simplices in order to move around the search space and find global minima. The method was coupled to the the MCRT algorithm and thoroughly validated against toy models. Finally details of how autofluorescent data from collaborators was fitted using these techniques.

6.2 Future Prospects

There are several avenues of promising work that can continue on from this thesis.

The code developed as part of the tissue ablation chapter, could easily be adapted for use in modelling photothermal therapy. Photothermal therapy is the use of light to selectively heat up nanoscale materials that have been inserted into tumours. The nanoscale materials, such as gold nanorods, are targeted with a specific wavelength of light (usually near infra-red) which heats up the rods and thus the surrounding tissue, eventually killing the adjacent cells [201, 202]. This could be easily modelled within the code developed as part of chapter 3, with little to no major changes. The code could be used to help optimise photothermal treatment modalities and predict treatment outcomes.

There is also scope to improve the heat transfer model. As mentioned in the chapter, a simple explicit model was used as it relatively easy to setup and solve a given problem using this scheme. However, this scheme leads to constraint on the timestep. This could be avoided by using an implicit scheme which is unconditionally stable for any timestep. Another way the heat transfer model could be improved is thought the use of the finite element method (FEM). The FEM allows PDEs to be solved on arbitrary grids, which would reduce the high memory requirement our model needs to achieve good resolution. The FEM would also allow a more accurate skin model to be included within the simulation, making the simulation more accurate.

Finally, the work of chapter 3 could also be extended to include a drug diffusion model. One use of tissue ablation is a an optical drill to create micro holes in the skin. These holes in the skin then allow better penetration of topical drugs. Modelling both the laser tissue ablation process and drug diffusion process in one simulation would allow *in-silico* testing of treatment parameters which could easily be optimised by the model.

The algorithm developed as part of chapter 4's work, φ MC, also has several avenues of future research. It should be fairly easy to extend the algorithm to model other beams, such as an Airy beam. It should also be fairly trivial to implement a spatial light modulator (SLM). An SLM is a device that can modulate light that is incident on it including imparting phase to different parts of the incident beam. This allows arbitrary complex beams to be created. The ability to model an SLM would open up the ability to model complex experiments in such things as wavefront shaping. Other types of experiments the algorithm could be used for include: laser speckle imaging, focusing light though turbid media, and complex micromanipulation [203–205].

One obvious avenue of future research would be to improve the five layer skin model presented as part of chapter 5's work. The skin model presented is planar, where as tissue is not planar in any sense. The first improvement on this could be to introduce a more complex geometrical structure into the voxel model. However, this method would quickly run into a computational wall. To represent the non planar reality if the tissue would require many voxels, such that the

RAM required to run any simulation would be prohibitive to running the simulations. Therefore, a different geometrical model would need to be used. A solution to this was briefly investigated: use of a mesh to model the skin's structure. Triangular meshes can be used to model any arbitrary shape or volume [cite]. The use of triangular meshes have been used to great effect by other authors in MCRT codes. Due to time constraints this was abandoned for this thesis before a fully working code could be developed. Figure 6.1 shows MCRT being preformed on a gourd, made from a triangular mesh.

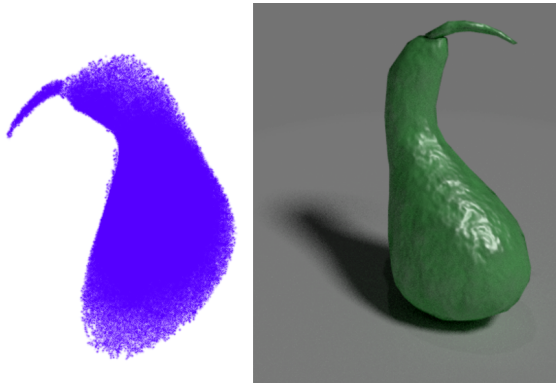


Figure 6.1: Image on the left shows the fluence of light in a gourd, calculated using MCRT. The optical properties of the gourd in this simulations are similar to that of skin. The optical properties of the medium around the gourd are that of air. Image on the right shows a rendering of the same mesh in blender.

A meshed skin model would allow objects like hairs, blood vessels, sweat glands, and the uneven boundaries greatly increasing the accuracy of the simulations.

As the data from our collaborators machine was not of a quality such that it could be reproduced using amoebaMCRT, this data could be taken again with a better machine, or other authors could be found that have the requisite data. amoebaMCRT would then be run on this data to determine the amount of that each fluorophore contributes to the signal. Other optimisation techniques other than the NM method could be explored. Techniques such as simulated annealing, genetic algorithms* or machine learning could be used. It could also be possible for our MCRT code to be used to create a “bank” of spectra that could then be used to train a machine learning algorithm to label peaks, and contributions to those peaks by fluorophores.

*The use of genetic algorithms was explored, however the computational cost of using them was deemed too high.

Appendices

Appendix A

Fresnel Reflections

In order to be able to accurately model the paths that light take in a medium where the refractive indices varies, Fresnel reflections and refractions must be modelled. To model these reflections and refractions in a simulation we calculate the Fresnel coefficients. Equations (A.1) to (A.3) shows the equations for calculating these for *s* and *p* polarised light, and unpolarised light (Eq. (A.3)).

$$R_s = \left| \frac{n_1 \cos \theta_i - n_2 \cos \theta_t}{n_1 \cos \theta_i + n_2 \cos \theta_t} \right|^2 \quad (\text{A.1})$$

$$R_p = \left| \frac{n_1 \cos \theta_t - n_2 \cos \theta_i}{n_1 \cos \theta_t + n_2 \cos \theta_i} \right|^2 \quad (\text{A.2})$$

$$R_{eff} = \frac{1}{2} (R_s + R_p) \quad (\text{A.3})$$

Where:

θ_i and θ_t are the angle of incidence and angle of transmission respectively,

see Eqs. (A.4) and (A.5) and Figs. A.1 and A.2;

n_1 and n_2 are the refractive indices of the current medium and the transmission medium [-];

R_s and R_p are the reflectance coefficients for *s* and *p* polarised light respectively [-];

finally, R_{eff} is the effective reflective coefficient for unpolarised light [-].

$$\sin \theta_t = \frac{n_1}{n_2} \sin \theta_i \quad (\text{A.4})$$

$$\cos \theta_t = \sqrt{1 - \sin \theta_t^2} \quad (\text{A.5})$$

R_{eff} gives a probability of reflection or refraction for a ray of light with an angle of incidence θ_i .

To calculate the angles of reflection and refraction, a vector form of Snell's law is used. Using the geometry illustrated in Fig. A.1 one can see that:

$$I = A + B \quad (\text{A.6})$$

$$R = A - B \quad (\text{A.7})$$

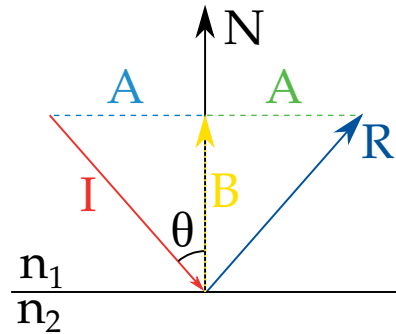


Figure A.1: Geometry for reflection of light at a refractive index boundary. I is incident light, R is the reflected light, and N is a normal to the surface. Here, θ is the angle of incidence which is equal to the angle of reflection.

$$B = \cos(\theta) \cdot N \quad (\text{A.8})$$

Therefore, substituting Eq. (A.8) into Eqs. (A.6) and (A.7) and rearranging yields:

$$I = A + \cos(\theta) \cdot N \quad (\text{A.9})$$

$$R = A - \cos(\theta) \cdot N \quad (\text{A.10})$$

$$\therefore R = I - 2(N \cdot I)N \quad (\text{A.11})$$

Where R gives the vector for a ray of light that has undergone reflection. Next we treat the transmission case. Figure A.2 gives the geometry for the situation, where the circle is a unit circle.

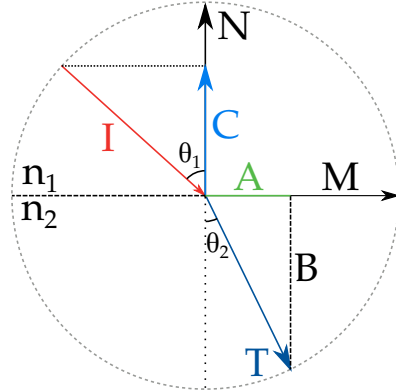


Figure A.2: Geometry of light refraction and reflections.

Again, one can deduce the following using trigonometry and Fig. A.2:

$$T = A + B \quad (\text{A.12})$$

$$A = \sin(\theta_2) M \quad (\text{A.13})$$

$$B = \cos(\theta_2) (-N) \quad (\text{A.14})$$

$$C = \cos(\theta_1) N \quad (\text{A.15})$$

$$M = \frac{I + C}{\sin(\theta_1)} \quad (\text{A.16})$$

Substituting Eqs. (A.13) to (A.16) into Eq. (A.12), using Snell's law (Eq. (A.21)), and rearranging yields:

$$T = A + B \quad (\text{A.17})$$

$$= M \sin \theta_2 - N \cos \theta_2 \quad (\text{A.18})$$

$$= \frac{I + C}{\sin \theta_1} \sin \theta_2 - N \cos \theta_2 \quad (\text{A.19})$$

$$= \frac{(I + \cos \theta_1 N) \sin \theta_2}{\sin \theta_1} - N \cos \theta_2 \quad (\text{A.20})$$

$$\frac{\sin \theta_1}{\sin \theta_2} = \frac{\eta_1}{\eta_2} \quad (\text{A.21})$$

$$\therefore T = \frac{\eta_1}{\eta_2} (I + \cos \theta_1 N) - N \cos \theta_2 \quad (\text{A.22})$$

$$T = \eta + (\eta c_1 - c_2) N \quad (\text{A.23})$$

Where Eq. (A.22) can be simplified by defining the following expressions:

$$c_1 = N \cdot I \quad (\text{A.24})$$

$$c_2 = \sqrt{1 - \eta^2(1 - c_1^2)} \quad (\text{A.25})$$

$$\eta = \frac{\eta_1}{\eta_2} \quad (\text{A.26})$$

To apply Eqs. (A.11) and (A.23) to our voxel model, the algorithm checks if there is a change in refractive index whenever a photon packet moves into a new voxel. If there is a change of refractive index the packet is placed on the surface of the voxel, and the algorithm calculates the surface normal of the voxel the light has hit and uses the above equations to calculate R_{eff} . With R_{eff} calculated a random number, ξ , is drawn. If ξ is less than R_{eff} then the photon packet is reflected, else then the packet is refracted into the new voxel. The new direction vectors are set according to Eqs. (A.11) and (A.23) and the packet is propagated as normal.

Appendix B

Detected Light Fluence Tracking Method

Most the fluence graphs presented in this thesis shows the fluence of the incident light throughout the simulated medium. However, there are problems where tracking the fluence of the detected light maybe useful, though this quantity is not straight forward to track. The current method of tracking fluence is to add pathlengths, calculated as the packet moves from voxel to voxel to a 3D array. This method obviously cannot determine which packet will be detected before the packet is detected, therefore a new method must be devised. This new method tracks the coordinates, direction vectors, random optical distance and fluorescent source of the packet using a stack. A stack is a commonly used abstract data structure, and is a collection of elements. In this case the elements are the coordinates, direction vectors, optical distance and fluorescent source. A stack has two main operations, pop and push. The push operation adds a new element to the collection, and the pop operation removes the most recently added element from the collection. This is known as last in first out (LIFO). Figure B.1 shows these two operations in action.

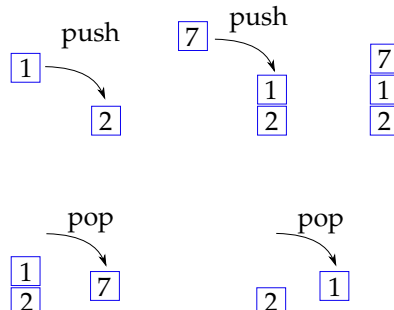


Figure B.1: Example of the push and pop operation on a stack. The first operation add the integer 2 to the stack. The second operation push 7 to the stack. The last operation pops the 7 from the stack.

The progress of each packet is pushed onto the stack, as it is propagated through the simulated medium. As mentioned above the packets coordinates, direction vectors, optical depth, and fluorescent source are the quantities pushed to the stack. These quantities are pushed to stack every time an interaction event occurs. When a packet is terminated, either via absorption or

it leaving the medium, the packets details are removed from the stack. This occurs unless the packet is detected. If the packet is detected then the information remains on the stack. This whole process repeats until all the packets have been run. Once all the packets have been run, the packets are “replayed”. This is achieved by popping the information off the stack and passed to the inttau2 routine. The packet is propagated again, this time recording the fluence as done in most of the chapters in this thesis.

Bibliography

- [1] J. Åqvist, C. Medina, and JE. Samuelsson. A new method for predicting binding affinity in computer-aided drug design. *Protein Engineering, Design and Selection*, 7(3):385–391, 1994.
- [2] M.A Lill and M.L Danielson. Computer-aided drug design platform using pymol. *Journal of computer-aided molecular design*, 25(1):13–19, 2011.
- [3] S. Liu, S. Liu, W. Cai, S. Pujol, R. Kikinis, and D. Feng. Early diagnosis of alzheimer’s disease with deep learning. In *2014 IEEE 11th international symposium on biomedical imaging (ISBI)*, pages 1015–1018. IEEE, 2014.
- [4] W. Sun, B. Zheng, and W. Qian. Computer aided lung cancer diagnosis with deep learning algorithms. In *Medical imaging 2016: computer-aided diagnosis*, volume 9785, page 97850Z. International Society for Optics and Photonics, 2016.
- [5] R.A Brooks and G. Di Chiro. Principles of computer assisted tomography (cat) in radiographic and radioisotopic imaging. *Physics in Medicine & Biology*, 21(5):689, 1976.
- [6] S. Al-Janabi, A. Huisman, and P.J Van Diest. Digital pathology: current status and future perspectives. *Histopathology*, 61(1):1–9, 2012.
- [7] A. El Saddik. Digital twins: The convergence of multimedia technologies. *IEEE MultiMedia*, 25(2):87–92, 2018.
- [8] H. van Houten. The rise of the digital twin: how healthcare can benefit. In <https://www.philips.com/a-w/about/news/archive/blogs/innovation-matters/20180830-the-rise-of-the-digital-twin-how-healthcare-can-benefit.html>. Philips, Aug 2018.
- [9] E.D Cashwell and C.J Everett. A practical manual on the monte carlo method for random walk problems. 1959.
- [10] D.W.O Rogers and A.F Bielajew. Monte carlo techniques of electron and photon transport for radiation dosimetry. *The dosimetry of ionizing radiation*, 3:427–539, 1990.
- [11] L. Badger. Lazzarini’s lucky approximation of π . *Mathematics Magazine*, 67(2):83–91, 1994.
- [12] P. Beckmann. *A history of Pi*. St. Martin’s Griffin, 2015.
- [13] GL.L Buffon. *Histoire naturelle générale et particulière*, volume 18. de l’Imprimerie de F. Dufart, 1785.
- [14] P. Jäckel. *Monte Carlo methods in finance*. J. Wiley, 2002.

- [15] D.B Hertz. Risk analysis in capital investment. *Harvard Business Review*, 42(1):95–106, 1964.
- [16] J.V Wall and C.R Jenkins. *Practical statistics for astronomers*. Cambridge University Press, 2012.
- [17] J.T Kajiya. The rendering equation. *SIGGRAPH Comput. Graph.*, 20(4):143–150, August 1986.
- [18] R.L Cook, T. Porter, and L Carpenter. Distributed ray tracing. *SIGGRAPH Comput. Graph.*, 18(3):137–145, January 1984.
- [19] T.P Robitaille. Hyperion: an open-source parallelized three-dimensional dust continuum radiative transfer code. *Astronomy & Astrophysics*, 536:A79, 2011.
- [20] T. Harries. Torus: Radiation transport and hydrodynamics code. *Astrophysics Source Code Library*, 2014.
- [21] R.M Valentine, C.T.A Brown, K. Wood, H. Moseley, and S. Ibbotson. Monte carlo modeling of in vivo protoporphyrin ix fluorescence and singlet oxygen production during photodynamic therapy for patients presenting with superficial basal cell carcinomas. *Journal of Biomedical Optics*, 16(4):048002, 2011.
- [22] C.L Campbell, K. Wood, R.M. Valentine, C.T.A Brown, and H. Moseley. Monte carlo modelling of daylight activated photodynamic therapy. *Physics in Medicine & Biology*, 60(10):4059, 2015.
- [23] M. Pharr, W. Jakob, and G. Humphreys. *Physically based rendering: From theory to implementation*. Morgan Kaufmann, 2016.
- [24] N. Metropolis. The beginning of the Monte Carlo method. *Los Alamos Science*, 15:125–130, 1987.
- [25] R. Eckhardt. Stan Ulam, John von Neumann, and the Monte Carlo method. *Los Alamos Science*, 15:131–136, 1987.
- [26] H.L Anderson. Metropolis, Monte Carlo, and the MANIAC. *Los Alamos Science*, 14:96–108, 1986.
- [27] S. Ulam, R.D Richtmyer, and J. Von Neumann. Statistical methods in neutron diffusion. *LAMS-551, Los Alamos National Laboratory*, pages 1–22, 1947.
- [28] K. Wood and R.J Reynolds. A model for the scattered light contribution and polarization of the diffuse $\text{H}\alpha$ galactic background. *The Astrophysical Journal*, 525(2):799, 1999.
- [29] D.W.O Rogers, B.A Faddegon, G.X Ding, C-M. Ma, J. We, and T.R Mackie. Beam: a monte carlo code to simulate radiotherapy treatment units. *Medical physics*, 22(5):503–524, 1995.
- [30] B.C Wilson and G. Adam. A monte carlo model for the absorption and flux distributions of light in tissue. *Medical Physics*, 10(6):824–830, 1983.
- [31] L.V Wang and H. Wu. *Biomedical optics: principles and imaging*. John Wiley & Sons, 2012.

- [32] S. Chandrasekhar. *Radiative transfer*. Courier Corporation, 2013.
- [33] V.DMZ Barbarić-Mikočević and K. Itrić. Kubelka-munk theory in describing optical properties of paper (i). *Technical Gazette*, 18(1):117–124, 2011.
- [34] M. Jasiński. Modelling of light and human skin interaction using kubelka-munk theory. *Scientific Research of the Institute of Mathematics and Computer Science*, 10(1):71–81, 2011.
- [35] WF. Cheong, S.A Prahl, and A.J Welch. A review of the optical properties of biological tissues. *IEEE journal of quantum electronics*, 26(12):2166–2185, 1990.
- [36] M. Gabriela. Mathematical methods in biomedical optics. *ISRN Biomedical Engineering*, 2013, 2013.
- [37] S.A Prahl. Light transport in tissue. 1990.
- [38] R. Graaff, J.G Aarnoudse, F.F.M de Mul, and H.W Jentink. Similarity relations for anisotropic scattering in absorbing media. *Optical engineering*, 32(2):244–253, 1993.
- [39] S.A Yoon, G.and Prahl and A.J Welch. Accuracies of the diffusion approximation and its similarity relations for laser irradiated biological media. *Applied Optics*, 28(12):2250–2255, 1989.
- [40] T.P Robitaille. On the modified random walk algorithm for monte-carlo radiation transfer. *Astronomy & Astrophysics*, 520:A70, 2010.
- [41] M. Min, C.P Dullemond, C. Dominik, A. de Koter, and J.W Hovenier. Radiative transfer in very optically thick circumstellar disks. *Astronomy & Astrophysics*, 497(1):155–166, 2009.
- [42] S.L Jacques. Origins of tissue optical properties in the uva, visible, and nir regions. *OSA TOPS on advances in optical imaging and photon migration*, 2:364–369, 1996.
- [43] S.L Jacques. Optical properties of biological tissues: a review. *Physics in Medicine & Biology*, 58(11):R37, 2013.
- [44] T. Lister, P.A Wright, and P.H Chappell. Optical properties of human skin. *Journal of biomedical optics*, 17(9):090901, 2012.
- [45] L.G Henyey and J.L Greenstein. Diffuse radiation in the galaxy. *The Astrophysical Journal*, 93:70–83, 1941.
- [46] S.L Jacques, C.A Alter, and S.A Prahl. Angular dependence of hene laser light scattering by human dermis. *Lasers Life Sci*, 1(4):309–333, 1987.
- [47] J.M Dixon, M. Taniguchi, and J.S Lindsey. Photochemcad 2: A refined program with accompanying spectral databases for photochemical calculations. *Photochemistry and photobiology*, 81(1):212–213, 2005.
- [48] S. Prahl. Photochemcad spectra. <https://omlc.org/spectra/PhotochemCAD/index.html>, 2017. [Online; Last accessed 4-February-2019].
- [49] D.J. Segelstein. *The complex refractive index of water*. PhD thesis, University of Missouri–Kansas City, 1981.

- [50] R.M Pope and E.S Fry. Absorption spectrum (380–700 nm) of pure water. ii. integrating cavity measurements. *Applied optics*, 36(33):8710–8723, 1997.
- [51] R.L.P van Veen, H.J.C.M Sterenborg, A. Pifferi, A. Torricelli, and R. Cubeddu. Determination of vis-nir absorption coefficients of mammalian fat, with time-and spatially resolved diffuse reflectance and transmission spectroscopy. In *Biomedical Topical Meeting*, page SF4. Optical Society of America, 2004.
- [52] I.S Saidi et al. *Transcutaneous optical measurement of hyperbilirubinemia in neonates*. PhD thesis, Rice University, 1992.
- [53] J.A Iglesias-Guitian, C. Aliaga, A. Jarabo, and D. Gutierrez. A biophysically-based model of the optical properties of skin aging. In *Computer Graphics Forum*, volume 34, pages 45–55. Wiley Online Library, 2015.
- [54] A.N Bashkatov, E.A Genina, and V.V Tuchin. Optical properties of skin, subcutaneous, and muscle tissues: a review. *Journal of Innovative Optical Health Sciences*, 4(01):9–38, 2011.
- [55] T. Sarna and H.A Swartz. The physical properties of melanins. *The pigmentary system: physiology and pathophysiology*, pages 311–341, 2006.
- [56] L.B. Lucy. Computing radiative equilibria with monte carlo techniques. *Astronomy and Astrophysics*, 344:282–288, 1999.
- [57] M. Metcalf, J. Reid, and M. Cohen. *Modern Fortran Explained*. Oxford University Press, 2011.
- [58] J.E Bjorkman and K. Wood. Radiative equilibrium and temperature correction in monte carlo radiation transfer. *The Astrophysical Journal*, 554(1):615, 2001.
- [59] W. Gropp, E. Lusk, and A. Skjellum. *Using MPI: Portable Parallel Programming with the Message-Passing Interface*. Scientific and Engineering Computation. MIT Press, 2014.
- [60] W. Gropp, T. Hoefler, R. Thakur, and E. Lusk. *Using advanced MPI: Modern features of the message-passing interface*. MIT Press, 2014.
- [61] G.M. Amdahl. Validity of the single processor approach to achieving large scale computing capabilities. In *Proceedings of the April 18-20, 1967, Spring Joint Computer Conference*, pages 483–485. ACM, 1967.
- [62] J. Bjorkman. Monte carlo radiation transfer. Presented as SAMCSS 2013, 2013.
- [63] C.M Gardner, S.L Jacques, and A.J Welch. Fluorescence and reflectance spectra specify intrinsic fluorescence spectrum corrected for tissue optics distortion. In *Advances in Fluorescence Sensing Technology*, volume 1885, pages 122–129. International Society for Optics and Photonics, 1993.
- [64] S.L Jacques, R. Joseph, and G. Gofstein. How photobleaching affects dosimetry and fluorescence monitoring of pdt in turbid media. In *Optical Methods for Tumor Treatment and Detection: Mechanisms and Techniques in Photodynamic Therapy II*, volume 1881, pages 168–180. International Society for Optics and Photonics, 1993.

- [65] D. Manstein, G.S. Herron, R.K. Sink, H. Tanner, and R.R. Anderson. Fractional photothermolysis: a new concept for cutaneous remodeling using microscopic patterns of thermal injury. *Lasers in Surgery and Medicine: The Official Journal of the American Society for Laser Medicine and Surgery*, 34(5):426–438, 2004.
- [66] S. Amini-Nik, D. Kraemer, M.L. Cowan, K. Gunaratne, P. Nadesan, B.A. Alman, and R.J. Dwayne Miller. Ultrafast mid-ir laser scalpel: protein signals of the fundamental limits to minimally invasive surgery. *PLoS One*, 5(9):e13053, 2010.
- [67] O.T. Tan, K. Sherwood, and B.A. Gilchrest. Treatment of children with port-wine stains using the flashlamp-pulsed tunable dye laser. *New England Journal of Medicine*, 320(7):416–421, 1989.
- [68] M. Kuperman-Beade, V.J. Levine, and R. Ashinoff. Laser removal of tattoos. *American Journal of Clinical Dermatology*, 2(1):21–25, 2001.
- [69] S.H. Liew. Laser hair removal. *American Journal of Clinical Dermatology*, 3(2):107–115, 2002.
- [70] C.A. Hardaway and E.V. Ross. Nonablative laser skin remodeling. *Dermatologic Clinics*, 20(1):97–111, 2002.
- [71] S.M. Shapshay, M.S. Strong, G.W. Anastasi, and C.W. Vaughan. Removal of rhinophyma with the carbon dioxide laser: a preliminary report. *Archives of Otolaryngology*, 106(5):257–259, 1980.
- [72] R. Valcavi, F. Riganti, A. Bertani, D. Formisano, and C.M. Pacella. Percutaneous laser ablation of cold benign thyroid nodules: a 3-year follow-up study in 122 patients. *Thyroid*, 20(11):1253–1261, 2010.
- [73] M. Hædersdal, F.H. Sakamoto, W.A. Farinelli, A.G. Doukas, J. Tam, and R.R. Anderson. Fractional CO₂ laser-assisted drug delivery. *Lasers in Surgery and Medicine: The Official Journal of the American Society for Laser Medicine and Surgery*, 42(2):113–122, 2010.
- [74] M.R. Alexiades-Armenakas, J.S. Dover, and K.A. Arndt. The spectrum of laser skin resurfacing: nonablative, fractional, and ablative laser resurfacing. *Journal of the American Academy of Dermatology*, 58(5):719–737, 2008.
- [75] D.V Widder. *The Heat Equation*, volume 67. Academic Press, 1976.
- [76] N. Ozisik. *Finite Difference Methods in Heat Transfer*. CRC press, 1994.
- [77] Alma Lasers GmbH. *PixelCO₂ Operator's Manual*. Alma Lasers GmbH.
- [78] S. Ristov, R. Prodan, M. Gusev, and K. Skala. Superlinear speedup in hpc systems: Why and when? In *Computer Science and Information Systems (FedCSIS), 2016 Federated Conference on*, pages 889–898. IEEE, 2016.
- [79] A.J Welch, M.J.C Van Gemert, et al. *Optical-thermal Response of Laser-irradiated Tissue*, volume 2. Springer, 2011.
- [80] N.T. Wright. Quantitative models of thermal damage to cells and tissues. In *Heat Transfer and Fluid Flow in Biological Processes*, pages 59–76. Elsevier, 2015.

- [81] M.H. Niemz. *Laser-tissue interactions: fundamentals and applications*. Springer Science & Business Media, 2013.
- [82] F. Petrella, S. Cavaliere, and L. Spaggiari. Popcorn effect. *Journal of Bronchology & Interventional Pulmonology*, 20(2):193–194, 2013.
- [83] R.M. Verdaasdonk, C. Borst, and M.J.C. Van Gemert. Explosive onset of continuous wave laser tissue ablation. *Physics in Medicine & Biology*, 35(8):1129, 1990.
- [84] W. Husinsky, G. Grabner, I. Baumgartner, F. Skorpik, S. Mitterer, and T. Temmel. Mechanisms of laser ablation of biological tissue. In *Desorption Induced by Electronic Transitions DIET IV*, pages 362–367. Springer, 1990.
- [85] M.S Kitai, V.L Popkov, V.A Semchischen, and A.A Kharizov. The physics of uv laser cornea ablation. *IEEE journal of quantum electronics*, 27(2):302–307, 1991.
- [86] A.A Oraevsky, R.O Esenaliev, and V.S Letokhov. Pulsed laser ablation of biological tissue: Review of the mechanisms. In *Laser Ablation Mechanisms and Applications*, pages 112–122. Springer, 1991.
- [87] A. Vogel and V. Venugopalan. Mechanisms of pulsed laser ablation of biological tissues. *Chemical Reviews*, 103(2):577–644, 2003.
- [88] G. Koren and J.T.C Yeh. Emission spectra, surface quality, and mechanism of excimer laser etching of polyimide films. *Applied Physics Letters*, 44(12):1112–1114, 1984.
- [89] J.E Andrew, P.E Dyer, D. Forster, and P.H Key. Direct etching of polymeric materials using a xecl laser. *Applied Physics Letters*, 43(8):717–719, 1983.
- [90] A.L. McKenzie. Physics of thermal processes in laser-tissue interaction. *Physics in Medicine & Biology*, 35(9):1175, 1990.
- [91] A.L. McKenzie. A three-zone model of soft-tissue damage by a CO₂ laser. *Physics in Medicine & Biology*, 31(9):967, 1986.
- [92] B. Majaron, P. Plestenjak, and M. Lukač. Thermo-mechanical laser ablation of soft biological tissue: modeling the micro-explosions. *Applied Physics B*, 69(1):71–80, 1999.
- [93] M. Gerstmann, Y. Linenberg, A. Katzir, and S. Akselrod. Char formation in tissue irradiated with a CO₂ laser: model and simulations. *Optical Engineering*, 33(7):2343–2352, 1994.
- [94] A. Sagi, A. Avidor-Zehavi, A. Shitzer, M. Gerstmann, S. Akselrod, and A. Katzir. Heating of biological tissue by laser irradiation: temperature distribution during laser ablation. *Opt. Eng*, 31(7):1425–1431, 1992.
- [95] J.A. Pearce. Relationship between arrhenius models of thermal damage and the cem 43 thermal dose. In *Energy-based Treatment of Tissue and Assessment V*, volume 7181, page 718104. International Society for Optics and Photonics, 2009.
- [96] F.C. Jr Hendriques. Studies of thermal injury; the predictability and the significance of thermally induced rate processes leading to irreversible epidermal injury. *Arch. Pathol.(Chic)*, 43:489–502, 1947.

- [97] S.C. Jiang, N. Ma, H.J. Li, and X.X. Zhang. Effects of thermal properties and geometrical dimensions on skin burn injuries. *Burns*, 28(8):713–717, 2002.
- [98] K.R. Diller and L.J. Hayes. A finite element model of burn injury in blood-perfused skin. *Journal of Biomechanical Engineering*, 105(3):300–307, 1983.
- [99] J. Zhang and X. Zhang. Dynamic modeling of tissue ablation with continuous wave co₂ laser. In *2007 1st International Conference on Bioinformatics and Biomedical Engineering*, pages 1057–1060. IEEE, 2007.
- [100] I.V. Meglinski and S.J. Matcher. Quantitative assessment of skin layers absorption and skin reflectance spectra simulation in the visible and near-infrared spectral regions. *Physiological Measurement*, 23(4):741, 2002.
- [101] B.R. Loiola, H.R.B. Orlande, and G.S. Dulikravich. Thermal damage during ablation of biological tissues. *Numerical Heat Transfer, Part A: Applications*, pages 1–17, 2018.
- [102] V. Casalegno, P. Vavassori, M. Valle, M. Ferraris, M. Salvo, and G. Pintsuk. Measurement of thermal properties of a ceramic/metal joint by laser flash method. *Journal of Nuclear Materials*, 407(2):83–87, 2010.
- [103] E. MacCormack, A. Mandelis, M. Munidasa, B. Farahbakhsh, and H. Sang. Measurements of the thermal diffusivity of aluminum using frequency-scanned, transient, and rate window photothermal radiometry. theory and experiment. *International journal of thermophysics*, 18(1):221–250, 1997.
- [104] Alma Lasers. Pixel CO₂, 2018.
- [105] M. Lapidoth, S. Halachmi, S. Cohen, and D.B. Amitai. Fractional co₂ laser in the treatment of facial scars in children. *Lasers in Medical Science*, 29(2):855–857, 2014.
- [106] M.A. Trelles, M. Shohat, and F. Urdiales. Safe and effective one-session fractional skin resurfacing using a carbon dioxide laser device in super-pulse mode: a clinical and histologic study. *Aesthetic Plastic Surgery*, 35(1):31–42, 2011.
- [107] E. Kohl, J. Meierhöfer, M. Koller, F. Zeman, L. Groesser, S. Karrer, U. Hohenleutner, M. Landthaler, and S. Hohenleutner. Fractional carbon dioxide laser resurfacing of rhytides and photoaged skin—a prospective clinical study on patient expectation and satisfaction. *Lasers in Surgery and Medicine*, 47(2):111–119, 2015.
- [108] J. Baumgartl, M. Mazilu, and K. Dholakia. Optically mediated particle clearing using airy wavepackets. *Nature photonics*, 2(11):675, 2008.
- [109] D.B Ruffner and D.G Grier. Optical conveyors: a class of active tractor beams. *Physical review letters*, 109(16):163903, 2012.
- [110] T. Vettenburg, H.I.C Dalgarno, J. Nylk, C. Coll-Lladó, D.E.K Ferrier, T. Čižmár, F.J Gunn-Moore, and K. Dholakia. Light-sheet microscopy using an airy beam. *Nature methods*, 11(5):541, 2014.
- [111] N.B Simpson, L. Allen, and M.J Padgett. Optical tweezers and optical spanners with laguerre–gaussian modes. *Journal of modern optics*, 43(12):2485–2491, 1996.
- [112] A.K Glaser, Y. Chen, and J.T.C Liu. Fractal propagation method enables realistic optical microscopy simulations in biological tissues. *Optica*, 3(8):861–869, 2016.

- [113] A. Elmaklizi, D. Reitzle, A.R Brandes, and A. Kienle. Penetration depth of focused beams in highly scattering media investigated with a numerical solution of maxwells equations in two dimensions. *Journal of biomedical optics*, 20(6):065007, 2015.
- [114] J. Van Roey, J. Van der Donk, and P.E Lagasse. Beam-propagation method: analysis and assessment. *Josa*, 71(7):803–810, 1981.
- [115] B.H Hokr, J.N Bixler, G. Elpers, B. Zollars, R.J Thomas, V.V Yakovlev, and M.O Scully. Modeling focusing gaussian beams in a turbid medium with monte carlo simulations. *Optics express*, 23(7):8699–8705, 2015.
- [116] J. Arnaud. Representation of gaussian beams by complex rays. *Applied optics*, 24(4):538–543, 1985.
- [117] J.E Harvey, R.G Irvin, and R.N Pfisterer. Modeling physical optics phenomena by complex ray tracing. *Optical Engineering*, 54(3):035105, 2015.
- [118] N.G Worku, R. Hambach, and H. Gross. Decomposition of a field with smooth wavefront into a set of gaussian beams with non-zero curvatures. *JOSA A*, 35(7):1091–1102, 2018.
- [119] F. Cai and S. He. Electric field monte carlo simulation of focused stimulated emission depletion beam, radially and azimuthally polarized beams for in vivo deep bioimaging. *Journal of biomedical optics*, 19(1):011022, 2014.
- [120] F.A Volpe, P-D. Létourneau, and A. Zhao. Huygens–fresnel wavefront tracing. *Computer Physics Communications*, 212:123–131, 2017.
- [121] C. Mignon, A.H. Rodriguez, J.A Palero, B. Varghese, and M. Jurna. Fractional laser photothermolysis using bessel beams. *Biomedical optics express*, 7(12):4974–4981, 2016.
- [122] S. Peter, P. Modregger, M.K Fix, W. Volken, D. Frei, P. Manser, and M. Stampanoni. Combining monte carlo methods with coherent wave optics for the simulation of phase-sensitive x-ray imaging. *Journal of synchrotron radiation*, 21(3):613–622, 2014.
- [123] J.R Mahan, N.Q Vinh, V.X Ho, and N.B Munir. Monte carlo ray-trace diffraction based on the huygens–fresnel principle. *Applied optics*, 57(18):D56–D62, 2018.
- [124] M. Mout, M. Wick, F. Bociort, J. Petschulat, and P. Urbach. Simulating multiple diffraction in imaging systems using a path integration method. *Applied optics*, 55(14):3847–3853, 2016.
- [125] D.G Fischer, S.A Prahl, and D.D Duncan. Monte carlo modeling of spatial coherence: free-space diffraction. *JOSA A*, 25(10):2571–2581, 2008.
- [126] C. Huygens. *Treatise on light*. tredition, 2012.
- [127] E. Hecht. *Optics*. Pearson Education, Incorporated, 2017.
- [128] C. Huygens, T. Young, A.J. Fresnel, and F. Arago. *The wave theory of light: memoirs of Huygens, Young and Fresnel*, volume 15. American Book Company, 1900.
- [129] A. Fresnel. Mémoire sur la diffraction de la lumière. *da p. 339 a p. 475: 1 tav. ft; AQ 210*, page 339, 1819.
- [130] G. Kirchhoff. Ann. d. physik. (2), 18:663, 1883.

- [131] M. Born, E. Wolf, and A.B. Bhatia. *Principles of Optics: Electromagnetic Theory of Propagation, Interference and Diffraction of Light*. Cambridge University Press, 2000.
- [132] J.W. Goodman. *Introduction to Fourier Optics*. W. H. Freeman, 2017.
- [133] P.W. Milonni and J.H. Eberly. *Laser Physics*. Wiley, 2010.
- [134] Thorlabs Inc. UV fused silica plano-convex lenses. <https://www.thorlabs.com/thorproduct.cfm?partnumber=LA4249>, 2019. [Online; accessed 18-April-2019].
- [135] J.M. Durnin, J.J. Miceli Jr, and J.H. Eberly. Diffraction-free beams. *Physical review letters*, 58(15):1499, 1987.
- [136] J.M. Durnin. Exact solutions for nondiffracting beams. I. the scalar theory. *JOSA A*, 4(4):651–654, 1987.
- [137] D. McGloin and K. Dholakia. Bessel beams: diffraction in a new light. *Contemporary Physics*, 46(1):15–28, 2005.
- [138] D. DeBeer, S.R Hartmann, and R. Friedberg. Comment on “diffraction-free beams”. *Physical review letters*, 59(22):2611, 1987.
- [139] J.E Harvey and J.L Forgham. The spot of arago: new relevance for an old phenomenon. *American journal of Physics*, 52(3):243–247, 1984.
- [140] J. Durnin, J.J Miceli, and J.H Eberly. Reply to d. debeer, sr hartmann and r. friedberg. *Phys. Rev. Lett.*, 59:2612, 1987.
- [141] P. Sprangle and B. Hafizi. Comment on nondiffracting beams. *Physical review letters*, 66(6):837, 1991.
- [142] J. Durnin, J.J Miceli Jr, and J.H Eberly. Durnin, miceli, and eberly reply. *Physical review letters*, 66(6):838, 1991.
- [143] T. Čižmár. *Optické pasti generované netradičními svazky*. PhD thesis, Masarykova univerzita, Přírodovědecká fakulta, 2006.
- [144] F. Merola, S. Coppola, V. Vespi, S. Grilli, and P. Ferraro. Characterization of bessel beams generated by polymeric microaxicons. *Measurement Science and Technology*, 23(6):065204, 2012.
- [145] B. Aernouts, E. Zamora-Rojas, R. Van Beers, R. Watté, L. Wang, M. Tsuta, J. Lamertyn, and W. Saeys. Supercontinuum laser based optical characterization of intralipid® phantoms in the 500–2250 nm range. *Optics express*, 21(26):32450–32467, 2013.
- [146] M.I Mishchenko. independent and dependent scattering by particles in a multi-particle group. *OSA Continuum*, 1(1):243–260, 2018.
- [147] M.Z. Vardaki, B. Gardner, N. Stone, and P. Matousek. Studying the distribution of deep raman spectroscopy signals using liquid tissue phantoms with varying optical properties. *Analyst*, 140(15):5112–5119, 2015.
- [148] P. Di Ninni, F. Martelli, and G. Zaccanti. Effect of dependent scattering on the optical properties of intralipid tissue phantoms. *Biomedical optics express*, 2(8):2265–2278, 2011.

- [149] R. Michels, F. Foschum, and A. Kienle. Optical properties of fat emulsions. *Optics Express*, 16(8):5907–5925, 2008.
- [150] V. Garcés-Chávez, K. Volke-Sepulveda, S. Chávez-Cerda, W. Sibbett, and K. Dholakia. Transfer of orbital angular momentum to an optically trapped low-index particle. *Physical Review A*, 66(6):063402, 2002.
- [151] V. Garcés-Chávez, D. McGloin, M.J Padgett, W. Dultz, H. Schmitzer, and K. Dholakia. Observation of the transfer of the local angular momentum density of a multiringed light beam to an optically trapped particle. *Physical review letters*, 91(9):093602, 2003.
- [152] X. Wei, C. Liu, L. Niu, Z. Zhang, K. Wang, Z. Yang, and J. Liu. Generation of arbitrary order bessel beams via 3d printed axicons at the terahertz frequency range. *Applied optics*, 54(36):10641–10649, 2015.
- [153] S.N. Khonina, V.V. Kotlyar, V.A. Soifer, M.V. Shinkaryev, and G.V. Uspleniev. Trochoson. *Optics Communications*, 91(3-4):158–162, 1992.
- [154] V.V. Kotlyar, A.A. Kovalev, S.N. Khonina, R.V. Skidanov, V.A. Soifer, H. Elfstrom, N. Tossavainen, and J. Turunen. Diffraction of conic and gaussian beams by a spiral phase plate. *Applied optics*, 45(12):2656–2665, 2006.
- [155] S. Topuzoski and L. Janicijevic. Conversion of high-order laguerre-gaussian beams into bessel beams of increased, reduced or zeroth order by use of a helical axicon. *Optics Communications*, 282(17):3426–3432, 2009.
- [156] S. Qiong-Ge, Z. Ke-Ya, F. Guang-Yu, L. Zheng-Jun, and L. Shu-Tian. Generalization and propagation of spiraling bessel beams with a helical axicon. *Chinese Physics B*, 21(1):014208, 2012.
- [157] World Health Organisation. *Cardiovascular diseases (CVDs)*, 17 May 2017 (accessed June 16, 2019). [https://www.who.int/en/news-room/fact-sheets/detail/cardiovascular-diseases-\(cvds\)](https://www.who.int/en/news-room/fact-sheets/detail/cardiovascular-diseases-(cvds)).
- [158] P. Bhatnagar, K. Wickramasinghe, E. Wilkins, and N. Townsend. Trends in the epidemiology of cardiovascular disease in the uk. *Heart*, 102(24):1945–1952, 2016.
- [159] R.S. Vasan. Biomarkers of cardiovascular disease: molecular basis and practical considerations. *Circulation*, 113(19):2335–2362, 2006.
- [160] M.H. Olsen. Assessment of cardiovascular risk â the impact and future of non-traditional cardiovascular risk markers. 2010.
- [161] A.R. Folsom. Classical and novel biomarkers for cardiovascular risk prediction in the united states. *Journal of epidemiology*, page JE20120157, 2013.
- [162] N. Kollias, R. Gillies, M. Moran, I.E Kochevar, and R.R Anderson. Endogenous skin fluorescence includes bands that may serve as quantitative markers of aging and photoaging. *Journal of investigative dermatology*, 111(5):776–780, 1998.
- [163] M. Monici. Cell and tissue autofluorescence research and diagnostic applications. *Biotechnology annual review*, 11:227–256, 2005.

- [164] E. Drakaki, E. Kaselouris, M. Makropoulou, A.A Serafetinides, A. Tsenga, A.J Stratigos, A.D Katsambas, and C. Antoniou. Laser-induced fluorescence and reflectance spectroscopy for the discrimination of basal cell carcinoma from the surrounding normal skin tissue. *Skin pharmacology and physiology*, 22(3):158, 2009.
- [165] Y. Pu, W. Wang, Y. Yang, and R.R. Alfano. Native fluorescence spectra of human cancerous and normal breast tissues analyzed with non-negative constraint methods. *Applied optics*, 52(6):1293–1301, 2013.
- [166] N. Ramanujam. Fluorescence spectroscopy of neoplastic and non-neoplastic tissues. *Neoplasia*, 2(1-2):89–117, 2000.
- [167] M. Tarnawska, K. Dorniak, M. Kaszubowski, M. Dudziak, and M. Hellmann. A pilot study with flow mediated skin fluorescence: A novel device to assess microvascular endothelial function in coronary artery disease. *Cardiology journal*, 25(1):120–127, 2018.
- [168] R.P. van Waateringe, B.T. Fokkens, S.N. Slagter, M.M. van der Klauw, J.V. van Vliet-Ostaptchouk, R. Graaff, A.D. Paterson, A.J. Smit, H.L. Lutgers, and B.H.R. Wolffenbuttel. Skin autofluorescence predicts incident type 2 diabetes, cardiovascular disease and mortality in the general population. *Diabetologia*, 62(2):269–280, 2019.
- [169] N. Akbar, S. Sokolovski, A. Dunaev, J.J.F. Belch, E. Rafailov, and F. Khan. In vivo non-invasive measurement of skin autofluorescence biomarkers relate to cardiovascular disease in mice. *Journal of microscopy*, 255(1):42–48, 2014.
- [170] M.M. Elahi, Y.X. Kong, and B.M. Matata. Oxidative stress as a mediator of cardiovascular disease. *Oxidative medicine and cellular longevity*, 2(5):259–269, 2009.
- [171] T.S. Blacker and M.R. Duchen. Investigating mitochondrial redox state using nadh and nadph autofluorescence. *Free Radical Biology and Medicine*, 100:53–65, 2016.
- [172] A.C. Croce and G. Bottioli. Autofluorescence spectroscopy and imaging: a tool for biomedical research and diagnosis. *European journal of histochemistry: EJH*, 58(4), 2014.
- [173] I.M. Freedberg and T.B. Fitzpatrick. *Fitzpatrick's Dermatology in General Medicine*. Number v. 2 in Fitzpatrick's Dermatology in General Medicine. McGraw-Hill, Health Professions Division, 1999.
- [174] Z. Zaidi and S.W. Lanigan. *Dermatology in Clinical Practice*. Springer London, 2010.
- [175] S. Prahl. *Tabulated Molar Extinction Coefficient for Hemoglobin in Water*, 1999 (accessed June 15, 2019). <https://omlc.org/spectra/hemoglobin/summary.html>.
- [176] D.M. Wieliczka, S. Weng, and M.R. Querry. Wedge shaped cell for highly absorbent liquids: infrared optical constants of water. *Applied optics*, 28(9):1714–1719, 1989.
- [177] S.L. Jacques, I.S. Saidi, A. Ladner, and D. Oelberg. Developing an optical fiber reflectance spectrometer to monitor bilirubinemia in neonates. In *Laser-Tissue Interaction VIII*, volume 2975, pages 115–125. International Society for Optics and Photonics, 1997.
- [178] S. Prahl. *Tabulated Molar Extinction Coefficient for Bilirubin in chloroform*, 2017 (accessed June 15, 2019). <https://omlc.org/spectra/PhotochemCAD/html/119.html>.
- [179] S. Prahl. *Tabulated Molar Extinction Coefficient for Beta-carotene in hexane*, 2017 (accessed June 15, 2019). <https://omlc.org/spectra/PhotochemCAD/html/041.html>.

- [180] A. Krishnaswamy and G.V.G Baranowski. A biophysically-based spectral model of light interaction with human skin. In *Computer Graphics Forum*, volume 23, pages 331–340. Wiley Online Library, 2004.
- [181] C.L Campbell, C. Christison, C.T.A Brown, K. Wood, R.M. Valentine, and H. Moseley. 3d monte carlo radiation transfer modelling of photodynamic therapy. In *Biophotonics South America*, volume 9531, page 95311H. International Society for Optics and Photonics, 2015.
- [182] C. Campbell. *Under the skin: Monte Carlo radiation transfer modelling of photodynamic therapy*. PhD thesis, School of Physics and Astronomy, University of St Andrews, 2016.
- [183] M.J.C Van Gemert, S.L Jacques, H.J.C.M Sterenborg, and W.M. Star. Skin optics. *IEEE Transactions on biomedical engineering*, 36(12):1146–1154, 1989.
- [184] R. Gillies, G. Zonios, R.R Anderson, and N. Kollias. Fluorescence excitation spectroscopy provides information about human skin in vivo. *Journal of Investigative Dermatology*, 115(4):704–707, 2000.
- [185] S. Prahls. *Tabulated Molar Extinction Coefficient for Tyrosine in water, 0.1 M phosphate buffer, pH 7*, 2017 (accessed June 16, 2019). <https://omlc.org/spectra/PhotochemCAD/html/092.html>.
- [186] S. Prahls. *Tabulated Molar Extinction Coefficient for Tryptophan in water, 0.1 M phosphate buffer, pH 7*, 2017 (accessed June 16, 2019). <https://omlc.org/spectra/PhotochemCAD/html/091.html>.
- [187] S. Soltani, A. Ojaghi, and F.E Robles. Deep uv dispersion and absorption spectroscopy of biomolecules. *Biomedical optics express*, 10(2):487–499, 2019.
- [188] Y. Sun, Y. Pu, Y. Yang, and R.R. Alfano. Biomarkers spectral subspace for cancer detection. *Journal of biomedical optics*, 17(10):107005, 2012.
- [189] M. Islam, M. Honma, T. Nakabayashi, M. Kinjo, and N. Ohta. ph dependence of the fluorescence lifetime of fad in solution and in cells. *International journal of molecular sciences*, 14(1):1952–1963, 2013.
- [190] E.W Evans, C.A Dodson, K. Maeda, T. Biskup, C.J. Wedge, and C.R. Timmel. Magnetic field effects in flavoproteins and related systems. *Interface focus*, 3(5):20130037, 2013.
- [191] A. Von Ketteler, D.P Herten, and W. Petrich. Fluorescence properties of carba nicotinamide adenine dinucleotide for glucose sensing. *ChemPhysChem*, 13(5):1302–1306, 2012.
- [192] R.S DaCosta, H. Andersson, and B.C Wilson. Molecular fluorescence excitation–emission matrices relevant to tissue spectroscopy. *Photochemistry and photobiology*, 78(4):384–392, 2003.
- [193] F. Gao and L. Han. Implementing the nelder-mead simplex algorithm with adaptive parameters. *Computational Optimization and Applications*, 51(1):259–277, 2012.
- [194] W.H. Press and S.A. Teukolsky. Savitzky-golay smoothing filters. *Computers in Physics*, 4(6):669–672, 1990.
- [195] S. Palmer, K. Litvinova, A. Dunaev, S. Fleming, D. McGloin, and G. Nabi. Changes in auto-fluorescence based organoid model of muscle invasive urinary bladder cancer. *Biomedical optics express*, 7(4):1193–1200, 2016.

- [196] A.V Dunaev, V.V Dremin, E.A Zherebtsov, I.E Rafailov, K.S Litvinova, S.G Palmer, N.A Stewart, S.G Sokolovski, and E.U Rafailov. Individual variability analysis of fluorescence parameters measured in skin with different levels of nutritive blood flow. *Medical engineering & physics*, 37(6):574–583, 2015.
- [197] O.D Smirnova, D.A Rogatkin, and K.S Litvinova. Collagen as in vivo quantitative fluorescent biomarkers of abnormal tissue changes. *Journal of Innovative Optical Health Sciences*, 5(02):1250010, 2012.
- [198] S.G Palmer. *Development of Non-invasive Techniques for Bladder Cancer Diagnosis and Therapy*. PhD thesis, University of Dundee, 2016.
- [199] YL. Pan. Detection and characterization of biological and other organic-carbon aerosol particles in atmosphere using fluorescence. *Journal of Quantitative Spectroscopy and Radiative Transfer*, 150:12–35, 2015.
- [200] G.H Patterson, S.M Knobel, P. Arkhammar, O. Thastrup, and D.W Piston. Separation of the glucose-stimulated cytoplasmic and mitochondrial nad (p) h responses in pancreatic islet β cells. *Proceedings of the National Academy of Sciences*, 97(10):5203–5207, 2000.
- [201] M. Singh, D.C.C Harris-Birtill, Y. Zhou, M.E Gallina, A.E.G Cass, G.B Hanna, and D.S Elson. Application of gold nanorods for photothermal therapy in ex vivo human oesophagogastric adenocarcinoma. *Journal of biomedical nanotechnology*, 12(3):481–490, 2016.
- [202] M.E Gallina, Y. Zhou, C.J Johnson, D. Harris-Birtill, M. Singh, H. Zhao, D. Ma, T. Cass, and D.S Elson. Aptamer-conjugated, fluorescent gold nanorods as potential cancer theranostic agents. *Materials Science and Engineering: C*, 59:324–332, 2016.
- [203] Ivo M Vellekoop and AP Mosk. Focusing coherent light through opaque strongly scattering media. *Optics letters*, 32(16):2309–2311, 2007.
- [204] Roarke Horstmeyer, Haowen Ruan, and Changhuei Yang. Guidestar-assisted wavefront-shaping methods for focusing light into biological tissue. *Nature photonics*, 9(9):563, 2015.
- [205] Tomáš Čižmár, Michael Mazilu, and Kishan Dholakia. In situ wavefront correction and its application to micromanipulation. *Nature Photonics*, 4(6):388, 2010.